

Electronic Structures of Metal Sites in Proteins and Models: Contributions to Function in Blue Copper Proteins

Edward I. Solomon,^{*,†} Robert K. Szilagyi,[†] Serena DeBeer George,[‡] and Lipika Basumallick[†]

Department of Chemistry, Stanford University, Stanford, California 94305, and Stanford Synchrotron Radiation Laboratory, SLAC, Stanford University, Stanford, California 94309

Received May 23, 2003

Contents

1. Introduction	419
2. Electronic Structure of D_{4h} $[\text{CuCl}_4]^{2-}$	423
2.1. Spectroscopy	423
2.2. Evaluation and Calibration of DFT Calculations	425
2.2.1. Correlation to Spectroscopy	425
2.2.2. Potential Energy Surface (PES)	426
3. Electronic Structure of Oxidized Blue Copper Sites	427
3.1. Orientation of the Ground State: Single-Crystal EPR	428
3.1.1. Origin of Small A_{ij} : Copper K-Edge XAS	428
3.1.2. Quantitative Analysis of g Values: Covalency	430
3.2. Experimental Probes of Covalency and the Nature of the Ground State Wave Function	430
3.2.1. Copper L-Edge Spectroscopy	430
3.2.2. Sulfur K-Edge Spectroscopy	431
3.2.3. LT MCD Spectroscopy	431
3.3. Comparison to DFT Calculations	432
4. Electronic Structure of the Reduced Blue Copper Site: Changes in Geometric and Electronic Structure with Oxidation	434
4.1. Variable Energy Photoelectron Spectroscopy (VEPES)	434
4.2. X-ray Absorption Spectroscopy (XAS)	437
5. Blue Copper Geometric and Electronic Structure: Role of the Protein	439
5.1. Standard Ligand Set [S(Cys), 2 N(His), and S(Met)]: The Coupled Distortion	439
5.1.1. Green to Blue Copper Sites: The M182T Mutant of Nitrite Reductase	441
5.2. Variation in the Chemical Nature of the Axial Ligand	442
5.2.1. No Axial Ligand: Fungal Laccases and Fet3p	442
5.2.2. Stellacyanin Axial Mutants: Variation of the Axial Ligand in a Fixed Protein Environment	443
5.3. Electronic Structure Calculations	444
6. Spectroscopic and Electronic Structure Studies of Blue Copper Model Complexes	446
7. Electronic Structure Contributions to Function	451

7.1. Reduction Potential (E_0)	452
7.2. ET Rate (k_{ET})	453
7.2.1. Reorganization Energy (λ)	454
7.2.2. Electronic Coupling Matrix Element (H_{DA})	454
8. Concluding Comments	455
9. Acknowledgment	456
10. References	456

1. Introduction

Approximately one-half of all known protein crystal structures in the protein data bank (PDB) contain metal ion cofactors, which play vital roles in charge neutralization, structure, and function.^{1,2} These proteins range in size from 5000–10⁷ Da with the metal ion corresponding to only on the order of 0.1 wt % of the molecule. Yet, for a wide range of these metalloproteins, the metal ion and its environment are key to the chemistry as these comprise the active site in catalysis. It is the purpose of this review to present the information content of spectroscopic methods, which allow one to focus in on the metalloactive site (Figure 1), define its electronic structure, evaluate the role of the protein in determining geometric and electronic structure, and elucidate the contributions of electronic structure to function.

Metalloproteins are simply metal complexes but with remarkably intricate and complex ligands. The metal ion, clusters of metal ions bridged by oxide or sulfide ligands or equatorially chelated by N-heterocyclic ligands (heme, corrin, etc.), are bound to the protein through one or more of the endogenous ligand lone pair donors in Table 1. Note that for most of the donor groups, this requires deprotonation, and the metal ion competition with the proton for the free base lowers the effective pK_A by at least several log units from those intrinsic values listed in Table 1. It is important to emphasize that for a number of the ligands in Tables 1 and 2, in particular phenolate, thiolate, oxo and sulfido, and the N-heterocyclic chelates, the metal complex exhibits extremely intense low energy charge transfer (CT) absorption bands, which reflect highly covalent ligand–metal bonds. These make major contributions to the electronic structure of an active site and can be affected by the geometry of the metal site and the orientation of the ligand–metal bond, which in turn can be influenced by the protein matrix.

* To whom correspondence should be addressed.

[†] Department of Chemistry, Stanford University.

[‡] Stanford Synchrotron Radiation Laboratory, SLAC, Stanford University.



Edward I. Solomon (second from left) grew up in North Miami Beach, FL, received his Ph.D. from Princeton University (with D. S. McClure), and was a postdoctoral fellow at the H. C. Ørsted Institute (with C. J. Ballhausen) and then at Caltech (with H. B. Gray). He was a professor at MIT until 1982. He then moved to Stanford University where he is now a Monroe E. Spaght Professor of Humanities and Sciences. His research is in the fields of physical inorganic and bioinorganic chemistry with emphasis on the application of a wide variety of spectroscopic methods combined with density functional calculations to elucidate the electronic structures of transition metal complexes and their contributions to physical properties and reactivity.

Robert Szilagyí (right) grew up in Makó, Hungary, and received his Ph.D. from University of Veszprém with Prof. Lajos Bencze. As a graduate student, he was fortunate to work with Prof. Nino Russo, University of Calabria, and Prof. Gernot Frenking, Philipps University Marburg. He was a postdoctoral fellow at Emory University, where he worked with Prof. Keiji Morokuma and Dr. Djameladdin G. Musaev. He continued his postdoctoral work at Stanford University with Profs. Britt Hedman, Keith O. Hodgson, and Edward I. Solomon. Since July 2003, he has been an assistant professor in the Department of Chemistry and Biochemistry at Montana State University, where he combines X-ray absorption spectroscopy with electronic structure calculations to study inorganic and organometallic systems with biological and industrial importance.

Serena DeBeer George (second from right) received her B.S. in Chemistry from Southwestern University in Georgetown, Texas, and her Ph.D. from Stanford University (under the direction of Edward I. Solomon and Keith O. Hodgson). Her doctoral research focused on the use of X-ray absorption spectroscopy to investigate the electronic and geometric structure of copper-containing metalloproteins. After she completed her Ph.D., she joined the scientific staff at the Stanford Synchrotron Radiation laboratory, where she continues to pursue synchrotron-based methods to elucidate the electronic and geometric structure of both bioinorganic and organometallic systems.

Lipika Basumallick (left) received her Masters in Chemistry from the Indian Institute of Technology, Kanpur. She worked on summer projects with Prof. C. N. R. Rao at the Jawaharlal Nehru Center for Advanced Scientific Research, Bangalore, and Prof. John A. Gladysz at the University of Utah, Salt Lake City. She is currently working toward her Ph.D. in chemistry at Stanford University under the direction of Prof. Edward I. Solomon. Her research interests focus on bioinorganic spectroscopy and in particular the blue copper electron transfer proteins. Her other interests include music and traveling.

In addition to the role of the local environment in forming the active site complex, one can define a hierarchy of roles of the protein primary to quaternary structure in the function of the metalloprotein. These are summarized in Figure 2, adapted from ref 3. These include (i) allosteric interactions between active sites in different subunits; (ii) organization of metal sites within a protein molecule for directional electron transfer (ET) to a catalytic site; (iii) surface recognition sites for interactions with donor and

acceptor proteins; (iv) covalent ET pathways within the protein; (v) forming substrate access channels (static or dynamic) to the active site; (vi) providing an active site hydrophobic environment within the protein in aqueous solution; (vii) forming a substrate binding pocket near the metal active site; (viii) assembling additional reactive covalently or noncovalently bound organic cofactors for catalysis; (ix) providing specific charge and H-bonding residues near the metal site to assist in catalysis; and (x) imposing a unique geometry on the metal site, which can activate it for reactivity. The last point has been termed the entatic (by Bob Williams)⁴ or rack-induced (by the late Bo Malmström) state.⁵ Arguments for and against this idea have been recently discussed, often with respect to the blue copper site (vide infra).^{6–11}

Figure 3 presents a complete energy level diagram for square planar D_{4h} $[\text{CuCl}_4]^{2-}$,¹² which will be considered in section 2 as a reference complex for understanding the unique spectroscopic features of the blue copper site in section 3. Spectroscopic methods that probe these energy levels cover over 10 orders of magnitude in photon energy.¹³ As summarized below and in Figure 3, different methods provide complimentary information into an active site, and by utilizing the appropriate combination of methods, one can obtain insight into geometric and electronic structure and their contribution to function.¹⁴

The ligand field (LF) environment of the metal site splits its d orbitals in energy. The highest energy orbitals are partially occupied, and these contribute to the magnetic properties of the active site ground state. Covalency further extends these magnetic orbitals onto the ligands involved in specific bonding interactions with the metal ion. To probe the ground state, complexes with unpaired electrons are placed in an external magnetic field and studied at low resolution by magnetic susceptibility and at high resolution by magnetic Mössbauer (for iron) and electron paramagnetic resonance (EPR)-based methods in the microwave energy region ($< \sim 1 \text{ cm}^{-1}$). The dominant information available from these methods is the anisotropy of the g tensor (formally a matrix), which is governed by the nature of d orbitals containing the unpaired electrons. From a single-crystal study, the orientation dependence of the g matrix defines the orientation of the singly occupied orbitals of the metal site. Magnetic Mössbauer and EPR also exhibit hyperfine couplings of the unpaired electrons to the nuclear spins on the metal and the ligands (the latter called superhyperfine coupling). These provide probes of the covalency (i.e., the metal and ligand contributions to the valence orbitals). The superhyperfine coupling is a very direct probe of the ligand character in a metal d-derived molecular orbital (MO); however, this coupling is often too small to resolve in a continuous wave, single-resonance EPR study. Superhyperfine coupling can alternatively be measured using double-resonance (i.e., in electron–nuclear double-resonance, ENDOR) and pulsed (i.e., electron spin–echo envelope modulation, ESEEM) methods. For ground states with $S > 1/2$, the spin degeneracy in $|M_S|$ can be split even in the absence of a magnetic field. This is known as zero field split-

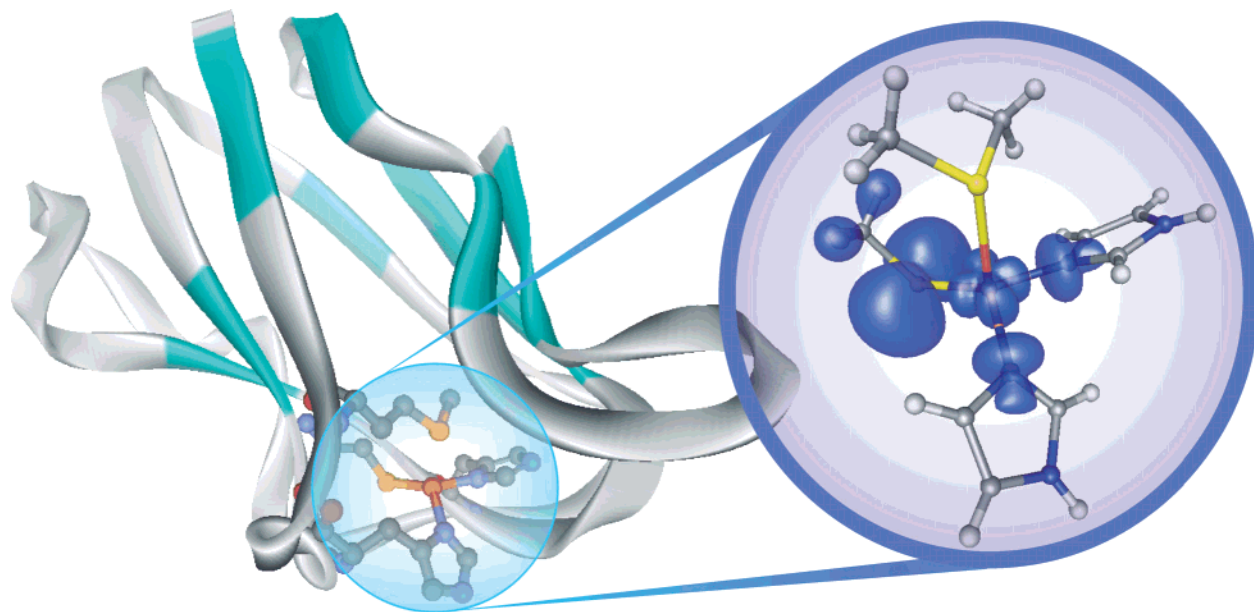


Figure 1. Crystal structure of plastocyanin (PDB code 1PLC) and an expanded view of the geometric and electronic structure of the active site.

ting, which also dramatically affects the EPR spectrum.

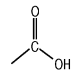
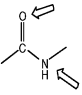
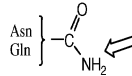
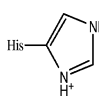
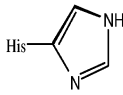
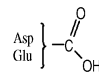
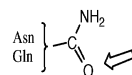
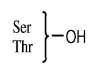
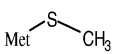
To higher photon energy (i.e., the near infrared and visible spectral regions), the electrons are excited from the filled d orbitals to the singly occupied or unoccupied metal valence orbitals. These are the LF or $d \rightarrow d$ transitions. The energy splitting of the metal-based d orbitals is accurately given by LF theory as long as the site is not overly covalent. These transitions provide sensitive probes of the geometric and electronic structure of an active site. The LF, $d \rightarrow d$ transitions are studied in small molecule inorganic complexes with electronic absorption spectroscopy (ABS). These transitions are parity (or Laporté) forbidden and often cannot be observed in the absorption spectrum of dilute metalloproteins. However, different spectroscopic methods are governed by different selection rules. Absorption intensity is governed by the square of the electric dipole transition moment. Alternatively, circular dichroism (CD) is dependent on the scalar product of the electric and magnetic dipole transition moments. Because LF transitions are often magnetic dipole allowed, these can be intense in the CD spectrum relative to the absorption spectrum. Magnetic circular dichroism (MCD) requires contributions from two perpendicular electric dipole transition moments. In low symmetry sites, electronic transitions can only be unidirectional. Therefore, paramagnetic active sites derive low-temperature MCD (LT MCD; called a C term) intensity by spin-orbit coupling between excited states. (A second mechanism for MCD intensity involves spin-orbit coupling between the ground state and an excited state.) Because the metal has a much larger spin-orbit coupling constant than the ligand, metal-centered $d \rightarrow d$ transitions will generally also be intense in the LT MCD relative to the absorption spectrum.

Overlapping the LF transitions and to higher energy in the visible/UV spectral regions are the CT transitions, which involve excitation of electrons from filled valence orbitals on the ligand to the singly

occupied or unoccupied valence orbitals on the metal center. Because the intensity of a CT transition reflects the overlap of the donor and acceptor orbitals involved, these are very sensitive probes of specific ligand-metal bonding interactions. From the above discussion, CT transitions can be distinguished from the LF transitions by the different selection rules involved in ABS/CD/MCD spectroscopies. CT transitions are generally intense in absorption (because they are electric dipole allowed) and weak in the CD and LT MCD spectra. The specific assignment of these transitions requires additional spectral insight. In single crystals, the polarizations of the electronic transitions allow their assignment to specific ligand-metal bonds. This, however, is a very difficult experiment, and new methodologies have been developed that allow these polarizations to be obtained for metalloproteins in solution (see ref 15). A complementary probe is resonance Raman spectroscopy. The high intensity of the CT transitions ($\epsilon \geq 1000 \text{ M}^{-1} \text{ cm}^{-1}$) allows resonance enhancement of Raman vibrations, and the vibrations that are resonance enhanced reflect the change in bonding that occurs in the electronic transition.

At still higher energy (X-ray region) are transitions from the filled core orbitals on the metal and ligand into the partially occupied or unoccupied valence orbitals on the metal ion and into the continuum. The most well-known X-ray absorption spectroscopic (XAS) method is metal K-edge spectroscopy, in which the ionized metal $1s$ electron reflects off the ligand atoms leading to interference effects on the metal K-edge (i.e., extended X-ray absorption fine structure, EXAFS). On the low-energy side of the metal K-edge are bound state transitions of the metal $1s$ electrons into the metal $3d$ and $4p$ orbitals. These can provide insight into the oxidation state, spin state, and coordination number and environment of the metal center. Whereas the metal K-edge is a low-resolution probe of the active site (this is because of its high energy, lifetime, and the

Table 1. Endogenous Biological Ligands

A. polypeptide chain		intrinsic pK _a (±1 log units in protein)
N-terminus	—NH_3^+	8
C-terminus		4
carbonyl of chain		—
amide of chain		~13
B. Residues		
N Donors		
amine	Lys—NH ₃ ⁺	10
amide		14
imidazole		6-7
imidazolate		~14
O Donors		
carboxylate		4-5
carbonyl		—
phenol	Tyr—OH	10
alcohol		14
S Donors		
thioether		—
thiolate	Cys—SH	8.5

fact that the 1s→3d transition is not electric dipole allowed), the metal L-edge and ligand K-edge can provide higher resolution probes of a metal center, and in particular, their intensities provide a very direct method to quantitate covalency of the metal d-based MOs.^{16–18} This is described in section 3.2.

All of the above methods involve excitation of electron to bound excited states. In photoelectron spectroscopy, one studies ionized electrons; thus, this method is not limited to transitions to partially occupied valence orbitals and can be used to probe any metal complex (e.g., Cu^I, which has a closed shell 3d¹⁰ configuration). However, because of limitations associated with the escape depth of the electron, the

Table 2. Exogenous Biological Ligands

		intrinsic pK _a (±1 log unit in protein)
acid–base	H ₂ O/OH [−] /O ^{2−}	14.0, ~34
	HCO ₃ [−] /CO ₃ ^{2−}	10.3
	HPO ₄ ^{2−} /PO ₄ ^{3−}	12.7
	HO ₂ /O ₂ [−]	4.9
	HCO ₂ [−]	3.8
	CH ₃ CO ₂ [−]	4.7
	HO ₂ [−]	11.6
	NH ₃	9.3
	imidazole	7.0
	pyridine	5.3
	N ₃ [−]	4.8
	−NCO [−]	3.7
	−NCS [−] , −SCN [−]	1.0, −1.9
	NO ₂ [−]	3.3
	HSO ₃ [−] /SO ₃ ^{2−}	7.0
	HCN/CN [−]	9.3
	H ₂ S/HS [−] /S ^{2−}	7.0, 12
F [−] , Cl [−] , Br [−] , I [−]	3.5, −7, −9, −11	
neutral	O ₂ , CO, NO, RCN, N ₂	
N-heterocycles	chlorines, corrins, hemes, isobacteriachlorins	2.7–5.5, 9.5–11.2
cofactors	pterins, α-ketoglutarate	1.8–4.1, 2.4

photoelectron experiment should be done on relevant active site model complexes rather than the complete protein system. There are two regions of focus in variable energy photoelectron spectroscopy (VEPES) experiments. One involves ionization of core electrons (X-ray photoelectron spectroscopy, XPS), the energy giving a direct probe of the effective nuclear charge on the atom and the intensity pattern (shake up satellites and multiplet effects) giving insight into ligand donor and acceptor bonding. Photoelectron spectroscopy at lower energy probes the valence orbital region (ultraviolet photoelectron spectroscopy, UPS), which gives a sensitive probe of the ligand–metal bonds. However, traditional UPS (utilizing HeI at 21.2 eV and HeII at 40.8 eV photons) can be ambiguous in peak assignments. The use of synchrotron radiation in allowing VEPES has revolutionized this method.^{12,19} Changes in the photon energy change the intensity of VEPES features, which through cross-section effects define the ligand and metal character in an orbital from which the electron is ionized, hence its covalency. Also, for many complexes, the electronic structure changes dramatically on ionization due to changes in electron repulsion, and this can also be quantitated by VEPES through resonance effects, which define the nature of the final states. This electronic relaxation has recently been shown using VEPES to be an important contribution to the redox properties of the iron sulfur centers.^{20–22}

While spectroscopy provides experimental probes of the energy level diagram in Figure 3, major advances have also recently been made in calculating the electronic structures of metalloenzyme active sites. The traditional methods of LF theory, and extended Hückel,^{23,24} semiempirical,^{25–27} and ab initio (with correlation) molecular orbital theory (MOT)²⁸ have been strongly complemented by density functional theory (DFT).²⁹ These theoretical methods [Xα-sw,^{30–33} local density approximation (LDA)^{34–36}], generalized gradient approximation (GGA)^{37–39}, and hybrid (for example, B3LYP^{40–42}), for the first time, routinely allow high-level calculations on large tran-

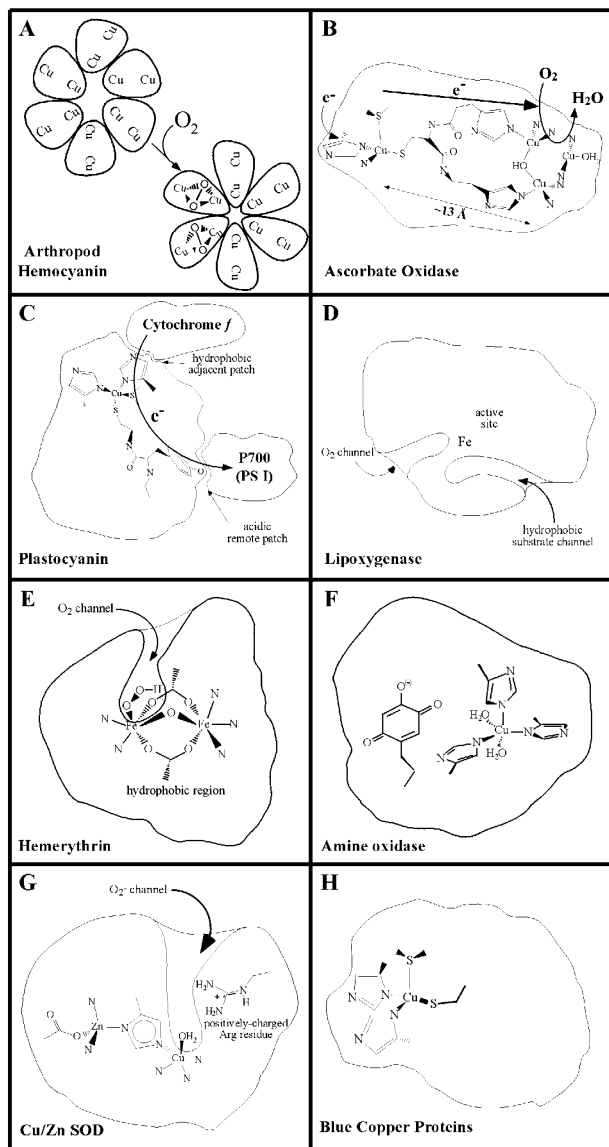


Figure 2. Roles of protein ligands in biological function. (A) Allosteric interactions between active sites in different subunits; (B) organization of sites within a multicenter enzyme; (C) surface recognition sites and superexchange pathways for ET; (D) forming substrate access channels to the active site; (E) hydrophobic environment; (F) protein pocket for substrate binding and activation near the metal active site; (G) specific charge and H-bonding residues near the metal site to assist catalysis; and (H) imposing a unique geometry on the metal site, which can activate it for reactivity. Adapted from ref 3.

sition metal systems, as is required for metalloprotein active sites. Here, it should be emphasized that it is critically important to evaluate DFT methods with spectroscopic data. There is a tendency in DFT calculations,^{43,44} for at least some metal ions, to overemphasize the covalency (the amount of ligand character in a metal d orbital), which will affect total energies. Methods that adjust these calculations on the basis of experimental data are now being developed (see section 2.2). Calculations supported by data can be used to define new bonding interactions and extend our understanding from known species (reactants, products, and intermediates) to obtain total reaction energies and evaluate reaction coordinates and transition states in catalysis.

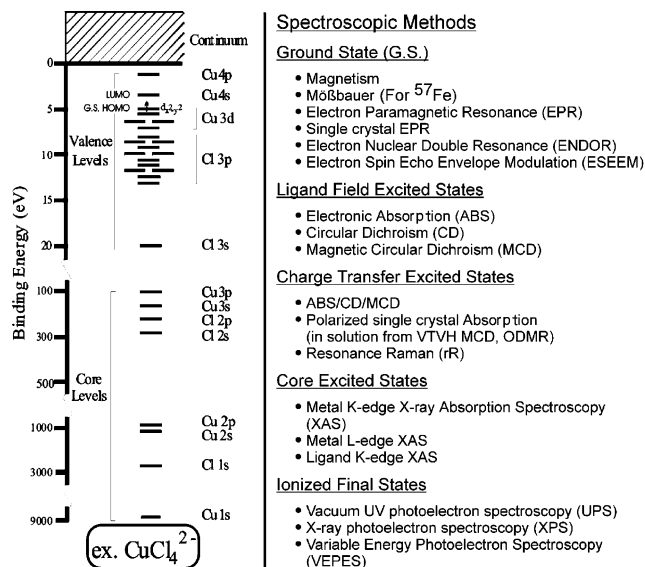


Figure 3. Complete MO diagram of $[\text{CuCl}_4]^{2-}$ (left) and an overview of different spectroscopic methods to probe the ground state and various excited states (right). Adapted from ref 14.

This leads to the goals of spectroscopy in bioinorganic chemistry. Generally, these are to define active site geometric and electronic structure and to use these to develop structure/function correlations in biology. Combined with perturbations (i.e., substrate, cofactor, and small molecule binding, etc.), spectroscopy will provide insight into a reaction mechanism on a molecular level. Rapid freeze quench and related kinetic methods allow one to identify and trap the intermediates in a reaction, the nature of which can be determined through detailed spectroscopic study. Often, fundamental insight requires the development of new spectroscopic methods and the interpretation of unique spectroscopic features observed for some active sites (relative to small molecule inorganic complexes of the same metal ion) using existing spectroscopic methods. As emphasized above, unique spectral features can reflect novel geometric and electronic structures and involve highly covalent ligand–metal bonds, which can activate a metal site for catalysis.

In many ways, the blue copper site reflects the impact and evolution of spectroscopy in bioinorganic chemistry, its use in defining electronic structure, and the possible role of the protein in affecting geometric and electronic structure (i.e., the entatic or rack-induced state).^{6,8,10,11} However, to recognize the uniqueness of the structure and spectroscopy of the blue copper center (Figure 1, blow up, structure described in section 3), it is important to first develop the basic spectroscopy of “normal” cupric complexes. To this end, square planar $[\text{CuCl}_4]^{2-}$ has been studied over the 10 orders of magnitude in photon energy summarized above. Its basic spectroscopy is presented in section 2 and then used to evaluate the results from modern DFT calculations.

2. Electronic Structure of D_{4h} $[\text{CuCl}_4]^{2-}$

2.1. Spectroscopy

Placing a cupric ion ($3d^9$) into an octahedral field of chloride ligands splits the d orbitals as indicated

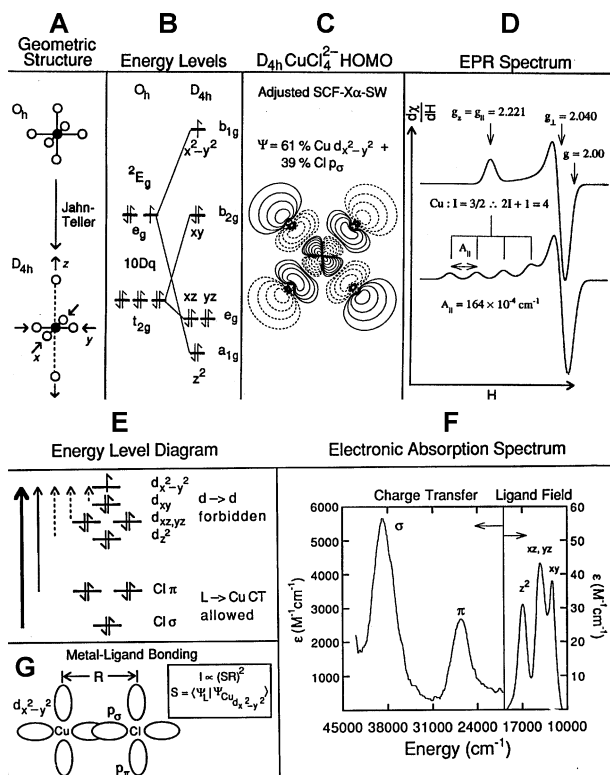


Figure 4. Ground and excited state spectral features of D_{4h} $[\text{CuCl}_4]^{2-}$. Adapted from ref 76.

in Figure 4B (the e_g above the t_{2g} set by $10Dq$) and generates a 2E_g ground state. This is orbitally degenerate, and electron–nuclear coupling between the degenerate levels leads to a Jahn–Teller distorting force, which lowers the symmetry and energy of the complex. The Jahn–Teller distortion generally observed in cupric complexes is a tetragonal elongation (Figure 4A, bottom), and in the limit of a large Jahn–Teller effect, this leads to square planar, D_{4h} $[\text{CuCl}_4]^{2-}$. A key point of LF theory is that the energy splitting of the d orbitals is sensitive to the geometry about the metal center, and in a square planar LF, the energy splitting obtained is given in Figure 4B, right. The $3d_{x^2-y^2}$ orbital is at highest energy, as it has its lobes oriented along the four chloride ligands in the equatorial plane and thus is subject to the largest repulsive/antibonding interactions. The rest of the orbital energies are obtained from polarized spectroscopy (vide infra). This square planar splitting of the d orbitals leads to an unpaired electron in the $3d_{x^2-y^2}$ orbital, which defines the ${}^2B_{1g}$ ground state of D_{4h} $[\text{CuCl}_4]^{2-}$. This is actually a MO with dominantly Cu 3d character but delocalized onto the four chloride ligands, which are involved in σ antibonding interactions with the $3d_{x^2-y^2}$ orbital (Figure 4C). This complex has been subject to the wide range of spectroscopic methods defined by the energy diagram in Figure 3. These accurately quantitate the ground state as having 39% chloride σ^* character mixed into the $3d_{x^2-y^2}$ orbital due to covalency (see Table 3 top, averaged over methods).

As summarized in the Introduction, the ${}^2B_{1g}$ ground state of D_{4h} $[\text{CuCl}_4]^{2-}$ is studied at high resolution using EPR spectroscopy. For an unpaired electron in a $3d_{x^2-y^2}$ -based MO, LF theory as described in sec-

Table 3. Summary of Spectroscopic Data for D_{4h} $[\text{CuCl}_4]^{2-}$

Ground State		
experimental method		Cu 3d character of the HOMO (%)
g value EPR, adjusted X α -sw		61
copper hyperfine EPR		67
chloride superhyperfine EPR		64
LF and CT energies CI model		56
core level excitations XPS satellite		60
valence level excitations VEPES		65
Excited State		
	excitation ($f x^2 - y^2$)	transition energy (cm^{-1})
LF transition	${}^2A_{1g}$ (z^2)	16 500
	${}^2E_{1g}$ (xz, yz)	13 500
	${}^2B_{2g}$ (xy)	12 000
CT transition	${}^2A_{2g}$ (p)	23 700
	${}^2E_{1u}$ (p)	26 400
	${}^2E_{1u}$ (s)	35 900

tion 3.1.2 gives $g_{||} > g_{\perp} > 2.0023$, with $g_{||}$ being the Zeeman splitting of the spin doublet with the magnetic field oriented along the molecular z -axis (Figure 4D, top) and g_{\perp} the splitting with the magnetic field in the equatorial plane. Note from Figure 4D, top, that the EPR spectrum is plotted as the first derivative of the microwave absorption to increase sensitivity, which leads to a peak at $g_{||}$ and an intense derivative-shaped feature with a crossing point at g_{\perp} in the EPR spectrum^{12,13} of a powder or frozen solution of D_{4h} $[\text{CuCl}_4]^{2-}$. As shown at the bottom of Figure 4D, copper has a nuclear spin I of $3/2$, which will couple to the electron spin and produce a hyperfine splitting of the EPR signal into $2I + 1 = 4$ lines. From the experimental spectrum, the hyperfine coupling in the $g_{||}$ region, $A_{||}$, is much larger than in the g_{\perp} region, A_{\perp} , and $A_{||}$ is generally large for tetragonal cupric complexes. The origin of this metal hyperfine coupling is considered in section 3.1.1 relative to the small $A_{||}$ value observed for blue copper sites.

Figure 4E gives an expanded portion of the ligand and metal valence orbital energy region of Figure 3, which correlates to the absorption spectrum in the near-infrared/visible/ultraviolet region in Figure 4F. Transitions within the d manifold (d→d or LF transitions of an electron into the $3d_{x^2-y^2}$ hole) are parity forbidden and therefore weak in the absorption spectrum contributing in the low energy ~ 600 nm region ($\epsilon < 50 \text{ M}^{-1} \text{ cm}^{-1}$, Figure 4F, scale to right). The specific assignments of the bands listed at the top of the spectrum derive from polarized single-crystal spectroscopy combined with vibronic selection rules. To higher energy are the intense ($\epsilon < 10^3 \text{ M}^{-1} \text{ cm}^{-1}$, Figure 4F, scale to left) ligand to metal CT transitions, which involve excitation of an electron from a MO dominantly on the ligand (bonding) to one dominantly on the metal (antibonding). These result in transfer of charge and are electric dipole allowed. Analysis of CT transitions requires specific consideration of the nature of the ligand valence orbitals involved in bonding to the metal (Figure 4G). Each chloride ligand will donate three valence 3p orbitals, which split into two sets: a $3p_z$ orbital oriented along the ligand–metal bond, which is σ bonding to the

metal, and two $3p_{x,y}$ orbitals perpendicular to the ligand–metal bond, which are π interacting with the metal and thus at higher energy (i.e., less bonding).

As diagramed in Figure 4G, the intensity in absorption is proportional to the overlap of the donor and acceptor orbitals involved in the CT process. Because the ligand $3p_{\sigma}$ orbital has strong overlap with the Cu $3d_{x^2-y^2}$ acceptor orbital, it will produce an intense CT transition at high energy (due to the σ bonding). Alternatively, the π CT has no direct overlap with $3d_{x^2-y^2}$ but acquires some intensity through configuration interaction (since the σ and π CTs both have 2E_u symmetry in the complete D_{4h} point group of $[\text{CuCl}_4]^{2-}$). The assignment of these CT transitions to specific orbitals of the four chloride ligands is derived from polarized reflectance data,⁴⁵ the Kramers–Krönig transformation of which provides polarized absorption data into the intense CT region of single crystals of D_{4h} $[\text{CuCl}_4]^{2-}$.

The definitively assigned absorption spectrum of D_{4h} $[\text{CuCl}_4]^{2-}$ in Figure 4F nicely illustrates the absorption features of normal cupric complexes: weak LF transitions in the $\sim 16\,000\text{ cm}^{-1}$ (600 nm) region and intense CT transitions at higher energy. The σ CT is extremely intense, and the low energy π CT is weak due to differences in overlap with the $3d_{x^2-y^2}$ acceptor orbital, which has its lobes oriented along the metal–ligand bond in Figure 4G due to the dominant σ antibonding interactions with the ligands.

2.2. Evaluation and Calibration of DFT Calculations

2.2.1. Correlation to Spectroscopy

Spectroscopic data including ground state spin densities, excitation energies, and their assignments for D_{4h} $[\text{CuCl}_4]^{2-}$,^{46,47} as summarized in Table 3, provide a basis for evaluation of modern DFT calculations. A pure or GGA density functional, BP86,^{40,48} and two hybrid functionals, B3LYP^{40–42} and BHandHLYP,⁴⁹ were evaluated. In addition to the type of functional, the quality of the basis set employed is also important. Figure 5 shows the basis set dependence of the three functionals evaluated

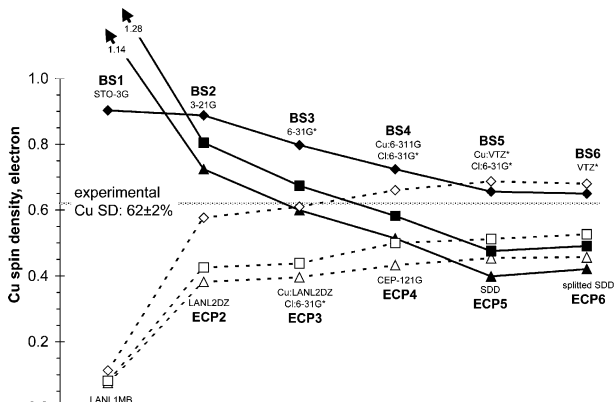


Figure 5. Cu atomic spin densities in D_{4h} $[\text{CuCl}_4]^{2-}$ using the experimental geometry with selected density functionals and basis sets by means of a MPA (triangle, BP86; rectangle, B3LYP; diamond, BHandHLYP; hollow symbol, effective core potential and valence basis set; and filled symbol, all electron basis set). Adapted from ref 43.

based upon the total Cu atomic spin density by means of the Mulliken population analysis (MPA).⁵⁰ As concluded from past calculations on similar systems,^{10,43,51} a combination of triple- ζ basis with polarization function for the metal⁵² and double- ζ basis with polarization for the ligands^{53–55} (BS5) is sufficient and the use of a more extensive basis set does not significantly improve the electronic structure description.

Considering the Cu atomic spin densities as the reflection of the ground state covalency calculated by the three functionals with basis set BS5 (Figure 5), we found that the GGA density functional (BP86) gives a ground state that is too covalent (43% Cu character vs 62% from experiment). The use of the hybrid functional B3LYP improves the ground state description (55% Cu character); however, it is still too covalent. In case of the other hybrid functional BHandHLYP, which contains approximately twice as much HF exchange relative to B3LYP, the ground state becomes too ionic (67% Cu character) relative to experiment.

Variation in the functional has a parallel effect on the LF and CT excitation energies (Figure 6). In the

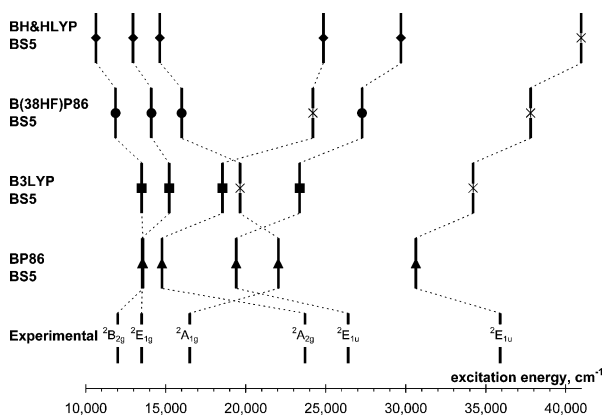


Figure 6. Experimental and calculated Δ SCF LF and CT excitation energies (triangle, BP86; rectangle, B3LYP; diamond, BHandHLYP; filled symbol, all electron basis set (BS5); cross indicates collapse to a different state and is estimated from TDDFT calculation).

case of the BP86 functional, the LF transitions are shifted to higher and the CT transitions to lower energies relative to experiment. The B3LYP hybrid density functional adjusts the relative positions of the transition energies to give better agreement with experiment. The BHandHLYP functional reverses the relative order of excited states and gives too low LF and too high CT transition energies.

Both ground and excited state descriptions indicate that the GGA DFT gives an excessively covalent ground state bonding description where the Cu 3d manifold is stabilized relative to the donor ligand orbitals resulting in too much ligand character in the singly occupied MO and high LF and low CT transition energies. In going from the BP86 to B3LYP and to the BHandHLYP functionals, the improved ground and excited state descriptions originate from the inclusion of an increased amount of Hartree-Fock (HF) exchange (0, 20, and 50%, respectively). The effects of the different ratios of HF exchange mixing

indicate that there is an optimum between 20 and 50%, which gives a good match to the experimental ground state spin density and excitation energies.

On the basis of the calculated ground state spin density, replacing 38% of the total Density Functional (DF) exchange by HF exchange is needed to match the experimental spin density. Variation in the correlation functional, i.e., the use of P86 vs LYP, did not affect the spin density by more than 2%. Using this spectroscopically adjusted hybrid functional (B(38HF)-P86) with a converged basis set (BS5), the LF and CT excitation energies also become reasonably close to the experimental value (within 1000 cm^{-1}).

In computational packages, such as Amsterdam Density Functional (ADF),^{56–60} where the adjustment of HF exchange is not available, alternative approaches can be used. To destabilize the metal 3d manifold and hence adjust the covalency, the nuclear charge of the metal can be reduced or an excess effective potential around the core can be defined using ECP basis set formalism. For example, a decrease in the Cu nuclear charge by 0.45 electron ($Z_{\text{eff}} = 28.55$) matches the experimental 62% Cu character of the highest occupied molecular orbital (HOMO) in the D_{4h} $[\text{CuCl}_4]^{2-}$. The LF and CT transition energies show a significant improvement as well. This Z_{eff} value has been successfully applied for other Cu^{II} -containing molecules, such as blue and green Cu active sites (vide infra).

It is interesting to compare the performance of DFT calculations to ab initio MO calculations, where the level of theory can be systematically varied. Figure 7 summarizes the Cu spin densities by MPA from

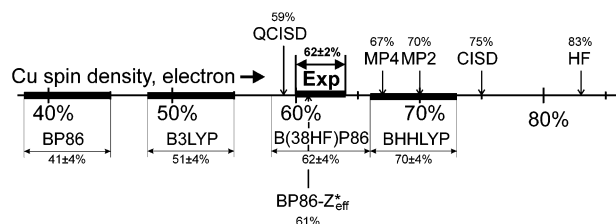


Figure 7. Cu atomic spin densities in D_{4h} $[\text{CuCl}_4]^{2-}$ (experimental geometry) for selected density functionals and ab initio methods calculated using BS5. The ranges for the DFT calculations indicate the population analysis dependence by means of Mulliken, Weinhold natural, and Bader AIM population analysis methods.

DFT and ab initio calculations performed using BS5. The pure HF calculation gives a highly ionic bonding description with 83% spin density located on the Cu atom, which is improved by taking into account electron correlation. Møller–Plessets perturbation theory^{61–65} up to the fourth order⁶⁶ converges toward a reasonable bonding description (67%), and the QCISD⁶⁷ approach gives a good agreement (60% by Mulliken population analysis) with the experimental Cu spin density (62%).

2.2.2. Potential Energy Surface (PES)

The D_{4h} structure of $[\text{CuCl}_4]^{2-}$ corresponds to a transition state in the gas phase and distorts to a flattened tetrahedral geometry with D_{2d} symmetry due to significant ligand–ligand repulsion. To obtain a square planar geometry without any imposed con-

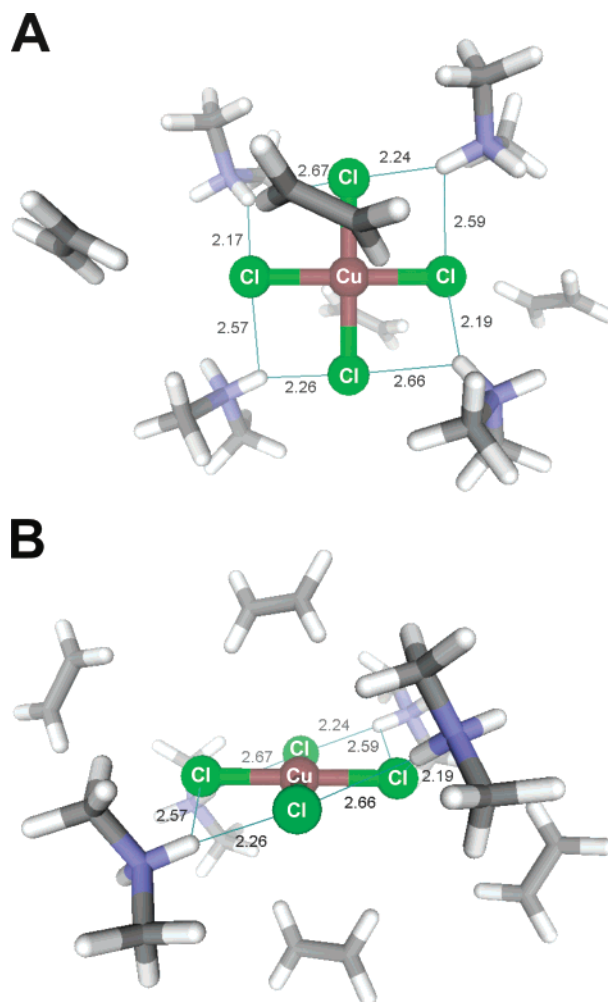


Figure 8. Smallest model of the tetragonal $[\text{CuCl}_4]^{2-}$ crystal structure, which prevents the D_{2d} tetrahedral distortion upon geometry optimization (A, top view; B, side view). Adapted from ref 43.

straints on the complex, a crystal lattice environment⁶⁸ needs to be constructed (Figure 8). In this model, the proximal H-atoms of the ammonium counter ions form a network of hydrogen bonds (indicated by thin lines in Figure 8), which reduce the ligand–ligand repulsion and successfully prevent the D_{2d} distortion.

The optimized internal coordinates of the $[\text{CuCl}_4]^{2-}$ with three functionals are summarized in Table 4.

Table 4. Optimized Minimum and Maximum Values of Cu–Cl Bond Lengths (r), Cl–Cu–Cl Bond Angles (θ), and Cl–Cu–Cl...Cl Out of Plane Angles (ω) and Cu Mulliken Atomic Spin Densities (SD, Electron) of the Tetragonal $[\text{CuCl}_4]^{2-}$ Complex in the Solid State (Using BS5 for the Complex and BS2 for the Environment; See Figure 5)

functional	r (Å)	θ (deg)	ω (deg)	SD
BP86	2.304–2.312	89.5–90.5	–0.5–0.3	0.42
B3LYP	2.313–2.319	89.5–90.5	–0.5–0.4	0.50
B(38HF)P86	2.288–2.290	89.7–90.5	–0.4–0.2	0.60
B(38HF)LYP	2.311–2.314	89.7–90.5	–0.4–0.4	0.61
BHandLYP	2.310–2.312	89.7–90.5	–0.3–0.4	0.68
experiment	2.248–2.281	90.1–89.9	0.0	0.62 ± 0.02

The Cl–Cu–Cl bond angles and Cl–Cu–Cl...Cl out of plane angles do not show a significant dependence

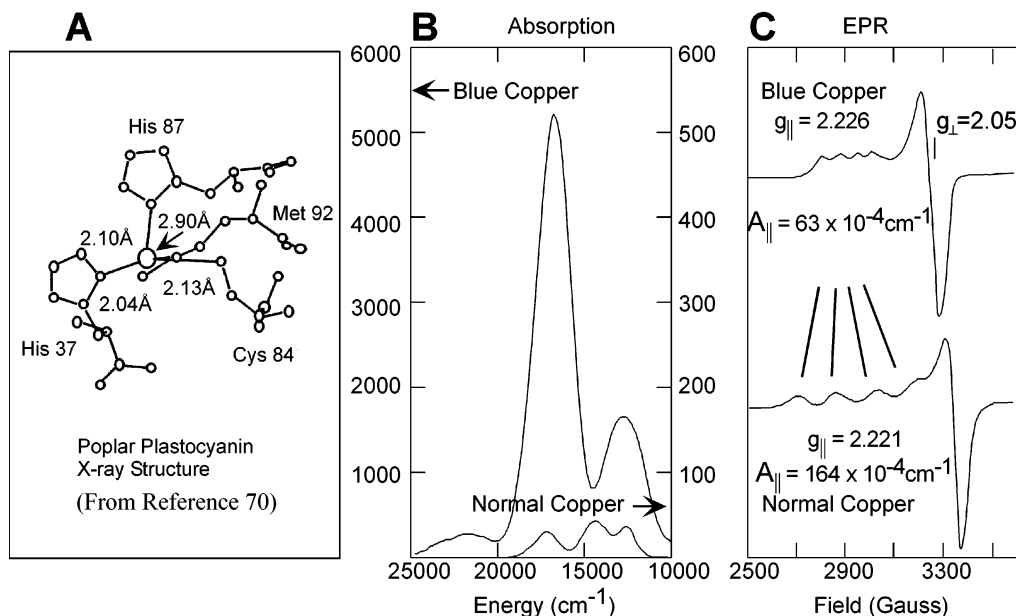


Figure 9. (A) X-ray structure of the blue copper site in poplar plastocyanin. (B) Absorption spectrum of plastocyanin (left ϵ scale) and “normal” D_{4h} $[\text{CuCl}_4]^{2-}$ (right ϵ scale). (C) X-band EPR spectrum of plastocyanin (top) and D_{4h} $[\text{CuCl}_4]^{2-}$ (bottom). Adapted from refs 3 and 70.

on the functional employed, which implies that these internal coordinates are primarily determined by the lattice environment. As seen for the gas phase calculations, the Cu atomic spin densities and the Cu–Cl bond lengths are affected by change in the functional, and the spectroscopically adjusted B(38HF)P86 functional gives the closest agreement with experiment. In addition to the stationary points, the Cu–Cl stretching frequencies were also evaluated ($\nu_{a_{1g}}$). The BP86 functional was found to slightly underestimate (261 cm^{-1}) and the B(38HF)P86 hybrid method overestimate (282 cm^{-1}) the experimental value (276 cm^{-1}).

While variations in the amount and type of correlation functional (P86 vs LYP) do not effect the Cu spin density by more than 1%, these do produce significant differences in the Cu–Cl bond length. The gas and solid phase calculated geometries of the tetragonal $[\text{CuCl}_4]^{2-}$ were in better agreement with experiment using the P86 functional as compared to LYP. A decrease of approximately 20% in the total DF correlation, as is in B3LYP, also gives less accurate optimized geometries.

The overall effect of variation in the HF exchange and the type and amount of DF correlation (BP86, B3LYP, B(38HF)P86, and BHandHLYP) on the PES properties are comparable. Relaxed PES scans revealed that the PES around the solid phase tetragonal $[\text{CuCl}_4]^{2-}$ is flat. Stretching of all four Cu–Cl bonds by 0.1 Å (along the a_{1g} coordinate) costs less than 1 kcal mol^{-1} per bond. Alternatively, in the gas phase, D_{4h} to D_{2d} distortion occurs along the b_{2u} normal coordinate involving mainly angular changes, which is worth 6–9 kcal mol^{-1} depending on the functional used.

In summary, the spectroscopically adjusted hybrid density functional B(38HF)P86 gives better ground and excited state bonding and improved PES descriptions relative to the generally used GGA and

hybrid functionals. For the $[\text{CuCl}_4]^{2-}$ complex, improvements have been achieved in atomic spin density by 20%, in LF and CT excitation energies by 2- and 10-fold, respectively (both are within 1000 cm^{-1} of experiment), in bond lengths by 0.03 Å, in the a_{1g} breathing mode by 30 cm^{-1} , and in the corresponding force constant by nearly 30%. The stabilization of the D_{2d} structure using the B(38HF)P86 functional (9 kcal mol^{-1}) increases by 3 kcal mol^{-1} , and the heterolytic bond dissociation energy of the first Cu–Cl bond in water (6 kcal mol^{-1}) becomes more endothermic by the same amount relative to the BP86 calculations.

3. Electronic Structure of Oxidized Blue Copper Sites

As first indicated by spectroscopy,⁶⁹ the geometric structure of the blue copper site in plastocyanin (first structurally defined by Hans Freeman;⁷⁰ Figure 9A) is very different from that of tetragonal cupric complexes in that it has a distorted tetrahedral geometry with an unusually short $\text{Cu}^{\text{II}}\text{--S}$ (thiolate) bond from Cys84 and an unusually long $\text{Cu}^{\text{II}}\text{--S}$ (thioether) bond from Met92.^{70,71} The remaining two ligands are His with fairly normal $\text{Cu}^{\text{II}}\text{--N}$ (His) bonds. Associated with this unusual geometry and ligation are the unique spectroscopic features of the blue copper center shown in Figure 9B,C.^{11,72–77} In the absorption spectrum of blue copper sites, instead of the weak LF transitions in the red (~ 600 nm, 16 000 cm^{-1}) spectral region of tetragonal Cu^{II} , there is an extremely intense absorption band ($\epsilon \sim 5000$ $\text{M}^{-1} \text{cm}^{-1}$) at ~ 16 000 cm^{-1} . Furthermore, in the EPR spectrum, the parallel Cu hyperfine coupling (A_{\parallel}) is reduced by more than a factor of 2 in the blue copper site relative that of tetragonal Cu^{II} complexes (Figure 9C). In this section, we develop the concept that these unique spectroscopic features reflect a highly covalent ground state wave function. For Cu^{II} complexes, this is the

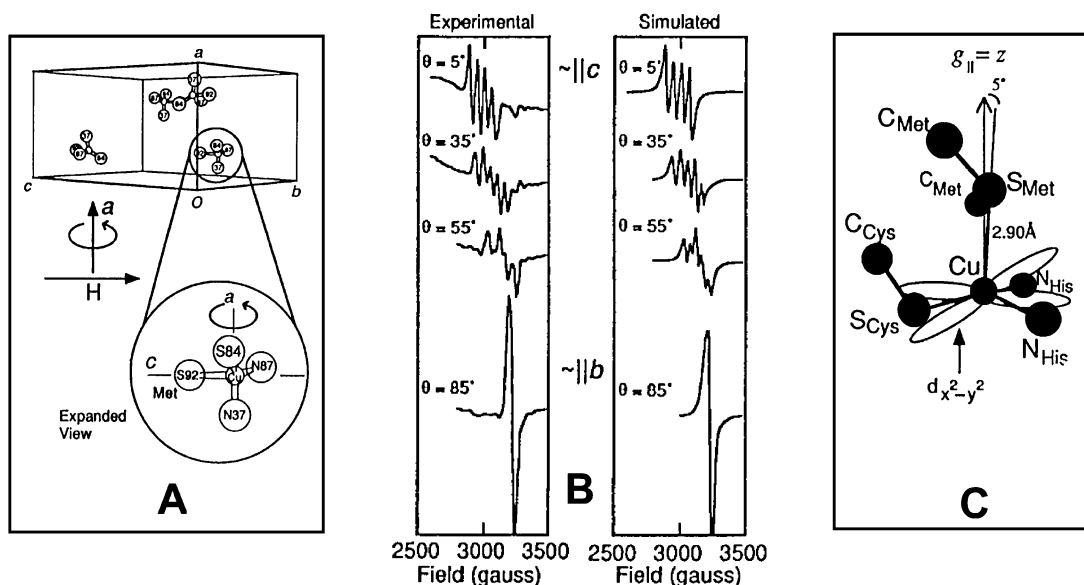


Figure 10. Single-crystal EPR of poplar plastocyanin; orientation of the $3d_{x^2-y^2}$ orbital. (A) Unit cell and molecular orientation of poplar plastocyanin with respect to the applied magnetic field. θ is the angle between the magnetic field (H) and the crystallographic c -axis ($\theta = 0$; H and c are collinear). (B) EPR spectra and simulations for the crystal orientations shown. (C) Orientation of the $g_{||}$ direction and the $3d_{x^2-y^2}$ orbital superimposed on the blue copper site. Adapted from ref 78.

redox active orbital and this high covalency activates the blue copper site for its biological function of long-range, rapid, directional ET (see section 7).

3.1. Orientation of the Ground State: Single-Crystal EPR

From Figure 9C, $g_{||} > g_{\perp} > 2.0023$, which indicates (from LF theory, see section 3.1.2) that the unpaired electron of the blue copper ground state is in a $3d_{x^2-y^2}$ -derived MO. The first step in understanding the ground state is to determine the orientation of this orbital relative to the distorted tetrahedral structure of the blue copper site in Figure 9A. This was first accomplished by single-crystal EPR studies⁷⁸ on plastocyanin (the equivalent results were later obtained for azurin in ref 79). This protein crystallized in an orthorhombic space group with four molecules in the unit cell (Figure 10A).⁷⁰ EPR spectra were taken while rotating a plastocyanin crystal around specific axes oriented perpendicular to the magnetic field. Representative spectra are shown in Figure 10B, left. Note that a $g_{||}$ EPR spectrum (with four parallel hyperfine lines) is observed when the field is approximately parallel to the c -axis, while a g_{\perp} (derivative shaped broad EPR signal without resolvable hyperfine components) is observed when the field is oriented approximately 90° off the c -axis. The c -axis corresponds to the approximate orientation of the long $\text{Cu}^{\text{II}}-\text{S}(\text{Met})$ bond. The specific coordinates of the g matrix were obtained by simulating the single-crystal EPR data with four molecules in a unit cell (Figure 10B, right), giving the experimental orientation in Figure 10C. $g_{||}$ is within 5° of the long $\text{Cu}-\text{S}(\text{Met})$ bond, which puts the $3d_{x^2-y^2}$ orbital perpendicular to this bond and close to the plane of the strong $\text{S}(\text{Cys})$ and two $\text{N}(\text{His})$ ligands. It is important to emphasize that the single-crystal EPR data first defined the blue copper site to be a

trigonally distorted tetrahedral structure with the weak axial direction along the long $\text{Cu}-\text{S}(\text{Met})$ bond.

3.1.1. Origin of Small $A_{||}$: Copper K-Edge XAS

The next feature of the ground state to consider is the origin of the small $A_{||}$ value in Figure 9C. There are three dominant contributions to the metal hyperfine coupling (eq 1): (i) the Fermi contact term. This is isotropic ($A_{||} = A_{\perp}$) and associated with unpaired electron spin density at the nucleus. Because the blue copper site has an unpaired electron in a d orbital, which has no direct spin density at the nucleus, this contribution involves the unpaired $3d$ electron spin polarizing the inner $2s$ and $3s$ core electron pairs to produce a net negative spin density at the nucleus. (ii) The spin dipolar term. This is anisotropic ($A_{\perp} = -1/2A_{||}$) and involves the electron spin averaged over the shape of the $3d$ orbital, dipolar coupling to the nuclear spin on the metal. As shown in Figure 11, for an electron averaged on a $3d_{x^2-y^2}$

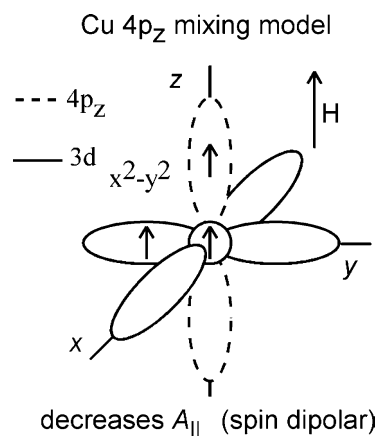


Figure 11. Geometric distortion model for small A values. $4p_z$ mixing with the $3d_{x^2-y^2}$ orbital in D_{2d} symmetry. Adapted from ref 78.

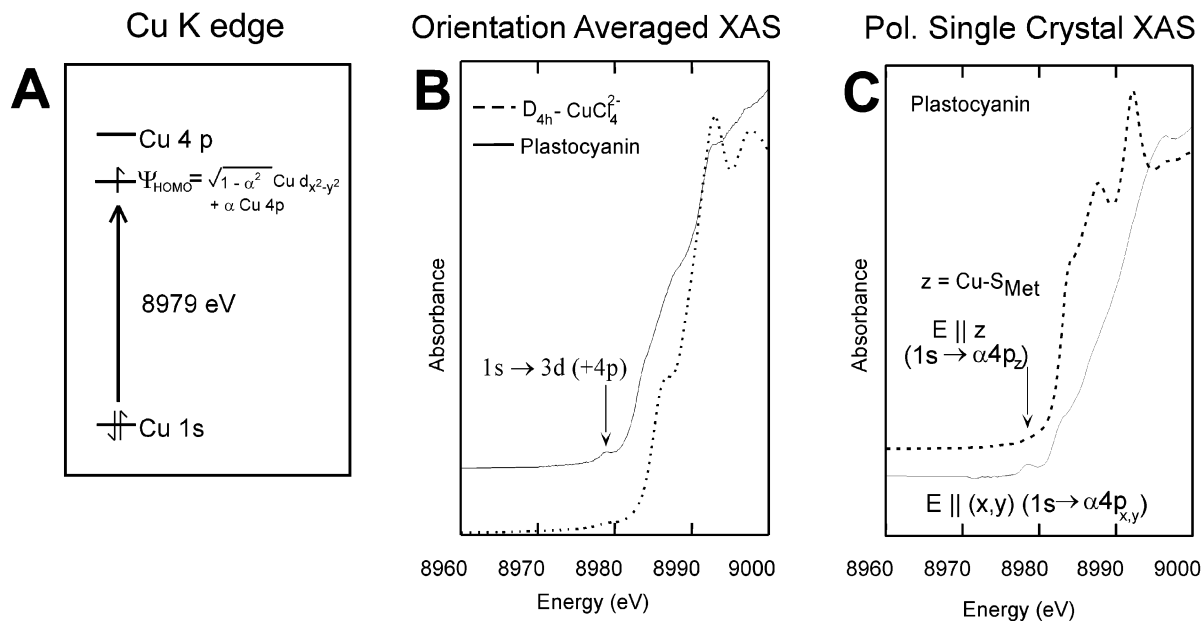


Figure 12. Cu K-edge XAS (A), orientation averaged XAS spectra of D_{4h} $[\text{CuCl}_4]^{2-}$ and the blue copper site in poplar plastocyanin (B), and polarized single-crystal XAS spectra for the poplar plastocyanin. Adapted from refs 85 and 86.

orbital with the magnetic field in the z direction (i.e., A_{\parallel} along g_{\parallel}), this involves an in plane parallel orientation of electron and nuclear spins giving a negative parallel hyperfine contribution. (iii) The orbital dipolar term. This is also anisotropic ($A_{\parallel} \neq A_{\perp}$) and involves the electron orbital angular momentum (which is spin-orbit mixed into the d electron ground state) dipolar coupling with the nuclear spin on the metal and is proportional to the g value deviations from 2.0023 (vide infra). The first and second terms are reduced by covalency (electron delocalization off the Cu $3d$ orbital and onto the ligands) while the third term contains covalency as it is obtained from the experimental g values.

$$A = A_F (\text{Fermi contact}) + A_S (\text{spin dipolar}) + A_L (\text{orbital dipolar}) \quad (1)$$

$$A_{\parallel}(D_{4h} [\text{CuCl}_4]^{2-}) = -123 \times 10^{-4} - 155 \times 10^{-4} + 114 \times 10^{-4} \text{ cm}^{-1} = -164 \times 10^{-4} \text{ cm}^{-1} \quad (2)$$

$$A_{\parallel}(\text{blue copper}) = -63 \times 10^{-4} \text{ cm}^{-1} \quad (3)$$

From eq 2, which gives the best estimates for the three contributions to A_{\parallel} for D_{4h} $[\text{CuCl}_4]^{2-}$, all are comparable in magnitude, the first two are negative and the orbital dipolar term is positive (note the negative sign, which is not defined in the standard EPR experiment but can be obtained from more advanced methods^{80–82}). As indicated above, the total A_{\parallel} hyperfine coupling constant is greatly reduced in magnitude for the blue copper site. The initial explanation for this reduction of $|A_{\parallel}|$ focused on the spin dipolar term in eq 1. In a distorted tetrahedral blue copper site, $3d_{x^2-y^2}$ could mix with the Cu $4p_z$ orbital. As shown in Figure 11, for the magnetic field along the z -axis, this would have the opposite sign of the spin dipolar interaction of the electron spin averaged over the $4p_z$ orbital (collinear, parallel

spins) relative to that of the $3d_{x^2-y^2}$ orbital and reduce the $|A_{\parallel}|$ value. Twelve percent $4p_z$ mixing into the $3d_{x^2-y^2}$ orbital in the blue copper site would give the small A_{\parallel} value observed experimentally.^{83,84}

This geometric distortion model for the small A_{\parallel} value of blue copper sites could be experimentally evaluated and eliminated through copper K-edge XAS.⁸⁵ As defined in Figure 12A, the lowest energy peak in the Cu K-edge (at 8979 eV) corresponds to a transition from the Cu $1s$ orbital to the singly occupied $3d_{x^2-y^2}$ -derived HOMO. Because $s \rightarrow d$ is electric dipole forbidden, the dominant electric dipole intensity mechanism contributing to this transition will be $s \rightarrow p$, therefore reflecting the $4p$ character mixed into the $3d_{x^2-y^2}$ orbital due to the distorted tetrahedral geometry of the blue copper site. From Figure 12B, the intensity of the 8979 eV feature in the XAS edge of plastocyanin has much more intensity than this feature in the D_{4h} $[\text{CuCl}_4]^{2-}$ spectrum reflecting the $4p$ mixing in blue copper. The key insight here was to determine the nature of the $4p$ mixing through the analysis⁸⁵ of polarized single-crystal XAS edge data.⁸⁶ Figure 12C shows the XAS spectrum obtained with a plastocyanin crystal oriented such that the \vec{E} vector of light is along the Cu–S(Met) bond, which from the single-crystal EPR data in section 3.1 is the electronic z -axis. This is the orientation where the 8979 eV peak intensity would reflect $4p_z$ mixing, and there is none. Alternatively, when the XAS spectrum is taken with the \vec{E} vector of the synchrotron radiation perpendicular to the z -axis (Cu–S(Met) bond), the 8979 eV intensity is high. This shows that the distorted tetrahedral structure mixes $4p_{x,y}$ into the $3d_{x^2-y^2}$ orbital, which would have the same sign for the spin dipolar term contributing to the A_{\parallel} term in Figure 11 and tends to increase not decrease A_{\parallel} . Thus, XAS data eliminated the original explanation of a small A_{\parallel} value for blue copper centers and shifted the focus to a highly covalent site. This will lower both A_F and A_S in eq 1

as covalent delocalization of the electron onto the ligand will reduce the electron hyperfine coupling to the nuclear spin on the Cu atom. This could be evaluated through a quantitative consideration of the EPR g values of the blue copper center.

3.1.2. Quantitative Analysis of g Values: Covalency

Table 5 gives the experimentally determined (S, X, and Q-band EPR) g values of plastocyanin. If the

Table 5. Quantitative Analysis of g Values for Plastocyanin

	experimental	$3d_{x^2-y^2}$ spin only	LFT d orbitals $\lambda L \cdot S$	X α -sw d levels, CT levels $\lambda_{Cu}L \cdot S + \lambda_L L \cdot S$	
				Norman radii	adjusted radii
g_x	2.047	2.000	2.125	2.046	2.059
g_y	2.059	2.000	2.196	2.067	2.076
g_z	2.226	2.000	2.479	2.159	2.226

ground state of this site could be described simply as an unpaired electron in a $3d_{x^2-y^2}$ orbital, the electron would only have spin angular momentum and this would lead to isotropic g values of 2.0023. LF theory allows for spin-orbit coupling of the $3d_{x^2-y^2}$ ground state with the higher energy d levels in Figure 4B, which mixes orbital angular momentum into the ground state and leads to anisotropic g values, which deviate from 2.0023. A complete LF calculation of the blue copper site gives the g values in the third column in Table 5, which have $g_{||} > g_{\perp} > 2.0023$ (consistent with a $3d_{x^2-y^2}$ -derived ground state). However, these deviate too much from 2.0023 relative to experiment. This reflects the fact that LF theory treats the d orbitals as having pure metal character. Covalent delocalization of these orbitals onto the ligands reduces their d character and hence the orbital angular momentum, bringing the g values closer to 2.0023.

This means that a proper description of the ground state of the blue copper site in plastocyanin requires MOT. This was initially accomplished using one of the earliest forms of DFT calculations known as SCF X α -scattered wave (X α -sw),^{33,36} an LDA method that only utilizes the Slater statistical approximation to exchange. It is insightful to consider the X α -sw results⁸⁷⁻⁸⁹ further here, while in section 3.3 we use the spectroscopic data on blue copper sites from sections 3.1 and 3.2 to evaluate the results of modern DFT calculations.

The X α -sw calculations of the blue copper site provide the antibonding metal-based (d-d) and bonding ligand-based (CT) valence orbitals. The g values were then evaluated by including spin-orbit coupling over all of these d-d and CT levels, which mixes orbital angular momentum from these levels into the ground state. The Zeeman effect associated with the magnetic field was then evaluated over this spin-orbit mixed ground state wave function to obtain a g matrix, which was diagonalized to get the principal g values and the orientation of the electronic axes. These calculations give the results in the fourth column in Table 5. Relative to the LF calculations (column 3 in Table 5), the g values are

reduced due to covalency, as anticipated. However, the X α -sw calculations give g values too close to 2.0023 relative to the experimental values.

This means that this calculation is giving too covalent a description of the blue copper active site based on experiment and emphasizes the fact that it is important to evaluate calculations with spectroscopy to determine their accuracy and relevance. There is one set of adjustable parameters in the X α -sw method, which is the sphere sizes used in constructing the scattered wave solutions. These were given by "Norman radii" named after J. Norman, who defined a set of criteria for overlapping spheres.^{33,90} Because these lead to an overly covalent description of the blue copper site, these sphere sizes were systematically adjusted until a bonding description was generated, which was supported by spectroscopy (i.e., a match of the calculated g values to experiment, first and last column in Table 5). This led in 1985⁸⁷ to the now well-known ground state wave function of the blue copper site in Figure 13.

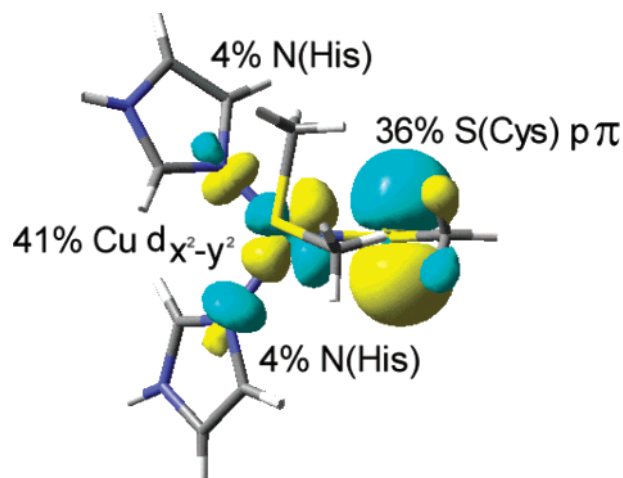


Figure 13. Contour of plastocyanin ground state wave function (β -LUMO) calculated by X α -sw.

Note that this is a contour in the x,y [S(Cys), two N(His)] plane. This experimentally adjusted X α -sw electronic structure calculation first suggested that there are three remarkable features of the ground state wave function of the blue copper site: (i) It is highly covalent with only 41% copper $3d_{x^2-y^2}$ character. (ii) The covalency is highly anisotropic and involves the Cu-S(Cys) bond. (iii) The $3d_{x^2-y^2}$ orbital is rotated such that its lobes, in fact, bisect the Cu-S(Cys) bond and thus is involved in a π antibonding interaction with the thiolate. These features of the ground state of the blue copper site could be evaluated experimentally using new spectroscopic methods as developed below.

3.2. Experimental Probes of Covalency and the Nature of the Ground State Wave Function

3.2.1. Copper L-Edge Spectroscopy

The L_3 -preedge peak of copper complexes occurs at ~ 930 eV and corresponds to a transition from the Cu 2p core level to the singly occupied HOMO of the cupric complex (Figure 14A). Because of the localized

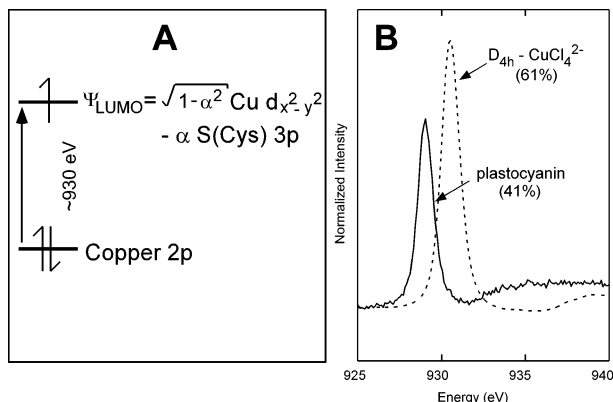


Figure 14. Cu L-edge XAS as a probe of ligand–metal covalency. (A) Energy level diagram depicting the Cu 2p to LUMO transition. (B) XAS Cu L₃-edge spectra for *D*_{4h} [CuCl₄]²⁻ and plastocyanin. Values listed are the amounts of Cu 3d character in the LUMO. Adapted from ref 91.

nature of the 2p orbital on the copper and the fact that p→d transition is electric dipole allowed, the intensity of the L-edge peak reflects the amount of Cu 3d character in the singly occupied MO hence its total covalent interaction with the ligand set.

From the data in Figure 14B, the L₃-edge intensity of plastocyanin is significantly less than that of *D*_{4h} [CuCl₄]²⁻ indicating that the blue copper site has less 3d character and thus is more covalent.⁹¹ From the data in Table 3, we know that *D*_{4h} [CuCl₄]²⁻ has 61% Cu 3d character in its singly occupied HOMO. Its intensity ratio to that of the L₃-edge of plastocyanin in Figure 14A could then be used to define the Cu 3d contribution to the blue copper ground state. This gives 41% copper 3d_{x²-y²} character in good agreement with the wave function in Figure 13.

3.2.2. Sulfur K-Edge Spectroscopy

Ligand K-edge spectroscopy is one of the most direct experimental probes of the covalent interaction of a specific ligand with a metal center. The feature at ~2470 eV corresponds to a sulfur 1s transition to the singly occupied HOMO (Figure 15A). The 1s orbital is localized on the sulfur, and s→p is electric dipole allowed; hence, the intensity of the sulfur K-edge transition reflects the sulfur 3p ligand char-

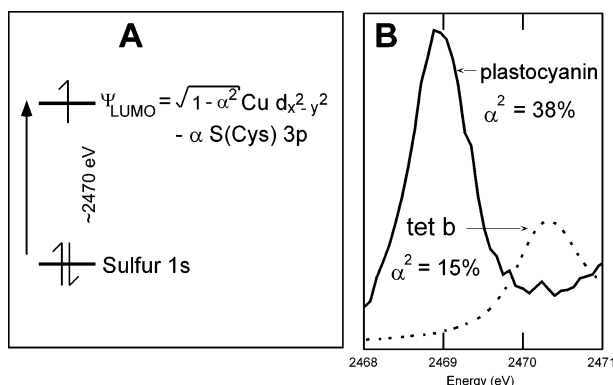


Figure 15. S K-edge XAS as a probe of ligand–metal covalency. (A) Energy level diagram depicting S 1s to LUMO transition. (B) Orientation averaged XAS S K-edge spectra for *tet b* (a model complex with a normal Cu^{II}–S(thiolate) bond) and plastocyanin. α^2 is the amount of S p character in the LUMO. Adapted from refs 85 and 92.

acter mixed into the ground state wave function due to the covalency of the Cu^{II}–S(thiolate) bond. In Figure 15B, this is ~2.5× as intense as the sulfur edge of a more normal five coordinate Cu^{II}–S(thiolate) model complex,⁹² which has ~15% sulfur character in its ground state.⁸⁵ The intensity ratio in Figure 15B then gives the thiolate 3p character in the plastocyanin active site ground state of 38%, again in good agreement with the spectroscopically adjusted X α -sw wave function in Figure 13 and directly reflecting the high covalency of the Cu^{II}–S(thiolate) bond in blue copper sites.

It should be noted that recent S K-edge XAS data⁹³ on the blue copper site in azurin indicate ~45% S 3p character (based on using a S K-preedge area of 1.02 for 38% S 3p character from Figure 15B). All azurin samples were fully oxidized and spin quantitated to determine copper loading; thus, these data most likely reflect a more accurate covalency estimate for a blue copper site.

3.2.3. LT MCD Spectroscopy

The final feature of the ground state wave function in Figure 13, the orientation of the 3d_{x²-y²} orbital in the *x,y* plane, came from the experimental assignment of the unique absorption features of the blue copper site in Figure 16A. Lowering the temperature sharpens the transitions, and by correlation to LT CD and MCD data, each involving a different selection rule (vide supra), eight transitions are required to fit the absorption spectrum (numbered in Figure 16B). The intense absorption feature at ~16 000 cm⁻¹, band 4, is the characteristic absorption feature of blue copper, and there is a second lower energy feature band 6, with moderate absorption intensity. Polarized single-crystal absorption data on plastocyanin in Figure 16C showed that both bands have the same polarization ratio that associated these with the Cu^{II}–S(Cys) bond. Hence, the assignment might follow that of CT transitions in “normal” cupric complexes described in section 2: high energy intense σ , low energy weak π CT (Figure 4G). However, LT MCD spectroscopy showed that this is, in fact, not the case. From Figure 16D vs B, bands 5–8 are intense in the LT MCD spectrum but weak in the absorption spectrum, while band 4 (and those to higher energy) is intense in absorption and weak in LT MCD. These data allow definitive assignment of these transitions.

As given in eq 4, LT MCD intensity involves a C term mechanism for paramagnetic complexes, which requires two perpendicular transition moments (M_j).

$$I \propto g_z M_x M_y + g_y M_x M_z + g_x M_y M_z \quad (4)$$

However, in low symmetry sites, all states are orbitally nondegenerate and electronic transition moments must be unidirectional (i.e., polarized in only one molecular direction). LT MCD intensity then derives from spin–orbit coupling between excited states with different polarization directions ($M_j \neq M_i$). Because the spin–orbit coupling constant of Cu^{II} (~830 cm⁻¹) is considerably larger than that of the ligands [(N,O) ~ 70 cm⁻¹, S ~ 380 cm⁻¹], the C term

Table 6. Atomic Orbital Populations and Spin Densities by Means of Mulliken (MPA) and Natural (NPA) Population Analyses for the Plastocyanin Model Complex (Hirshfeld (HIR)/Voronoi (VOR) Population Analyses for Calculations with BSIV in ADF)

	Spin Density (MPA/NPA)				
	Cu	S(Cys)	C(Cys)	H(Cys)	N(His)
BP86/BS5	28/28	59/58	-2/-1	3/3	10/11
BP86/BSIV	27/-	61/-	-2/-	3/-	9/-
B3LYP/BS5	31/32	59/57	-2/-1	3/3	10/10
BHandHLYP/BS5	50/53	41/38	-2/-1	2/2	10/10
experimental				2 ^c	8 ^d
B(38HF)P86/BS5	37/41	54/50	-3/-1	3/3	10/10
BP86(Z*)/BSIV	49/-	42/-	-1/-	2/-	8/-
β -LUMO (MPA/NPA)					
	Cu	S(Cys)	C(Cys)	H(Cys)	N(His)
BP86/BS5	32/30	54/55	1/1	3/3	8/10
BP86/BSIV	30/-	56/-	2/-	2/-	7/-
(HIR/VOR)	33/32	49/51	4/1	3/6	6/7
B3LYP/BS5	35/34	53/54	1/0	2/2	7/8
BHandHLYP/BS5	53/55	36/35	1/0	2/1	6/6
experimental	41 ^a	45 ^b			
B(38HF)P86/BS5	42/41	47/49	1/0	2/2	6/7
BP86(Z*)/BSIV	49/-	38/-	1/-	2/-	7/-
(HIR/VOR)	51/51	34/35	3/1	2/4	6/6

^a Cu 3d character by Cu L-edge XAS for plastocyanin + 1% Cu 4s/4p contribution. ^b S 3p character by S K-edge XAS for azurin + 1% S 3s contribution. ^c Paramagnetic NMR + 1% contribution from C(Cys). ^d ¹⁴N ENDOR + 1% from other ring atoms.

scription. This is most appropriate for comparison with the S K-edge and Cu L-edge experimental results. The total atomic spin density, which is the excess electron density due to the unoccupied antibonding combination, is also used to characterize the bonding and for comparison to experimental superhyperfine parameters and paramagnetic NMR results. For the plastocyanin model complex, the hole covalency and the spin density are similar with some differences [at most 7% by MPA and 3% in natural population analysis (NPA)^{95–97}]. The atomic spin densities reflect additional contributions such as Cu 4s and 4p from higher, unoccupied orbitals and a S 3s contribution from deeper, occupied orbitals. The orbital population of the β -LUMO reflects contribution from a single orbital, which is dominantly involved in the ground state bonding.

In general, the total spin density of the β -methylene H-atoms and the imidazole (δ -histidine) N-atoms remains within 2% of the experimental values. Interestingly, the functional dependence is only reflected in the distribution of the orbital characters between the Cu and the S(Cys) atoms. In agreement with single-crystal EPR experiments,⁷⁸ the axial thioether ligand does not contribute to the ground state bonding.

As seen for the $[\text{CuCl}_4]^{2-}$ in section 2.2, the GGA density functional (BP86 in Table 6) overestimates the covalency with too much S(Cys) character in the ground state wave function (54–61 vs 38% in experiment). The hybrid B3LYP functional (with 20% HF exchange) improves the bonding; however, it is still too covalent (53–59%) and the BHandHLYP functional (with 50% HF exchange) gives too much metal

character (50–55 vs 41% in experiment), which corresponds to too ionic bonding. The spectroscopically adjusted (to $[\text{CuCl}_4]^{2-}$, see section 2.2) density functional B(38HF)P86 gives a reasonable description of the ground state (47–54%). As an alternative approach in programs without hybrid functionals, calculations with adjusted effective nuclear charge [BP86(Z*)] also give a reasonable bonding description. Using the reduced effective nuclear charge (Z_{eff}) of 28.55 optimized for $[\text{CuCl}_4]^{2-}$, the bonding is somewhat too ionic (49–51% Cu character vs 41% in experiment).

It is worth noting the method dependence of the spin densities and hole populations, which is about 4 and 2%, respectively. In Table 6, the results of independent population analyses are compared. In general, the NPA tends to give more reasonable results than the MPA due to the latter's separation of the electron density equally between atoms. The atoms in molecule (AIM),⁹⁸ which is considered as one of the most accurate approaches for dividing electron density between atoms, could not be used here due to the highly complex nature of the electron density of the plastocyanin model complex.

In addition to the ground state wave function properties, the excited state calculated energies are also evaluated relative to experiment (Figure 17). As discussed in section 3.2.3 and Figure 16, the experimental electronic absorption spectrum of plastocyanin can be well-separated into LF (or d-d) and metal to ligand CT excitations at lower and higher energies, respectively. The signs of the MCD bands combined with a connection⁹⁴ of g_z with the energy of band 7 in Figure 16B lead to the specific assignments of the LF transitions as shown in Figure 16B and reproduced in column 1, Figure 17. The LF transitions are at lowest energy with $d_{x^2-y^2}$ (ground state) < d_z^2 < d_{xy} < d_{xz+yz} < d_{xz-yz} . The first two CT transitions have been assigned to be the Cys π and Cys pseudo- $\sigma \rightarrow \text{Cu}^{\text{II}} 3d_{x^2-y^2}$ excitations, which are split by about 2000 cm^{-1} , followed by the His $\pi \rightarrow \text{Cu}^{\text{II}} 3d_{x^2-y^2}$ excitations at higher energies.

In general, CASPT2 calculations⁹⁹ (column 8, Figure 17) on a simplified model complex [(imidazole)-Cu(SH)(SH₂)]¹⁺ employing a moderate-sized basis set and density functional calculations with Slater type basis sets (columns 2, 4, and 5, Figure 17) reproduce the grouping of LF and CT transitions. In contrast, the time-dependent DFT calculations^{100–102} employing Gaussian type basis sets (columns 6 and 7, Figure 17) do not. The TDDFT assignments are based on the mixing coefficients of ground state orbitals contributing to the transitions. The questionable quality of the TDDFT excitations for the blue Cu system reflects an unreasonable orbital description of the occupied (donor) orbitals as well as the limited applicability of the TDDFT formalism for open shell systems. The nonadjusted GGA functional (BP86/BSIV, in column 3, Figure 17) gives an overly covalent bonding description results in too low CT and too high LF excitation energies relative to experiment.

In the adjusted $X\alpha$ -sw calculations⁸⁹ (column 2, Figure 17), the LF and CT transitions are well-separated in agreement with experiment. Because of

involved in bonding, model complexes rather than the proteins are studied, and because one goal here is to understand normal ligand–metal bonding and its relation to the blue copper site, the models chosen are the blue copper relevant imidazole, dimethyl sulfide, and methylthiolate ligands bound to coordinatively unsaturated Cu^1 sites on oxide and chloride single-crystal surfaces in ultrahigh vacuum.⁷ As an example, the photoelectron spectral data for methylthiolate bound to cuprous oxide are shown in Figure 18A (where the surface oxide is used to deprotonate

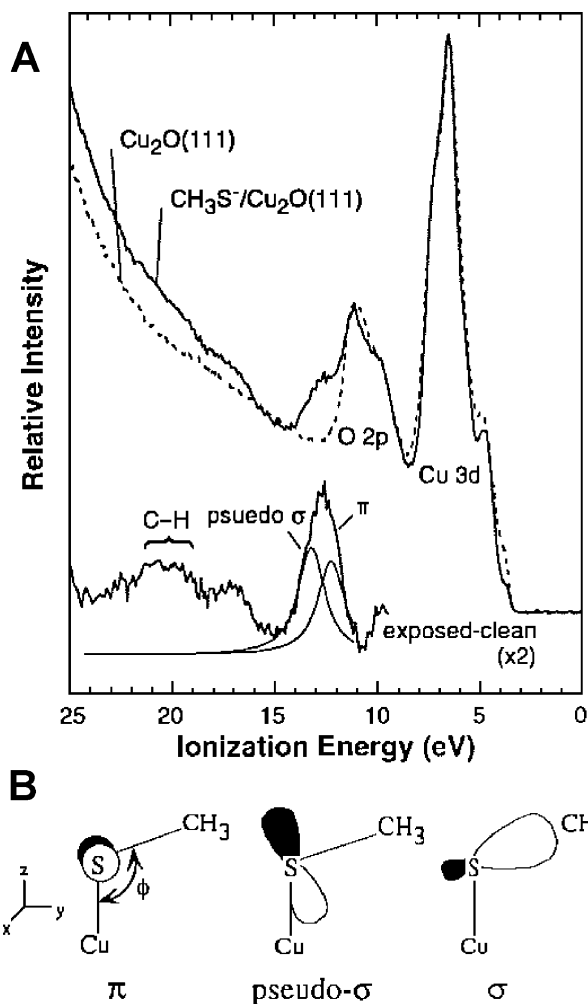


Figure 18. Cu^1 – SCH_3 bonding. (A) Valence band PES of $\text{Cu}_2\text{O}(111)$ (dotted line), $\text{Cu}_2\text{O}(111)$ exposed to methanethiol (solid line), and their difference spectrum (bottom) with Gaussian/Lorentzian resolution of the low-energy region; (B) valence orbitals of methanethiolate. Adapted from ref 7.

methylthiol). The dashed spectrum gives the valence band region of clean Cu_2O , and the solid spectrum is that of methylthiolate bound to the surface. The difference spectrum at the bottom of Figure 18A gives the valence orbitals of the Cu^1 – S (thiolate) bond. Varying the photon energy changes the intensity of the peaks^{12,104} and allows the specific assignments of the levels indicated in the difference spectrum. Three valence orbitals of thiolate are involved in bonding to the Cu^1 : the π , pseudo σ , and σ shown in Figure 18B. The π and pseudo σ , which are the S 3p orbitals perpendicular to the S–C bond, dominate the

bonding and split in energy as the angle ϕ in Figure 18B deviates from 180° . Thus, the energy splitting and intensity changes with photon energy of the peaks in the difference spectrum in Figure 18A give the geometric and electronic structure of the unconstrained Cu^1 – S (thiolate) bond of the surface complex. Our strategy was to use VEPES to experimentally define the geometric and electronic structure of each normal Cu^1 –ligand bond for the surface complexes. These data were then used to evaluate and calibrate $\text{X}\alpha$ -sw electronic structure calculations of the unconstrained surface complexes. These experimentally calibrated $\text{X}\alpha$ -sw calculations were then used to generate an electronic structure description of the reduced blue copper site and to evaluate the change in electronic structure with oxidation.

These studies, which are described in detail in ref 7, demonstrate that the bonding in the reduced blue copper site is dominated by ligand p to Cu^1 4p σ donor interactions. Thus, even though the bonding involves a reduced copper center, which results in the 3d orbitals being higher in energy by 1–2 eV due to the lower effective nuclear charge on the reduced copper relative to the oxidized site (see Figure 19), there is no evidence for back bonding for any of the blue

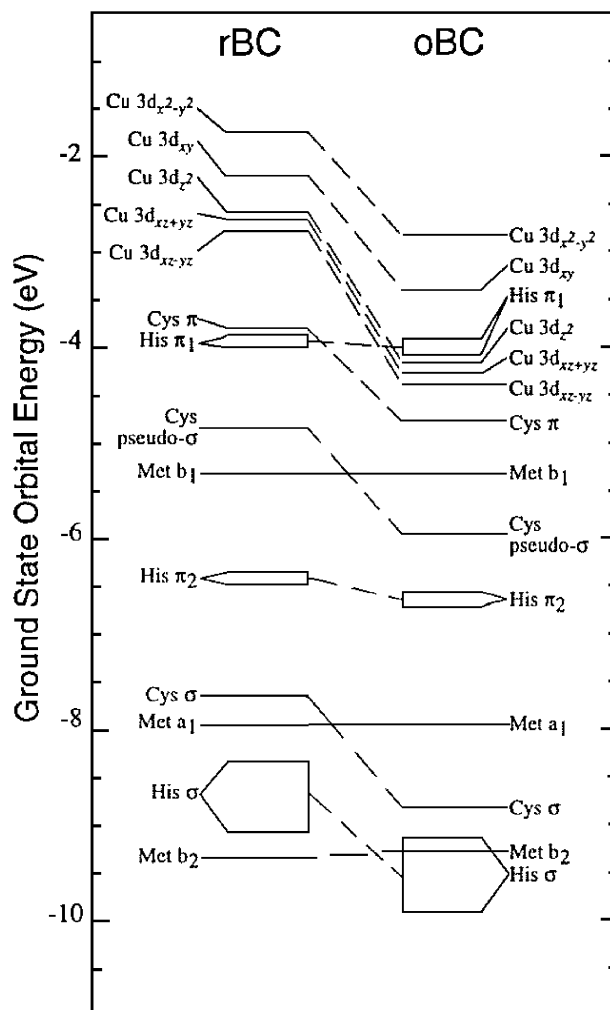


Figure 19. Valence molecular levels from $\text{X}\alpha$ -sw calculations of reduced blue copper (rBC) and oxidized blue copper (oBC). Orbital energies of oxidized blue copper have been aligned to the Met a_1 level of reduced blue copper.¹⁸⁸ Adapted from ref 7.

copper ligands. We further found that the long Cu^I–S(Met) bond length of 2.9 Å does not derive from the electronic structure of the reduced blue copper site but is imposed on the site by the protein structure. Both calculations and a statistical analysis of the known structures in the Cambridge Crystallographic Database (CCDB) indicate that a reasonable Cu^I–S(Met) bond length is ~2.32 Å.⁸ As considered in the next section, this appears to be an important feature of the blue copper site structure that can be ascribed to the protein matrix (i.e., an entatic or rack state). This elongated thioether Cu^I–S(Met) bond reduces the donor interaction of this ligand with the copper. This is compensated for by the thiolate, leading to the short, strong Cu^I–S(Cys) bond (Figure 20).⁷

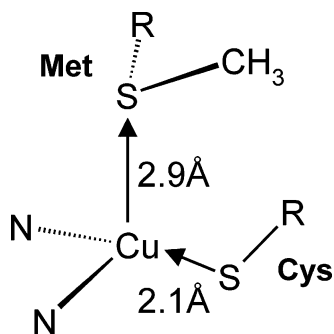


Figure 20. Effects of the protein on the ligand donor interactions in blue copper sites. Arrows show decreased electron donation from the axial S(Met), which results in increased electron donation from the S(Cys). Adapted from ref 8.

Comparison of the electronic structure descriptions of the oxidized and reduced blue copper sites indicates that the ligand donor interactions with the unoccupied copper 4p (and 4s) levels change little upon oxidation and that the dominant change in bonding involves the hole produced in the 3d_{x²–y²}-derived HOMO in Figure 13. Thus, on oxidation, the blue copper site loses a strong antibonding interaction with the S(thiolate) and weaker antibonding interactions with the two imidazole nitrogens.

Having obtained an experimentally calibrated electronic structure description of the reduced site, we could evaluate the changes in geometric structure, which would occur for a blue copper site unconstrained by the protein. This involved evaluation of the electron–nuclear linear coupling terms of the oxidized site in the reduced geometry along all of the normal modes, Q_i , of the blue copper site. As illustrated in Figure 21, a nonzero slope of the linear coupling term of the oxidized site in the reduced geometry (Γ_{ex}), $Q_i \langle \Gamma_{\text{ex}} | (\delta V / \delta Q_i)_0 | \Gamma_{\text{ex}} \rangle$, corresponds to a distorting force along normal mode Q_i .¹² The significant distorting forces that we find to be present (Table 7) are consistent with the change in electronic structure on oxidation described above. There is a large distorting force toward contraction of the Cu–S(thiolate) bond (along a_1 stretching modes). This, however, is opposed by a large force constant, k_i , associated with the short and strong Cu–S(thiolate) bond leading to a limited contraction ($\Delta Q_i = \langle \Gamma_{\text{ex}} | (\delta V / \delta Q_i)_0 | \Gamma_{\text{ex}} \rangle / k_i$) along this bond (Table 7 next to

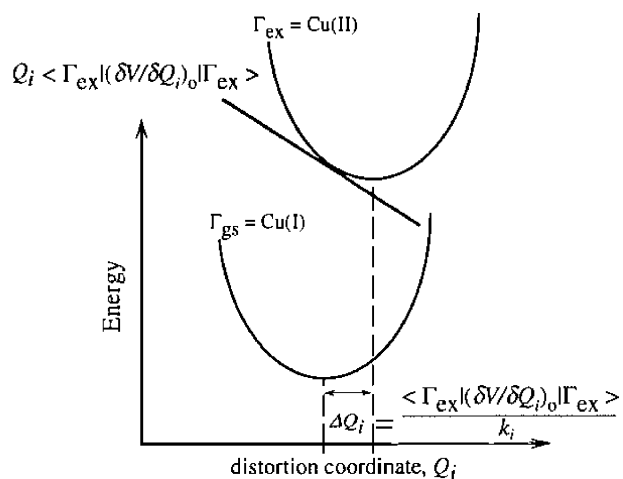
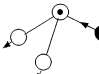
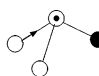

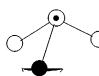

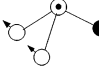


Figure 21. Configuration coordinate diagram of the linear coupling term for the distorting force along the i -th normal mode of vibration on the oxidized blue copper site relative to the reduced ground state. Adapted from ref 7.

Table 7. Distorting Forces along Normal Modes of the [CuN₂S] Model

normal modes	$\delta V / \delta Q_i$	E_V^c	μ_i	k_i	ΔQ_i	ΔR (Å)	
stretches ^a	(eV/Å)	(cm ⁻¹)	(amu)	(md/Å)	(Å)	Δ Cu-S	Δ Cu-N
 1a'	4.35	400	94	8.72	0.080	-0.069	+0.035
 2a''	0.17	275	80	4.00	0.007	0.000	±0.006
 3a'	3.28	220	82	2.58	0.204	-0.071	-0.141
normal modes	$\delta V / \delta Q_i$	E_V^c	μ_i	k_i	ΔQ_i	ΔR ^b	
bends ^a	(10 ⁻³ eV/°)	(cm ⁻¹)	(amu)	(md/Å)	(°)	Δ SCuN	Δ NCuN
 4a''	0.60	70	79	.23	0.1°	±0.1	0.0
 5a'	0.49	60	103	.23	0.1°	0.0	-0.1
 6a'	4.45	40	102	.08	1.5°	+1.1	+0.8

○ Cu ○ His ● Cys

the last column, top). There are also smaller distorting forces to contract along the Cu–N(His) bonds (Table 7, last column). Importantly, no significant distorting force is present along any of the bending modes (Table 7 bottom, last two columns). In section 4.2, XAS combined with crystallography is used to define the geometric changes of the reduced blue copper site on oxidation. Consistent with the above linear coupling terms, the dominant structural changes are limited contractions along the Cu–S(Cys) and Cu–N(His) bonds, and there is no significant angle change with oxidation.

An entatic or rack state where the Cu^{I} geometry is imposed on the Cu^{II} site by the protein would correspond to a large Jahn–Teller distorting force along a bending mode, which would give a tetragonal distortion of the Cu^{II} site. The lack of a Jahn–Teller distorting force in the oxidized blue copper site can be understood from the scheme in Figure 22. In an

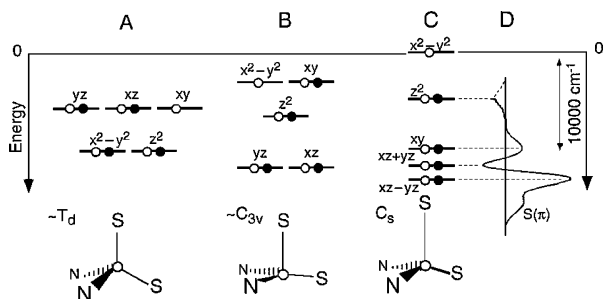


Figure 22. Schematic of the blue copper LF effect on the oxidized site. The Jahn–Teller distorting force is eliminated, which minimizes the reorganization energy of the site. (A) Energy level diagram of an idealized T_d structure and (B) a C_{3v} structure, which are both subject to Jahn–Teller distortions upon oxidation, while the (C) C_s structure in the blue site is not. (D) MCD spectrum of plastocyanin, showing the $d_{x^2-y^2}$ and d_{xy} orbitals are split by over $10\,000 \text{ cm}^{-1}$, eliminating the Jahn–Teller distorting force of the oxidized site. Adapted from ref 8.

idealized tetrahedral structure, there would be a 2T_2 ground state, which is orbitally degenerate (A). Electron–nuclear coupling over the orbitally degenerate levels leads to the Jahn–Teller distortion. In the reduced blue copper site, there is an elongated Cu–S(thioether) bond, which produces C_{3v} effective symmetry at the copper leading to a 2E ground state in the oxidized site, which corresponds to the unpaired electron being in the degenerate ($3d_{x^2-y^2}$, $3d_{xy}$) set of orbitals (B). The long Cu–S(thioether) bond further results in contraction of the Cu–S(thiolate) bond (see above and Figure 20), which splits the remaining orbital degeneracy of the 2E (C). In particular, from the MCD assignment in Figure 16B reproduced in Figure 22D, the $3d_{xy}$ level is $>10\,000 \text{ cm}^{-1}$ above the $3d_{x^2-y^2}$ ground state; it is a linear coupling term between these levels that would lead to a Jahn–Teller distorting force. Thus, the orbital degeneracy is strongly lifted in the C_s site symmetry (C) and there is no Jahn–Teller distorting force. This leads to little geometric change on oxidation and a low Franck–Condon barrier to ET (see section 7).

4.2. X-ray Absorption Spectroscopy (XAS)

In addition to PES, XAS may also be used to probe a d^{10} metal configuration. XAS spectroscopy involves the photoexcitation of core electrons to partially occupied or unoccupied valence orbitals on the metal ion and to the continuum. In the case of a metal K-edge, a metal $1s$ core electron is excited resulting in an intense electric dipole-allowed $s \rightarrow p$ transition, which can provide information about oxidation state and site geometry. Once the electron has been excited in to the continuum, it interacts with neighboring atoms; the scattering producing EXAFS, which provides structural information.

A systematic study of a series of Cu^{I} complexes with varying coordination numbers has shown that the Cu $1s \rightarrow 4p$ preedge peak energies and intensities can be correlated with the coordination number and understood in the context of a simple electronic structural description.¹⁰⁵ Figure 23A shows a com-

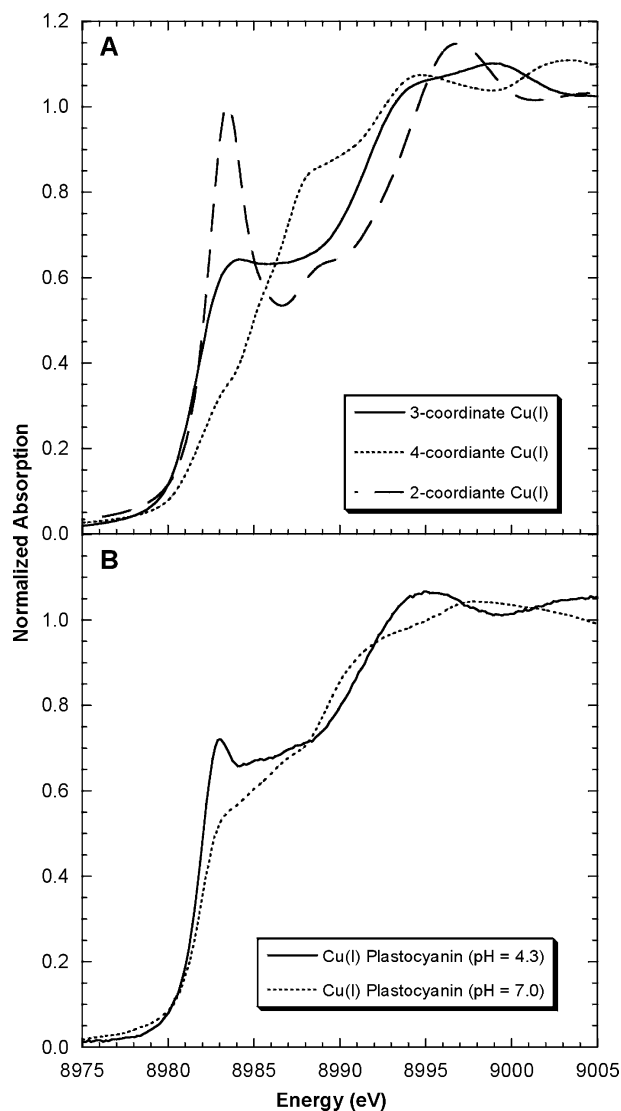


Figure 23. (A) Comparison of the normalized Cu K-edge XAS spectra of representative two-, tri-, and four-coordinate Cu^{I} model complexes. (B) Normalized Cu K-edge XAS spectra of low (pH = 4.3) and high (pH = 7.0) pH Cu^{I} plastocyanin. Adapted from ref 105.

parison of “typical” two-, three-, and four-coordinate Cu^{I} model complexes, demonstrating that as the coordination number increases the preedge feature splits in energy, decreases in intensity, and increases in energy. This can be understood based on a simple LF model shown in Figure 24. The 3-fold degeneracy of the $4p_{x,y,z}$ orbitals in a free Cu^{I} ion will be split in energy by a LF. For a linear two-coordinate Cu^{I} complex, this would involve a repulsive interaction along the z -axis, which would raise the energy of the antibonding copper $4p_z$ MO relative to the $4p_{x,y}$ levels. In addition, ligand overlap along the z -axis will reduce the Cu $4p_z$ character in the antibonding orbital, thus reducing the Cu $1s$ to $4p_z$ transition intensity. Hence, an intense preedge feature due to

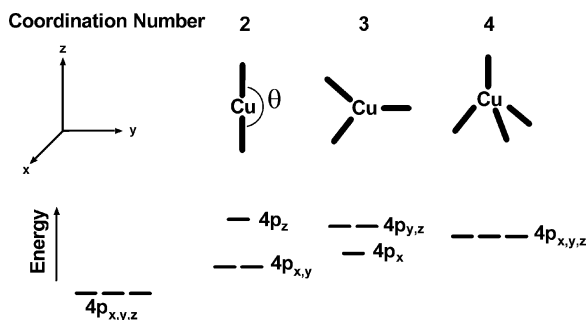


Figure 24. LF splitting of reduced Cu 4p orbitals as a function of site geometry. Adapted from ref 105.

the transition to the doubly degenerate $4p_{x,y}$ orbitals appears at lower energy and with much greater intensity than the $1s \rightarrow 4p_z$ transition. Bringing in a third ligand along the y -axis and decreasing the θ from 180° splits the degeneracy of the $4p_{x,y}$ orbitals, with the p_y orbital moving to higher energy and the transition decreasing in intensity due to covalent mixing with the added ligand. For a four-coordinate tetrahedral complex, the $4p_{x,y,z}$ orbitals should be degenerate, however shifted to higher energy and reduced in intensity due to covalent mixing of all 4p orbitals with the four ligands.

The sensitivity of the Cu^{I} -edge to the coordination environment has been used to probe the environment of blue copper proteins. Figure 23B shows the data for reduced plastocyanin at high (pH = 7.0) and low (pH = 4.3) pH values.¹⁰⁶ At high pH, the edge intensity and position are clearly closer to that of a three-coordinate complex than a four-coordinate complex, consistent with the weak axial methionine in plastocyanin. As the pH of plastocyanin is decreased, the His87 becomes protonated off the Cu^{I} center (and the Met92 moves in to a distance of 2.5 Å).¹⁰⁷ The

edge data reflect this change showing an increase in the energy and intensity at ~ 8989 eV, indicating that the average Cu^{I} coordination environment decreases from three-coordinate to closer to two-coordinate.

EXAFS data and crystallographic results also have provided important information about the reduced site of blue copper proteins. Table 8 summarizes the changes in geometric parameters for the oxidized and reduced blue copper sites found in azurin and plastocyanin.^{71,107–112} From crystallographic results, upon reduction, the average Cu–N(His) and Cu–S(Cys) bond lengths increase by ~ 0.12 and ~ 0.06 Å, respectively and the changes in bond angles are minimal (consistent with discussion in section 4.1). The reported crystal structures range from 1.33 to 1.9 Å in resolution. However, even at 1.3 Å resolution, the error in the bond lengths is ~ 0.05 – 0.08 Å.^{71,113} EXAFS results, while providing only very limited angular information, provide a greater accuracy in bond length determination (~ 0.02 Å) and hence when coupled with crystallographic results provide a more accurate assessment of the changes that occur upon oxidation. The results of EXAFS studies on plastocyanin and azurin are summarized in Table 9.^{114–119} The results indicate that upon oxidation the Cu–N and Cu–S bond lengths decrease by an average of ~ 0.06 and ~ 0.08 Å, respectively. Early EXAFS studies on plastocyanin showed evidence for a long Cu–S(Met) in the oxidized and reduced forms of poplar plastocyanin and in the oxidized forms of *P. vulgris* plastocyanin and *S. oleracea* plastocyanin.^{86,114–117} However, these studies did not include multiple scattering interactions from the histidine ring structure, which would occur at approximately the same distance. More recent EXAFS analyses of *P. aeruginosa* azurin, which included multiple scattering contributions from the histidine rings, showed

Table 8. Summary of Published Crystallographic Data for Oxidized and Reduced Plastocyanins and Azurins

oxidation state	<i>D. Crassirhizoma</i> plastocyanin		<i>Poplar</i> plastocyanin			<i>Synechococcus</i> sp. plastocyanin		<i>A. denitrificans</i> azurin		<i>A. xylosoxidans</i> azurin	
	ox	red	ox	red	red	ox	red	ox	red	ox	red
pH	4.5	4.5	6.0	7.0	3.8	5.0	5.0			6.0	6.0
PDB code/ ref	1KDJ/ 108	1KDI/ 108	1PLC/ 71	5PCY/ 107	6PCY/ 107	1BXU/ 109	1BXV/ 109	2AZA/ 110	b/ 111	1DYZ/ 112	1DZO/ 112
resolution	1.7	1.8	1.33 ^a	1.8	1.9	1.9	1.8	1.8	1.9	1.75	1.75
	bond lengths (Å) (Pc/Az)										
Cu–N(His37/46)	1.99	1.95	1.91	2.12	2.11	1.97	2.09	2.08	2.13	2.04	2.03
Cu–N(His87/117)	2.06	2.10	2.06	2.39	3.15	2.01	2.37	2.00	2.05	1.99	2.02
Cu–S(Cys84/112)	2.23	2.21	2.07	2.16	2.13	2.14	2.17	2.15	2.26	2.14	2.16
Cu–S(Met92/121)	2.94	2.91	2.82	2.87	2.52	2.93	2.80	3.11	3.23	3.26	3.26
Cu–O(Gly45)								3.13	3.22	2.72	2.75
	bond angles (deg)										
N(His37/46)–Cu– N(His87/117)	106	105	97	99	89	101	93	105	104	106	107
N(His37/46)–Cu– S(Cys84/112)	128	130	132	136	141	131	140	135	132	133	133
N(His37/46)–Cu– S(Met92/121)	81	81	89	88	95	86	92	77	78	74	74
N(His87/117)–Cu– S(Cys84/112)	119	117	121	110	87	121	109	119	123	121	120
N(His87/117)–Cu– S(Met92/121)	108	108	101	106	106	99	100	96	92	88	89
S(Cys84/112)–Cu– S(Met92/121)	107	108	110	113	124	108	115	107	109	105	105

^a Coordinates given in Figure 9A are from the original lower resolution (1.6 Å) structure. ^b Not presently listed in the PDB.

Table 9. Summary of Published EXAFS Data for Oxidized and Reduced Plastocyanins and Azurins

oxidation state	<i>Poplar plastocyanin</i>		<i>P. vulgaris plastocyanin</i>		<i>S. oleracea plastocyanin</i>		<i>P. aeruginosa azurin</i>	
	ox	red	ox	red	ox	red	ox	red
pH	6.0	7.0			5.5	5.5	5.5	5.5
refs	86, 114	114	115, 116	115, 116	117	117	119	118
2 Cu–N(His)	1.98	1.96/2.01	1.97	2.05	1.94/2.02	1.96/2.11	1.95	2.00
1 Cu–S(Cys)	2.08	2.19	2.11	2.22	2.09	2.15	2.14	2.21
1 Cu–S(Met)	2.76	2.86	2.66		2.90			

no evidence for the distant Cu–S(Met) bond, consistent with a long, weakly coupled interaction.^{118,119}

Crystallographic and EXAFS results indicate that only small changes in bond length and angle occur upon oxidation of blue copper sites. These changes are summarized in Figure 25, which shows the

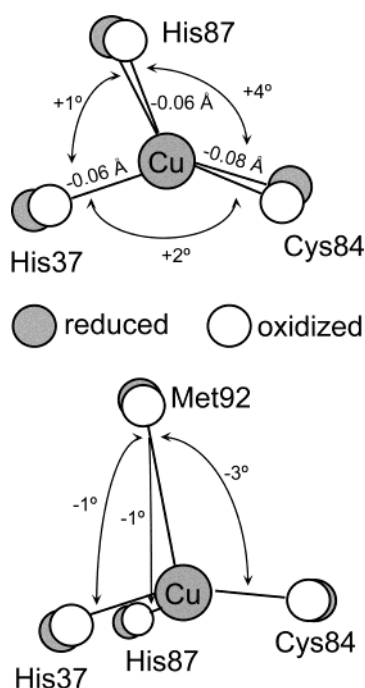


Figure 25. Average structural changes upon oxidation of a blue copper site (amino acid numbering from plastocyanin). Bond lengths are based on EXAFS results, which do not distinguish His37 and His87. Angular changes are based on crystallographic results. Adapted from ref 3.

average bond length change from EXAFS and the average angular change from crystallography. The limited structural change at the Cu site helps lower the reorganization energy and makes an important contribution to the ET function of these sites, which is discussed further in section 7. Note that the largest bond length change is the Cu–S(Cys), which also has the largest vibrational frequency (Table 7) and therefore involves the most energy.

5. Blue Copper Geometric and Electronic Structure: Role of the Protein

The VEPES studies described in section 4.1 indicate that the long Cu^I–S(thioether) bond in plastocyanin is imposed on the reduced site by the protein matrix. This long bond reduces the donor interaction of the thioether with the copper and is compensated by the thiolate resulting in the short, strong Cu–S(thiolate) bond (Figure 20). Together, these

eliminate the Jahn–Teller tetragonal distortion of the Cu^{II} site upon oxidation. Relative to the “classic” blue copper site in plastocyanin, there are a number of naturally occurring and mutant blue copper sites, which exhibit perturbed geometric and electronic structures. The perturbed spectral features (relative to plastocyanin) include increased absorption intensity at 450 nm at the expense of the 600 nm absorption band and more rhombic EPR spectra. Structurally, the perturbed sites divide into two categories: (i) those having the same ligand set as plastocyanin [S(Cys), 2 N(His), and S(Met)] but with geometric distortions (section 5.1) and (ii) those having variation in the chemical nature of the axial ligation (section 5.2). These perturbed blue copper sites provide the opportunity to experimentally evaluate the role of the protein in determining the geometric and electronic structure of the site (sections 5.1 and 5.2) and to evaluate electronic structure calculations of geometry optimized structures (section 5.3).

5.1. Standard Ligand Set [S(Cys), 2 N(His), and S(Met)]: The Coupled Distortion

Proteins such as cucumber basic blue (also called plantacyanin) and *Achromobacter cycloclastes* nitrite reductase (NiR) have the same ligand set as plastocyanin [i.e., axial S(Met)] yet exhibit perturbed spectral features (in fact, NiR is a green protein solution). These spectral features are compared to those of plastocyanin (assigned in section 3) in Figure 26.^{89,120} From Figure 26A, in going from plastocyanin → cucumber basic blue → nitrite reductase, the S(Cys) $\pi \rightarrow \text{Cu } 3d_{x^2-y^2}$ CT intensity decreases while the S(Cys) $\sigma \rightarrow \text{Cu } 3d_{x^2-y^2}$ CT intensity increases. Because CT intensity reflects orbital overlap (vide supra), these absorption spectral changes indicate that the singly occupied $3d_{x^2-y^2}$ acceptor orbital is rotated from a π to a σ interaction with the S(thiolate) ligand. This is also supported by DFT calculations^{89,99} in Figure 26B. From the LT MCD spectra in Figure 26C (assigned as in section 3), we observed that this dramatic spectral change is associated with a shift in the LF transitions to higher energy corresponding to a tetragonal distortion of the LF of the blue copper site in going to nitrite reductase. Finally, from Figure 26D, associated with this change from π to σ Cu–S(thiolate) bonding and tetragonal distortion of the site, the Cu–S(Cys) effective stretching vibrational frequency decreases (weighted average $\langle \nu_{\text{Cu-S(thiolate)}} \rangle = 403$ to 394 to 383 cm^{-1} for spinach plastocyanin, cucumber basic blue, and nitrite reductase, respectively^{121–123}) indicating a significant weakening of the Cu^{II}–S(thiolate) bond in the NiR site.

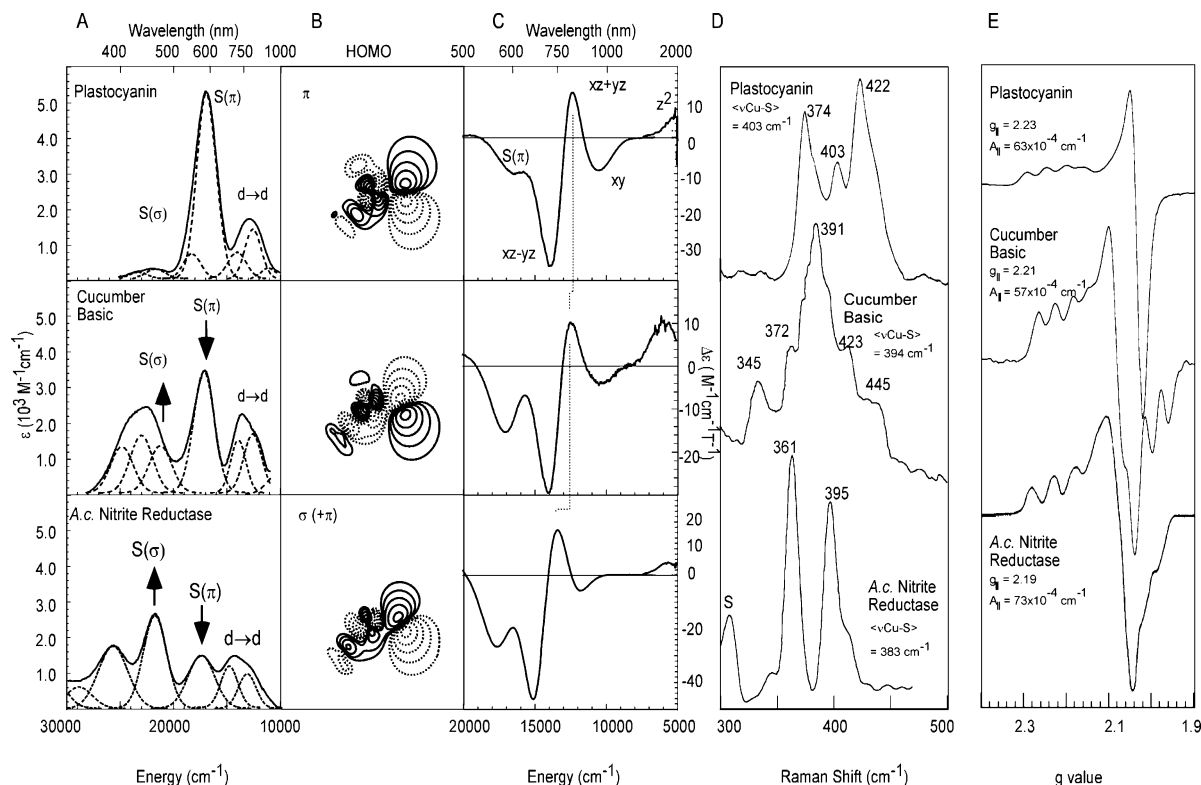


Figure 26. Coupled distortion in a series of perturbed blue Cu proteins. (A) Low-temperature absorption showing redistribution of spectral intensity in Cys π and σ CT bands. (B) Redox active orbitals calculated with χ -sw showing rotation from a π type interaction in plastocyanin to σ ($+\pi$) mixture in nitrite reductase. (C) MCD spectra showing a shift of the LF transitions to higher energy indicating a tetragonal distortion. (D) Resonance Raman spectra indicating weakening of the Cu–S(thiolate) bond along the series. (E) EPR spectra showing a small change along the series. Adapted from ref 155.

Before correlating to crystal structures, two spectroscopic points should be clarified. First, the fact that the LF transitions (easily observed in the LT MCD spectra in Figure 26C from their high C_0/D_0 ratios) shift up in energy, clearly demonstrates that the site becomes tetragonal rather than tetrahedral (as proposed in refs 124 and 125) in going from plastocyanin to NiR. An increasing tetrahedral distortion would shift the LF transitions to lower energy (see also section 5.2). Second, from Figure 26E, the EPR data (including ESEEM and ENDOR, not shown) exhibit small changes along the series ($g_z = 2.23, 2.21, 2.19$; $g_y = 2.06, 2.07, 2.06$; $g_x = 2.05, 2.02, 2.02$ for plastocyanin, cucumber basic protein, and NiR, respectively); yet, there is a large change in electronic structure [e.g., π to σ Cu^{II}–S(thiolate) bonding]. This insensitivity of the spin Hamiltonian parameters to this change in electronic structure is considered in section 5.1.1.

These spectroscopic/electronic structural trends can be correlated to the crystallographic results on these sites as summarized in Figure 27.^{71,126,127} On going from plastocyanin to cucumber basic blue to nitrite reductase, the Cu–S(thioether) bond decreases by 0.3 Å and the Cu–S(thiolate) bond increases by >0.1 Å. Furthermore, the Cu–S(Cys)–S(Met) plane rotates relative to the N(His)–Cu–N(His) plane in a Jahn–Teller type (e_u) distortion toward a more tetragonal geometry. This electronic/geometric correlation has been termed the coupled distortion¹²⁰ in which the strong axial Cu–S(Met) interaction produces a weaker Cu–S(Cys) bond and together result in a tetragonal

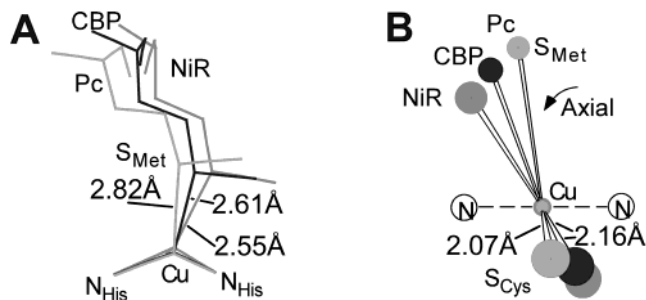


Figure 27. Continuum of coupled tetragonal distortions in a series of perturbed blue copper proteins. Crystal structures show contraction of the Cu–S(Met) bond associated with elongation of the Cu–S(Cys) bond and tetragonal e_u -like mode Jahn–Teller distortion. Adapted from ref 8.

Jahn–Teller distortion of the site. These perturbed blue copper sites with the same ligand set as plastocyanin demonstrate that the protein matrix does indeed contribute to the geometry of the active site through stabilization of sites with the standard ligand set [S(Cys), 2 N(His), and S(Met)] at different positions along this coupled distortion coordinate. The idea that the stronger axial Cu–S(Met) bond in NiR is an important factor in leading to the large distortion toward tetragonal in the coupled distortion coordinate is demonstrated by the mutant studies involving this axial ligand described in section 5.1.1.

Finally, it should be emphasized that the spectra and structures in Figures 26 and 27 reflect a continuum of geometries and electronic structures. This differs from proposals based on DFT calculations (see

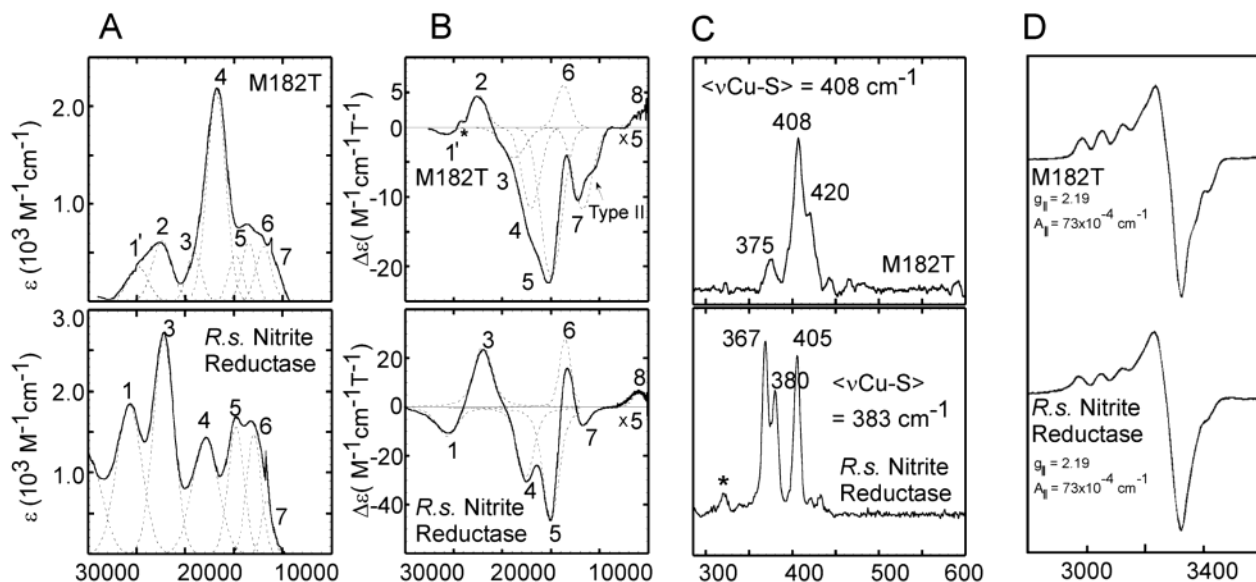


Figure 28. Comparison of spectral features of Met182Thr mutant and wild-type nitrite reductase. (A) Low-temperature absorption, (B) MCD spectra, (C) resonance Raman at excitation energy of 647 (top) and 458 nm (bottom), and (D) EPR spectra. Adapted from ref 128.

section 5.3), which have suggested that the experimentally observed spectral changes arise from an equilibrium mixture of trigonally distorted tetrahedral (as in plastocyanin) and tetragonal limiting structures.⁹⁹ The presence in the 5K spectra of a single set of MCD d→d bands, Figure 26C, and a single set of EPR spectra, Figure 26E, across the series makes it clear that this is a continuum of individual geometries along the coupled distortion coordinate.

5.1.1. Green to Blue Copper Sites: The M182T Mutant of Nitrite Reductase

To gain further insight into the role of the axial ligand, studies¹²⁸ have also been pursued on the green copper site in *Rhodobacter sphaeroides* nitrite reductase (R.s. NiR) and its Met182Thr mutant.^{129,130} Wild-type R.s. NiR exhibits spectroscopic signatures characteristic of a green site (i.e., a highly perturbed blue site as discussed in section 5.1), while the M182T mutant shows spectroscopic features characteristic of a classic blue site (i.e., in plastocyanin).

Figure 28A shows a comparison of the absorption spectrum for M182T R.s. NiR and the wild-type enzyme. The M182T mutant shows an increase in the absorption intensity at ~600 nm and an accompanying decrease in intensity at ~450 nm (making it blue). Thus, this mutant allowed evaluation of a “blue” site in the “green” protein environment. This leads to an interesting spectroscopic series: blue – plastocyanin → green – nitrite reductase → blue – the M182T axial mutant of nitrite reductase.

The absorption intensity pattern in the mutant indicates an increase in the π Cu^{II}–S(Cys) interaction and a decrease in the pseudo σ Cu^{II}–S(Cys) interaction. This suggests that the Cu 3d_{x²-y²} HOMO orbital orientation in the mutant is similar to that of the typical blue sites such as plastocyanin. Resonance Raman data (Figure 28C) provide direct evidence that the Cu–S(Cys) bond is stronger in the Met182Thr mutant [$\langle\nu(\text{Cu-S})\rangle = 408 \text{ cm}^{-1}$] relative to the wild-

type [$\langle\nu(\text{Cu-S})\rangle = 383 \text{ cm}^{-1}$]. Thus, on going from the wild-type green site to the blue M182T mutant, the axial ligand strength decreases, the Cu–thiolate interaction strengthens, and the ground state goes from a σ to a π Cu–S(Cys) bonding interaction. From a comparison of the LF transition energies of the Met182Thr mutant to other blue copper centers (plastocyanin and fungal laccase,⁹⁴ vide infra), there is a very weak axial interaction (protein ligand or water) in the mutant.

Interestingly, this diminished axial interaction in the mutant relative to the wild-type does not change some of the ground state EPR and other spectral properties of the mutant.^{129,130} The MCD spectra (Figure 28B) indicate that the LF transition energies (bands 5–8) have remained unchanged in the mutant as compared to those in the wild-type. This results from two competing effects: (i) the coupled distortion in reverse—the loss of the strong axial thioether results in an increase in equatorial Cu–S(thiolate) interaction, which causes a more tetrahedral distortion of the site and would decrease the LF energies—and (ii) the presence of the very weak axial ligand (weaker than plastocyanin, but not completely absent as in the three-coordinate site of fungal laccase, vide infra), which allows the Cu to move into the CuN₂S plane resulting in a more trigonal structure, which would increase the LF transition energies (see section 5.2.1). EPR measurements (Figure 28D) have shown that the type-1 parameters (*g* values and copper hyperfine values) of the Met182Thr mutant were identical to the values of the wild-type enzyme.¹²⁹ The similar *g* values reflect the similar LF transition energies and imply that the Cu 3d character in the HOMO is similar in the wild-type and the mutant. The similar *g* values and covalency of the mutant and the wild-type would account for their equivalent copper hyperfine couplings. The ENDOR frequencies for the histidine nitrogens were unchanged in the mutant from their values in the wild-type enzyme. The spin densities on the nitrogens, which contribute

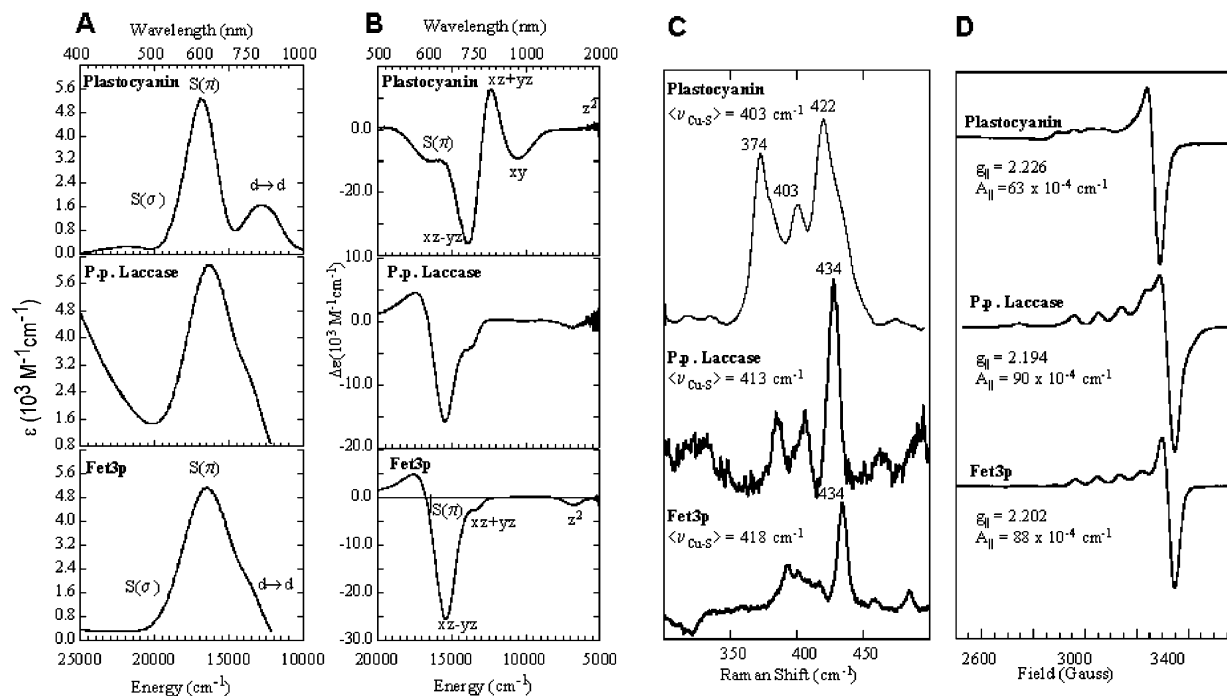


Figure 29. Comparison of the spectral features of plastocyanin, *P.p.* fungal laccase, and Fet3p: (A) low-temperature absorption, (B) MCD, (C) resonance Raman (excitation energy of 647.1 nm), and (D) EPR spectra. Adapted from refs 94 and 134.

to these hyperfine couplings in the mutant and the wild-type, have been found to be similar in DFT calculations. Also, similar β -methylene hyperfine coupling in M182T mutant and wild-type can be explained in part by the rotation of the $\beta\text{C}(\text{Cys})-\text{C}(\text{backbone})$ about the $\text{S}(\text{Cys})-\beta\text{C}(\text{Cys})$ bond in the blue mutant relative to the wild-type. This affects the orientation of the spin density on the $\text{S}(\text{Cys})$ relative to the β -methylene protons.

The spectroscopically calibrated DFT calculations reproduce the differences in electronic structure and bonding among the tetracoordinate green and blue sites and tricoordinate blue (or fungal laccase, vide infra, section 5.2.1) sites. Calculations show that both classes of blue sites have dominant thiolate π bonding character, while the green sites gain significant thiolate σ bond character. In addition, the computed spin densities and ground state covalencies in the tetra- and tricoordinate blue sites correlate well with the experimentally (resonance Raman) determined bond strengths of the $\text{Cu}-\text{S}(\text{Cys})$ interaction (see also section 5.3). The key structural difference is that the blue site has no or a weak axial bond while the green site has a short, strong axial thioether bond.

The spectroscopy of the M182T mutant and its correlation to the wild-type NiR green site and to the classical blue site in plastocyanin emphasizes the role of the axial ligand in determining the geometric and electronic structure of the blue copper site.

5.2. Variation in the Chemical Nature of the Axial Ligand

5.2.1. No Axial Ligand: Fungal Laccases and Fet3p

The type 1 (T1) site in proteins such as fungal laccase and Fet3p have the axial $\text{S}(\text{Met})$ replaced by either a leucine (leu) or a phenylalanine (phe); hence,

no axial ligand is provided by the protein.^{131–133} These proteins form a class of nonaxially ligated T1 sites, which have spectroscopic features that are distinct from the classic blue copper sites in plastocyanin and azurin. In this section, the T1 site of *P. pinsitus* (*P.p.*) fungal laccase⁹⁴ and the T1 site of Fet3p¹³⁴ are compared to that of plastocyanin. To gain further insight into the contribution of the axial ligand, studies were also conducted on the Met axial mutant of *P. pinsitus* fungal laccase.

Both fungal laccase and Fet3p are multicopper oxidases and contain T2 (normal) and T3 (coupled binuclear) copper sites in addition to the T1 site.^{132,133,135,136} The spectral features of the T1 sites were isolated using either differential anion binding or by examination of the T1 and T2 depleted mutants. Figure 29A,B gives a comparison of the absorption and MCD data, respectively, for plastocyanin and the T1 sites of *P.p.* fungal laccase and Fet3p. From the absorption data, the CT spectrum remains intense π and weak pseudo σ , as in plastocyanin, indicating that the site remains trigonally distorted tetrahedral. From the MCD, the $d \rightarrow d$ bands for both *P.p.* fungal laccase and Fet3p shift to higher energy than in plastocyanin. This can also be observed from the absorption spectra, where the $d \rightarrow d$ bands appear as a shoulder at $\sim 13\,700 \text{ cm}^{-1}$, as opposed to the well-resolved feature at $\sim 12\,500 \text{ cm}^{-1}$ in plastocyanin. In addition, in both fungal laccase and Fet3p, the lowest energy transition ($d_{x^2-y^2} \rightarrow d_{z^2}$) is negative, whereas in classic blue copper sites it is positive.^{88,89} This derives from the lack of axial ligand that drops the Cu atom into the $\text{N}(\text{His})-\text{S}(\text{Cys})-\text{N}(\text{His})$ plane, eliminating transition intensity in the z direction. (It is interesting to note, however, that in the Q99L mutant of stellacyanin, the sign of this transition is positive,⁹³ indicating a less trigonal structure.)

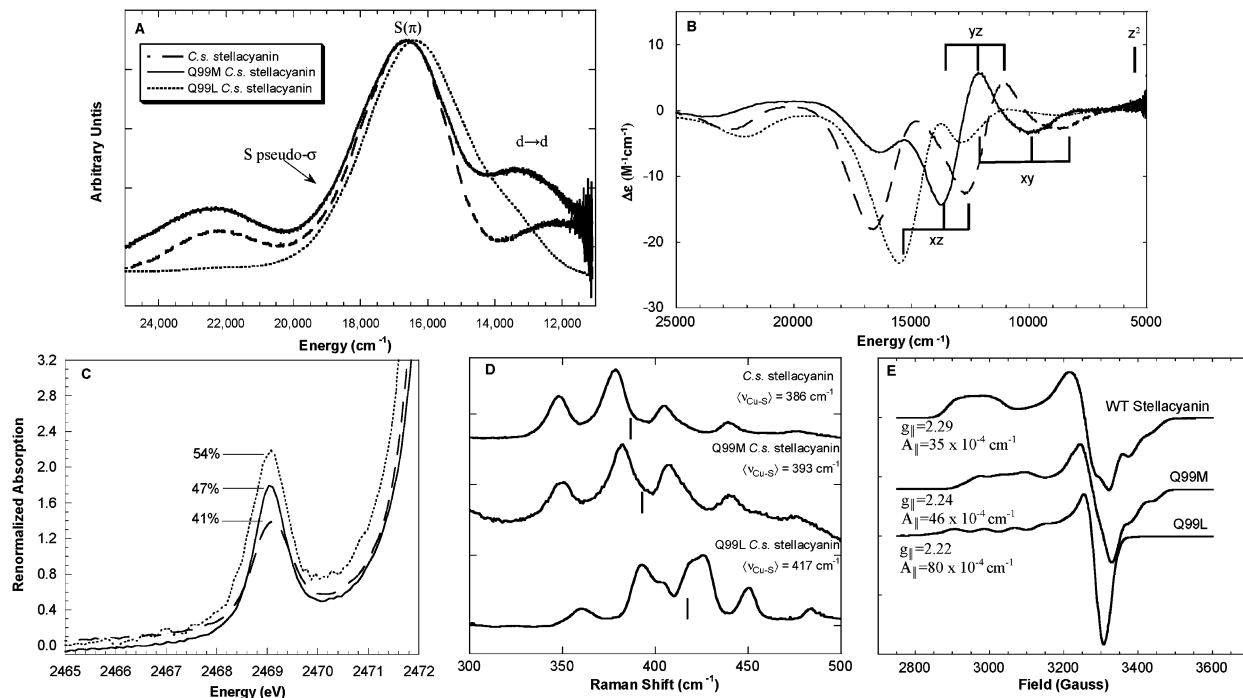


Figure 30. Comparison of the spectral features of *C.s.* stellacyanin and the Q99M and Q99L mutants of stellacyanin: (A) absorption, (B) MCD, (C) S K-edge XAS, and (D) resonance Raman (excitation energy of 647.1 nm) and EPR spectra. Adapted from ref 93.

From Figure 29D, the g values for fungal laccase and Fet3p have decreased relative to plastocyanin, while the A values have increased. The increase in A values for fungal laccase and Fet3p is due in part to the low g values, which in turn derives from the increase in the $3d_{x^2-y^2} \rightarrow 3d_{xy}$ transition energies relative to plastocyanin.¹³⁷ In addition, the increase in A values relative to plastocyanin may be attributed to a decrease in $4s$ mixing into the HOMO. This is supported by DFT calculations, which show that the amount of $4s$ mixing decreases from 1% in plastocyanin to 0% in fungal laccase, due to the more planar geometry of the T1 site in fungal laccase. A detailed analysis of the EPR and optical parameters is found in ref 94. From Figure 29C, the intensity weighted average of the Cu–S stretching frequency determined from resonance Raman data is significantly higher for both *P.p.* fungal laccase and Fet3p (413 and 418 cm^{-1}) than for plastocyanin (403 cm^{-1}), indicating a significantly stronger Cu–S(thiolate) bond. The increase in the strength of the Cu–S(Cys) bond is consistent with the increased oscillator strength of the blue absorption band in fungal laccases relative to plastocyanin and indicates a more covalent Cu–S(thiolate) bond.

The changes in electronic structure described above result from the elimination of the axial interaction, which causes the Cu atom to shift into the N(His)–S(Cys)–N(His) plane increasing the LF transition energies. The absence of the axial ligand is partially compensated for by the increased covalency of the Cu–S(thiolate) bond.

In addition, studies have been performed on the F463M mutant of *P.p.* fungal laccase.⁹⁴ These studies show that replacing the nonligating axial Phe with a weakly ligating Met perturbs the site toward a plastocyanin-like electronic structure. Both the LF

strength and the Cu–S(thiolate) bond strength decrease. These studies further support the contribution of the axial ligand to the electronic structure of blue copper sites.

Finally, it should be noted that the axial ligand also makes a significant contribution to the redox potential of the blue site.^{129,138–146} The contribution of both the axial ligand and the protein environment to the redox potential are discussed in section 7.

5.2.2. Stellacyanin Axial Mutants: Variation of the Axial Ligand in a Fixed Protein Environment

In contrast to the T1 sites of fungal laccase and Fet3p, where the axial interaction has been eliminated, in stellacyanin, the axial S(Met) ligand is replaced by a stronger field O(Gln).¹⁴⁷ To gain further insight into the contributions of the axial ligand, mutagenesis studies have been pursued on the S(Met) and no axial (Leu) mutants of cucumber stellacyanin.⁹³ The wild-type and two mutant proteins span the range of known native, axial interactions in blue copper sites [O(Gln) to S(Met) to no axial (Leu)] and allow the contribution of the axial ligand to be systematically probed within a fixed protein environment.

Figure 30A,B shows the absorption and MCD data for stellacyanin and the Q99M and Q99L mutants.⁹³ The high-intensity $S\pi$ CT transition and relatively weak S pseudo σ CT transition indicate that all of these sites are similarly tetrahedral, indicating that no tetragonal distortion has occurred. From the MCD, on going from wild-type to Q99M to Q99L, the LF transition energies increase. Because there is no tetragonal distortion of the site, this indicates that as the axial ligand is weakened the copper shifts into the N(His)–S(Cys)–N(His) plane and the site becomes more trigonal.

Figure 30C shows the preedge region of the S K-edge XAS spectrum. On going from wild-type to Q99M to Q99L stellacyanin, the preedge intensity increases (from 41 to 47 to 54% S 3p character for wild-type, Q99M, and Q99L stellacyanin, respectively) indicating a more covalent Cu^{II}-S(thiolate) bond. In addition, EXAFS data on the oxidized proteins show that on going from wild-type to Q99M to Q99L stellacyanin the Cu-S(Cys) bond length decreases by 0.04–0.05 Å. These results indicate that as the axial bond is weakened the Cu-S(thiolate) becomes shorter. These results are also supported by resonance Raman data (Figure 30D), which show an increase in the effective Cu-S(thiolate) stretching frequency upon weakening the axial ligand.

Figure 30E shows the EPR data for wild-type stellacyanin and the axial mutants. Across the series, going from wild-type to Q99M to Q99L, the g_{\parallel} values decrease and the A_{\parallel} values increase. The decreased g values and increased A values on going from wild-type to Q99M can be accounted for by the increase in LF transition energies. However, for Q99L in addition to the decrease in g values, an increase in the metal contribution to the HOMO must be included to increase A_{\parallel} . This indicates a higher Z_{eff} in the Q99L mutant, suggesting that elimination of the axial ligand is only partially compensated by the increased donation from the Cu-S(thiolate) bond. This is found more quantitatively through analysis of the XAS edge energies. Across the series (wild-type to Q99M to Q99L stellacyanin), the S K-edge energy remains the same. However, from MCD spectroscopy (based on shifts in bands the d_{xz+yz} transition from 11 200 (WT) to 12 150 (Q99M) to 14 200 cm^{-1} (Q99L) in Figure 30B), the LF increases by 0.13 and 0.38 eV relative to wild-type for Q99M and Q99L stellacyanin, respectively. This requires that the effect of the change in Z_{eff} on the d orbital energy is at least as great as the change in LF. The change in Z_{eff} is likely even larger due to a shift in the sulfur 1s core to deeper binding energy upon increasing the covalency of the Cu-S(thiolate) bond.

The results of these studies also clearly demonstrate that the axial ligand modulates the geometric and electronic structure of the blue copper site. As the axial ligand is weakened, the Cu shifts further into the N(His)-S(Cys)-N(His) plane and the site becomes a more trigonal structure. The Cu-S(thiolate) bond becomes shorter and more covalent, indicating that the strength of the axial ligand inversely affects the strength of the Cu^{II}-S(thiolate) bond, as illustrated schematically in Figure 20. However, the decreased axial interaction is only partially compensated for by the increased donation from the thiolate; thus, the effective nuclear charge on the Cu increases, which impacts the reduction potential of the site (see section 7).

5.3. Electronic Structure Calculations

As presented above, different protein sites with the blue copper ligand set can have different electronic structures. This is directly reflected in the nature of the π vs σ type Cu^{II}-S(thiolate) bonding, which can be understood in terms of the ligand positions along

a coupled distortion coordinate. In the reduced site (section 4), the Cu^I-S(thioether) bond is longer than in normal Cu^I complexes with unconstrained thioether coordination (2.3–2.4 Å),^{7,8} which leads to a short Cu^I-S(thiolate) bond. This structure is relatively stable upon oxidation with only limited metric changes expected in going from the reduced to the oxidized site. Comparison of wild-type and mutant oxidized NiR sites (section 5.1) further demonstrates the role of the axial ligand in determining the position along the coupled distortion coordinate. A shorter, stronger axial Cu^{II}-S(thioether) bond [in conjunction with a longer Cu^{II}-S(thiolate) bond] gives a green site, which is more tetragonally distorted than the blue site. Furthermore, studies of wild-type and mutant stellacyanin active sites (section 5.2) demonstrate that increasing the axial interaction results in a weaker Cu^{II}-S(thiolate) bond and a decreased Z_{eff} of the Cu^{II} ion, which contributes to lowering the reduction potential of the site.

In this section, we use modern DFT to computationally evaluate the role of the protein ligand environment in determining the geometric and electronic structure of the blue copper site in the context of the above data. Figure 31 shows the experimental structure of the oxidized plastocyanin site (A) and optimized equilibrium structures employing different density functionals (B–D). The crystallographic bond lengths involving the Cu^{II} for the experimental structure at 1.33 Å resolution⁷¹ are in good agreement with the more accurate EXAFS distances (Figure 31A); therefore, the crystallographic structure can be used as a reference structure for comparison with the geometry optimized structures. As discussed in section 3.3, functionals with different amounts of HF exchange give different ground state bonding descriptions. In geometry optimizations, the BP86 (Figure 31B) and B3LYP (Figure 31C) functionals using a theoretically converged basis set (BS5) give equilibrium structures with small σ/π ratios [ratio of S(Cys) 3p lobes along (σ) and perpendicular (π) to the Cu-S(Cys) bond], which correspond to dominantly π type Cu^{II}-S(Cys) bonding and optically to blue sites.

Geometry optimizations done by Ryde et al.⁹ using the B3LYP hybrid functional give a π type structure similar to these results. The main difference is in the way the optimized structure is correlated with the protein site. An energy difference (ΔE in Figure 31C) of 7.5 kcal mol⁻¹ is obtained by backtransforming all of the Cu containing internal coordinates of the optimized structure to the experimental geometry. Alternatively, refs 9 and 148 compare optimized structures obtained with and without constrained Cu-S(Met) distances (in the range of 2.62–3.10 Å). This gives an increase in energy due to the protein constraint of 1.2 kcal mol⁻¹.

In contrast to the above results, the spectroscopically adjusted hybrid functional [B(38HF)P86] gives an optimized equilibrium structure (Figure 31D), which is optically green and characterized by a high σ/π ratio (0.8, experimental room and low-temperature values are 1.0 and 2.0, respectively). The B(38HF)P86 geometry is more tetragonal, which is due to the increased HF exchange mixing [HF mixing

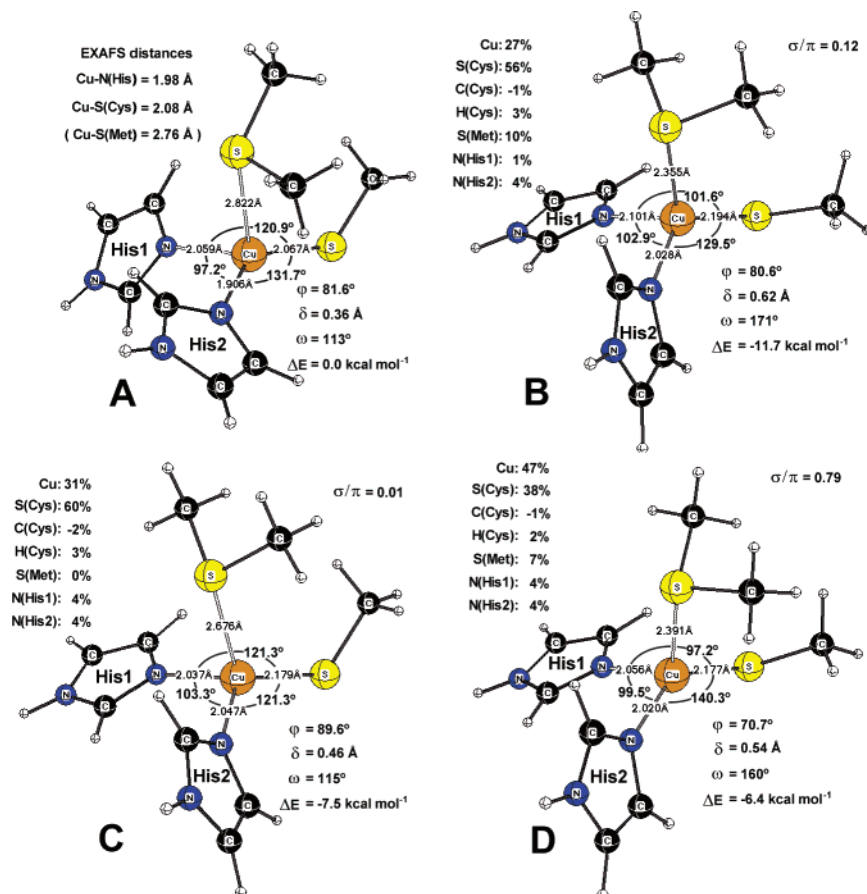


Figure 31. Experimental (A) and optimized structures of oxidized plastocyanin model $[(\text{imidazole})_2\text{Cu}^{\text{II}}(\text{SCH}_3)(\text{S}(\text{CH}_3)_2)]^{1+}$ at (B) BP86/BS5, (C) B3LYP/BS5, and (D) B(38HF)P86/BS5 levels of theory (atomic spin densities from NPA are given in the top insets).

is approximately 20% in B3LYP and 38% in B(38HF)-P86) and the different correlation functional (LYP vs P86)]. The increased HF exchange gives more Cu^{II} character [27% at BP86, 31% at B3LYP, and 47% at B(38HF)P86 levels, from insets in Figure 31], which leads to a larger Jahn–Teller distortion. The energy stabilization of the site due to geometry optimization calculated using the B(38HF)P86 functional is 6.4 kcal mol^{-1} . This energy difference between the experimental blue copper structure and the optimized structures originates from the coupled distortion involving axial $\text{Cu}^{\text{II}}\text{--S}(\text{thioether})$ bond contraction [2.82 Å (exp) \rightarrow 2.39 Å (opt)], $\text{Cu}^{\text{II}}\text{--S}(\text{thiolate})$ bond elongation (2.07 Å \rightarrow 2.18 Å), and the site going toward a more tetragonally distorted geometry ($\varphi = 82^\circ \rightarrow 71^\circ$). In addition to these changes, the thiolate rotates along the $\text{Cu}^{\text{II}}\text{--S}(\text{Cys})$ bond ($\omega = 113^\circ \rightarrow 160^\circ$), and the equatorial imidazole rings adjust their positions relative to the thiolate and thioether ligands [for example, $\text{S}(\text{Cys})\text{--Cu--N}(\text{His1})$ $121^\circ \rightarrow 97^\circ$, $\text{S}(\text{Cys})\text{--Cu--N}(\text{His2})$ $132^\circ \rightarrow 140^\circ$, Cu out of plane distance (δ) 0.36 Å \rightarrow 0.54 Å].

To further study the role of the axial ligand, calculations were also carried out starting from the experimental green site structure of NiR (Figure 32A),¹²⁶ but with the axial thioether eliminated. Geometry optimization gives a planar, trigonal structure (Figure 32B), which closely resembles the experimental, three-coordinate fungal laccase site¹⁴⁹ and is characterized by a highly covalent, π type

$\text{Cu}^{\text{II}}\text{--S}(\text{Cys})$ bond (55% S character). The calculated changes in geometric and electronic structure in going from a strong to no axial ligand parallel the data described in section 5.2 and demonstrate the role of the axial ligand in affecting the electronic structure of the oxidized blue copper site.

Studies have been carried out by Ryde et al.^{9,148} for the reduced site. Using the B3LYP functional, they find that all geometric parameters except the $\text{Cu}^{\text{I}}\text{--S}(\text{Met})$ bond length are within the experimental ranges. Partial optimizations with a constrained $\text{Cu}^{\text{I}}\text{--S}(\text{Met})$ bond at 2.9 Å gave only 1 kcal mol^{-1} for the energy destabilization.

Parallel to the oxidized site, calculations have now been performed for the reduced blue copper site using different functionals; the optimized, equilibrium geometries are summarized in Figure 33. Because of the unreasonably long $\text{Cu}^{\text{I}}\text{--N}(\text{His1})$ bond (2.4 Å, Figure 33A), the crystallographic bond lengths of the reduced site have been replaced by the more accurate EXAFS distances (Table 9, Figure 33A top inset), which provide the reference experimental structure for the reduced blue copper site. The optimized structures obtained using different functionals are similar to each other, and the energy stabilization upon optimization is in the range of 14–21 kcal mol^{-1} [the low and high limits correspond to the BP86 and hybrid B(38HF)P86 results, respectively]. The geometric changes are similar to those observed for the oxidized site [the $\text{Cu}^{\text{I}}\text{--S}(\text{Met})$ gets shorter, $\text{Cu}^{\text{I}}\text{--}$

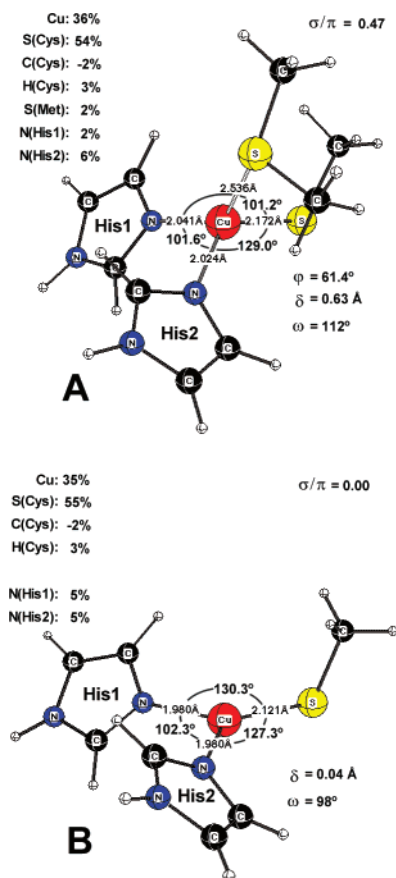


Figure 32. Experimental green site (A) and optimized model [(imidazole)₂Cu^{II}(SCH₃)]¹⁺ at the (B) B(38HF)P86/BS5 level of theory (atomic spin densities from NPA are given in the top insets).

S(Cys) gets longer, thiolate rotates, and the imidazole rings move] but with the site becoming more tetrahedral (reduced) rather than tetragonal (for the oxidized site in Figure 31D).

In summary, density functional calculations indicate that the reduced site is more destabilized in the protein matrix by at least 10 kcal mol⁻¹ relative to the oxidized site. The key structural changes that occur upon geometry optimization are the shortening of the Cu–axial ligand bond, lengthening of the Cu–thiolate bond, and a tetrahedral distortion of the site. There is also a rotation of the thiolate and movement of the equatorial imidazole rings. In the oxidized site, similar but smaller structural differences occur but with a tetragonal, Jahn–Teller distortion, which gives a larger σ/π ratio for the geometry optimized structure (using the spectroscopically adjusted functional) similar to that of the green site in NiR.

6. Spectroscopic and Electronic Structure Studies of Blue Copper Model Complexes

Two structurally defined complexes now exist that model key geometric and electronic features of the blue copper site. The original cupric complex of Kitajima, Fujisawa, and Moro-Oko^{150,151} was based on the tridentate tris(pyrazolyl)hydroborate [HB(pz)₃]¹⁻ ligand and used triphenylmethylthiolate to model the Cys ligand. This gave a trigonally distorted tetrahedral structure **1** with a short, strong

Cu^{II}–S(thiolate) bond (2.1 Å) very similar to the structure of plastocyanin (Figure 34A). Replacing the long axial thioether (2.8 Å) of plastocyanin is an axial N(pz') ligand at a distance of 2.2 Å. Alternatively, Holland and Tolman¹⁵² used the bidentate β -diketiminate ligand. The triphenylmethylthiolate was again used to model Cys, and in this case, the complex **2** was three-coordinate, trigonal planar, with a very similar structure to the three-coordinate blue copper site in fungal laccase (Figure 34B).¹⁴⁹ Availability of these models allowed chemical perturbations not possible in protein systems, which provided new insights into the assignment of spectral features and the contributions of specific bonding interactions to the electronic structure of the blue copper site. Specifically, these allowed the covalency of the Cu^{II}–S(thiolate) bond, the nature of the equatorial nitrogen ligands, and the axial ligand to be varied, and thus, these effects on electronic structure could be further evaluated. These studies^{153,154} utilized the combination of absorption, LT MCD, EPR, resonance Raman excitation profiles, and sulfur K-edge and copper L-edge XAS and DFT calculations.

From the sulfur K-edge data in Figure 35A and the derived covalency numbers in Table 10, the Cu^{II}–S(thiolate) bond in **1** is considerably more covalent than in plastocyanin (52 vs 38% sulfur 3p character in the HOMO).¹⁵⁴ This large change in covalency allows correlation of this contribution to the properties of the blue copper site. From the

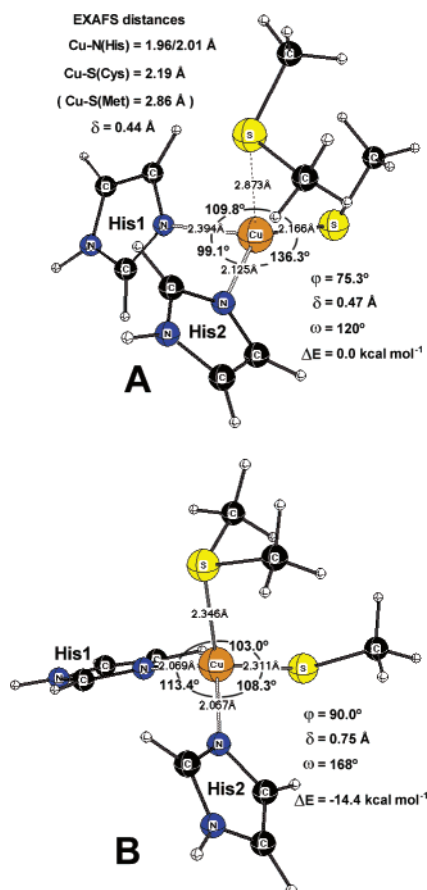


Figure 33. Experimental (A) and optimized structure of reduced plastocyanin model [(imidazole)₂Cu^I(SCH₃)(S(CH₃)₂)⁰ at the (B) BP86/BS5 level of theory.

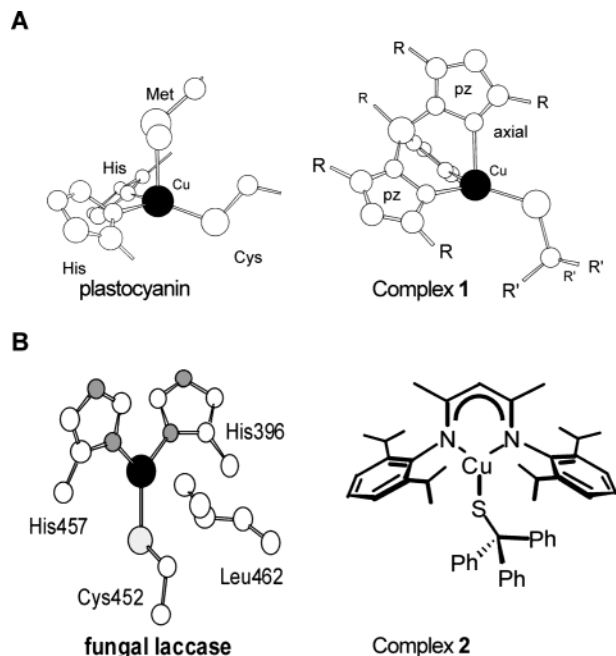


Figure 34. Structures of (A) plastocyanin and complex **1** (Cu–S, 2.13 Å; Cu–N(ax), 2.12 Å; Cu–N(eq1/eq2), 2.03 Å/1.93 Å) and (B) fungal laccase and complex **2** (Cu–S, 2.12 Å; Cu–N(1/2), 1.92 Å/1.92 Å). Adapted from refs 153 and 154.

resonance Raman and absorption results in the last three columns of Table 10, the Cu–S bond is stronger, the reorganization energy in the S(Cys)→Cu CT transition at ~ 600 nm is larger, and the oscillator strength (f) is higher in **1** relative to plastocyanin. These experimentally confirm previous predictions concerning the contribution of this highly covalent bond to the properties of the blue copper site. The effects of this change in Cu^{II}–S(thiolate) covalency on the electronic spectra are defined by the low-temperature absorption and MCD data in Figure 36. There are three important features. First, the LF transitions go down in energy in **1** (bands 1, 3, 4, and 5 from their large C_0/D_0 ratios in MCD/absorption) relative to plastocyanin. This reflects the fact that the structure of **1** (Figure 34A, left) is closer to tetrahedral leading to lower energy LF transitions. As the axial interaction is reduced [i.e., the long Cu–S(thioether) bond in plastocyanin], the copper moves toward the trigonal plane and the LF splittings of the d orbitals increase (vide supra). Second and of particular importance, even though the Cu–S(thiolate) covalency has increased and the π CT transition at ~ 600 nm has gone up in intensity to reflect this, the bands at 450 nm decrease in intensity by a factor of 5 (ϵ of 300 to 60 M⁻¹ cm⁻¹). This clearly excludes the assignment of the bands in the 450 nm region in plastocyanin as relating to the thiolate pseudo σ to Cu^{II} CT transition. Alternatively, along

Table 10. Summary of XAS, Resonance Raman, and Optical Parameters for Complex 1, Complex 2, and Plastocyanin

	S K-edges		Cu L-edges		$\langle\nu_{\text{Cu-S}}\rangle$ (cm ⁻¹)	$E_{\text{R}}(f)$ (cm ⁻¹)	osc. strength
	% S 3p	energy (eV)	% Cu 3d	energy (eV)			
1	52	2469.0	36	930.8	421	2600	0.0777
2	32	2469.2	33	931.3	427	1100	0.0664
plastocyanin	38	2469.0	41	930.7	403	1500	0.0496

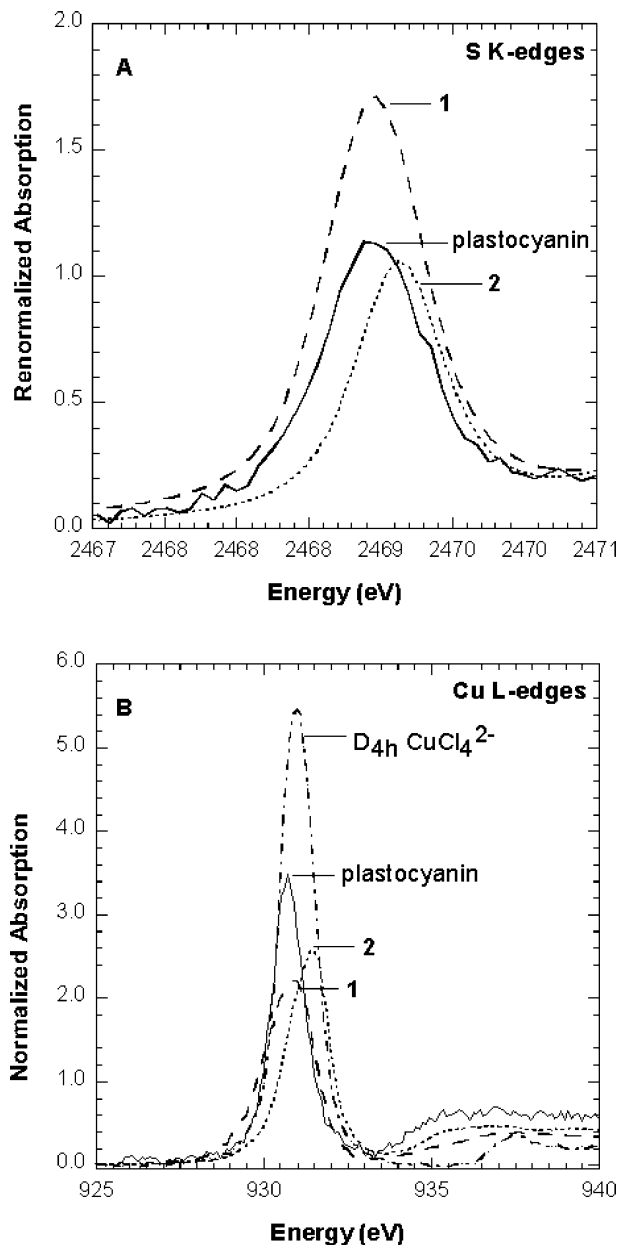


Figure 35. Comparison of the (A) renormalized S K-edge XAS spectra and (B) normalized Cu L₃ spectra of plastocyanin, complex **1**, and complex **2** (Cu L₃-edge data for D_{4h} [CuCl₄]²⁻ are also included). Adapted from refs 153 and 154.

with the decrease in the intensity in this region in **1** relative to plastocyanin, a new low energy band 2 appears in the LT MCD spectrum of **1** but not in plastocyanin (Figure 36B). This reflects the different natures of the valence orbitals of pyrazole relative to imidazole and allows their contributions to the CT spectrum to be elucidated. From Figure 37, both of the free ligands have two π and one σ valence orbital. The σ valence orbitals are greatly stabilized in energy

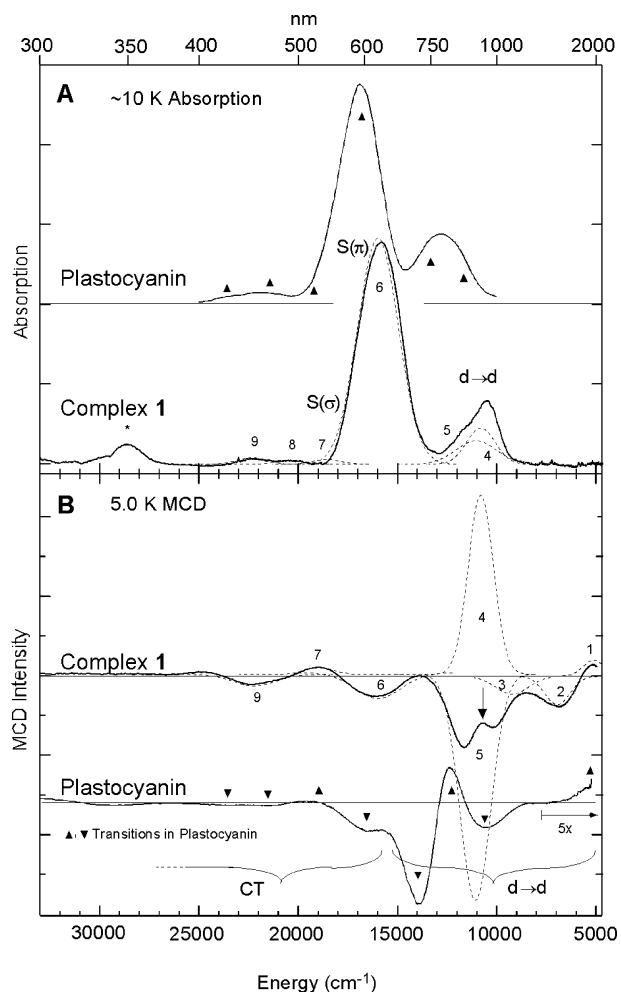


Figure 36. Comparison of (A) low-temperature absorption and (B) MCD spectra of complex **1** and plastocyanin. Adapted from ref 154.

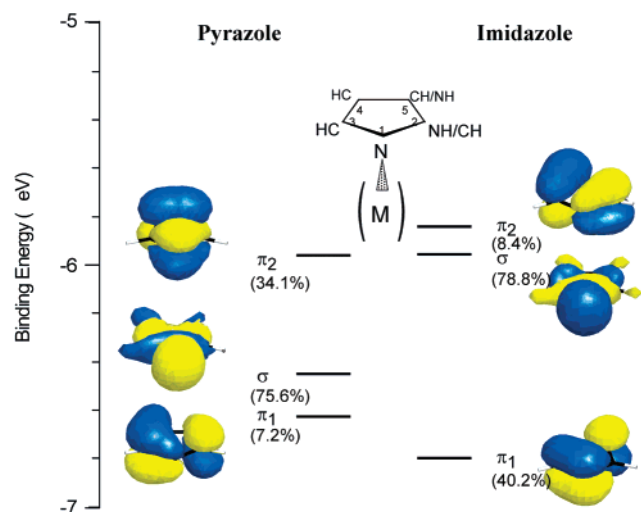


Figure 37. Comparison of the calculated energy level diagrams and valence orbitals of pyrazole (left) and imidazole (right). Adapted from ref 154.

due to σ bonding to the $3d_{x^2-y^2}$ orbital of the copper. The remaining π valence orbitals can contribute CT transitions overlapping the visible region in Figure 36. From Figure 37, the major difference between pyrazole and imidazole is that the dominant contribution on the nitrogen coordinated to the copper (N_1)

is in the higher energy π_1 in imidazole (40%) and in the lower energy π_2 (34%) level in pyrazole. These are split in energy by ~ 0.7 – 1.0 eV in the free ligand. This leads to the assignment of low-energy band 2 as a pyrazole π_2 CT transition in **1**, which is eliminated in plastocyanin due to the small coefficient of N_1 in π_2 of imidazole. Alternatively, the 450 nm band region corresponds to π_1 CT transitions with the higher intensity in plastocyanin reflecting the greatly increased N_1 character in π_1 in imidazole relative to pyrazole.

In addition to defining the contribution of the $\text{Cu}^{\text{II}}\text{--S}(\text{thiolate})$ bond to the spectroscopy and electronic structure, studies on **1** relative to plastocyanin have also defined why this $\text{Cu}^{\text{II}}\text{--S}(\text{thiolate})$ bond is more covalent and demonstrates that this reflects the fact that the tris(pyrazolyl)hydroborate ligand system has a reduced donor interaction with the Cu^{II} relative to the ligand set [2 N(His), S(Met)] of plastocyanin. Summing the sulfur and copper contributions to the HOMO of **1** (Table 10) shows a residual of 12% as compared to 21% in plastocyanin. This reflects the additional contribution of the different endogenous ligand sets to the ground state wave function, which is also reproduced by the DFT calculations in Figures 13 and 38. Changing the trisphenylmethylthiolate to methylthiolate does not change the ground state wave function of **1**.

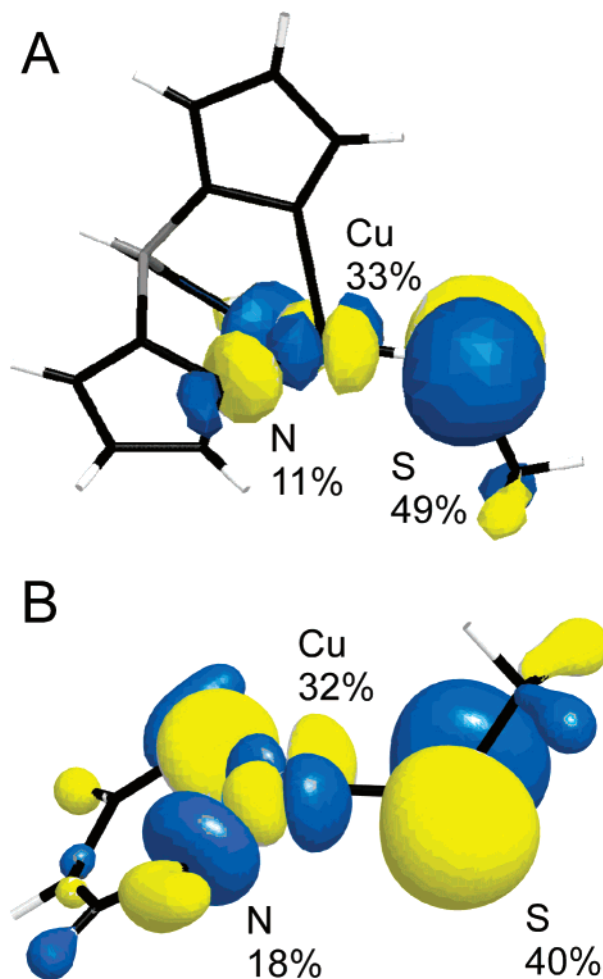


Figure 38. β -LUMO orbital contours for (A) complex **1** and (B) complex **2**. Adapted from refs 153 and 154.

The major contribution to the diminished donor strength of the $[\text{HB}(\text{pz}')_3]^-$ ligand is the misdirected nature of the pyrazolyl σ bonds to the Cu^{II} in the constrained geometry of **1** in Figure 34A. In this structure, the N–N–Cu angles are constrained to be 115° relative to the ideal angle of $\sim 125^\circ$ as found for the C–N–Cu angle of the imidazoles in plastocyanin. Replacing the N(pz')–B bonds with N(pz')–H bonds and geometry optimization in the DFT calculations leads to an angle of 126° . Thus, changes in the donor set [2 N(His), S(Met)] of a blue copper site can strongly effect the covalency of the Cu^{II} –S(thiolate) bond, which plays a key role in the ET properties of the site (section 7).^{8,155}

Finally, it is important to emphasize that this model tris(pyrazolyl)hydroborate ligand system, in addition to allowing better orientation of the pyrazolyl σ bonds (vide supra), is constrained, which contributes to its ability to reproduce the dominant properties of the blue copper site. The HB capping was replaced by H-atoms attached to the distal N-atoms of the pyrazolyl ligand, and the geometry of the $[(\text{pz})_3\text{Cu}^{\text{II}}(\text{SCH}_3)]^0$ complex was optimized. Interestingly, a strong functional dependence was found for the optimized geometry. Using a GGA density functional, such as BP86, with a theoretically converged basis set (BS5), the optimized geometry remains trigonally distorted tetrahedral with pure π Cu–S(thiolate) bonding. In both initial and optimized geometries, this bonding is highly covalent; hence, it has more ligand than metal character; therefore, the effective oxidation state of the Cu is closer to Cu^{I} , which favors a tetrahedral structure. This functional gives a ground state description with 34% Cu and 52% S contributions (36 and 52% experimentally by XAS, respectively) for the constrained N–ligand geometry. As discussed in sections 2.2 and 3.3, for unconstrained Cu complexes, the use of hybrid density functionals is needed to give a reasonable bonding description. Using the B(38HF)-P86 functional with BS5, the global minimum of the $[(\text{pz})_3\text{Cu}^{\text{II}}(\text{SCH}_3)]^0$ complex is a tetragonally distorted geometry with 61% Cu and 24% S contributions and a high σ/π ratio of 6.7.

In comparing complex **2** to complex **1** (Figure 34, both with the same triphenylmethylthiolate ligand), there are dramatic changes in the spectral features/electronic structure, which reflect both of the differences between the donor strengths of the β -diketiminate and the tris(pyrazolyl)borate ligand systems and the loss of the axial ligand in **2**.¹⁵³ From Table 10, the Cu^{II} –S(thiolate) covalency in the HOMO dramatically decreases from 52 to 32% sulfur character. Associated with this (Table 10), the oscillator strength of the S(Cys) π CT transition goes down [0.066 (**2**) vs 0.077 (**1**)], the reorganization energy in the Cu–S bond in this transition decreases (from 2600 to 1100 cm^{-1}), and from Figure 39, the S(Cys) π CT transition has greatly decreased in energy by 2500 cm^{-1} to 750 nm, the lowest energy S(thiolate) \rightarrow Cu^{II} CT transition yet observed. These spectral changes are reproduced by DFT calculations and dominantly reflect the strong donor interaction of the β -diketiminate ligand with the Cu^{II} . From the

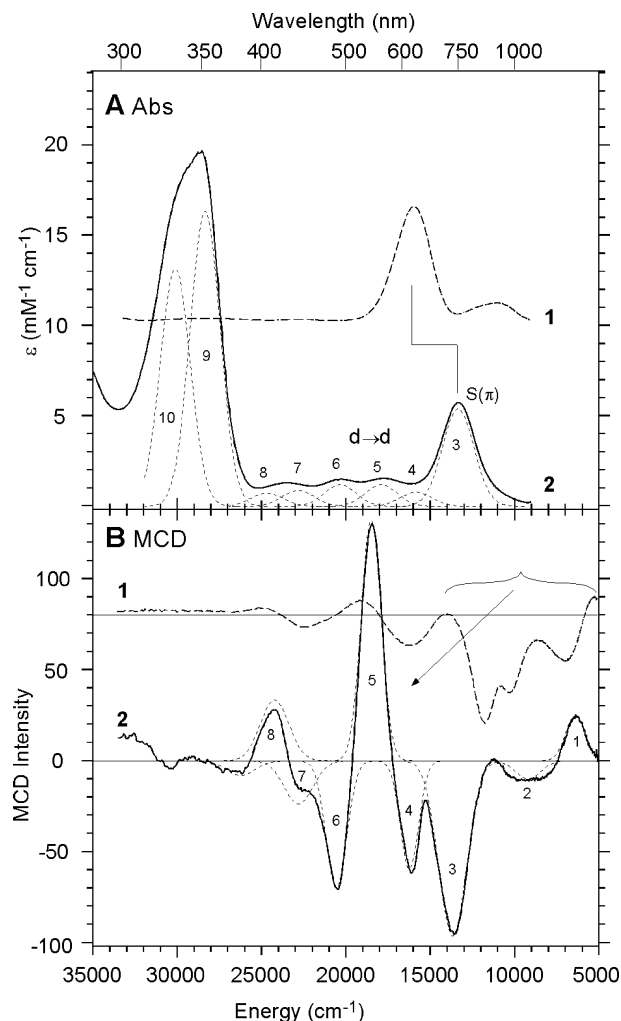


Figure 39. Comparison of (A) low-temperature absorption and (B) MCD spectra of complexes **1** and **2**. Adapted from refs 153 and 154.

MO diagram of the free ligand in Figure 40, the $5b_2$ orbital is at high energy, has almost pure nitrogen character, and is well-oriented and with the proper phase to have a strong σ donor interaction with the $3d_{x^2-y^2}$ orbital on the copper. This can be seen experimentally from the covalency numbers in Table 10, where the sum of sulfur and copper character leaves a residual of 35% for **2** relative to 12% for **1**, which reflects the nitrogen character in the HOMO associated with the different ligand systems. This can also be observed from the large nitrogen superhyperfine splittings in the EPR signal of **2** but not **1** (ref 152) and is also qualitatively reproduced by DFT calculations¹⁵⁴ (Figure 38). The strong donor interaction of the β -diketiminate with the Cu^{II} leads to a trans effect, which reduces the covalency of the Cu^{II} –S(thiolate) bond in the HOMO. This also leads to the low energy of the S(thiolate) π CT transition in **2** relative to **1** (Figure 39) and to that of the blue copper site. The significant β -diketiminate character in the HOMO destabilizes its energy and reduces the bonding interaction of the thiolate with the Cu relative to **1**. There is also an increase in Z_{eff} of **2** relative to **1** (vide infra). Together, these lead to the unusually low energy of this CT transition and its limited thiolate character.

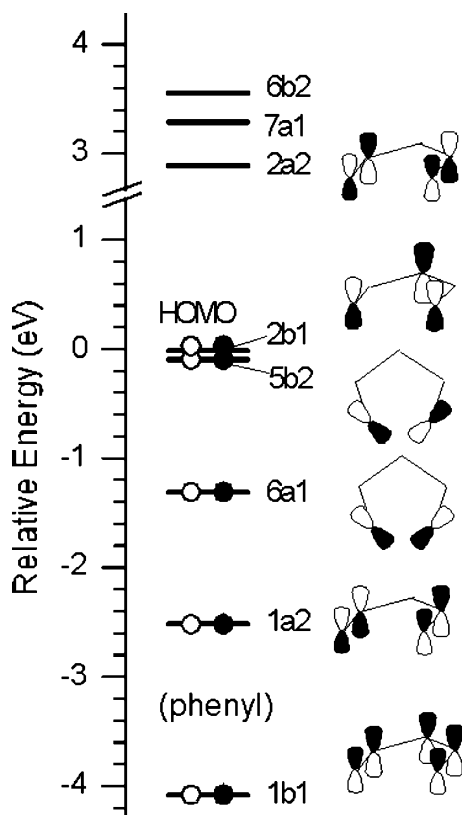


Figure 40. Calculated energy level diagram and valence orbitals of the β -diketiminato ligand. Adapted from ref 153.

Alternatively from the Cu–S effective stretching vibrational frequency in Table 10, column 5, and the Cu–S bond lengths in the crystal structures^{150–152} (Figure 34), the total Cu^{II}–S(thiolate) bond strength of **2** is slightly higher than that of **1**. This derives from the fact that the thiolate in **2** also significantly donates into other unoccupied 4s and 4p orbitals on the Cu^{II} to compensate for the reduced π donor interaction with the HOMO. Thus, while the β -di-

ketiminato is a stronger equatorial donor ligand than the equatorial pyrazolyls, the additional axial pyrazolyl donor interaction in **1** reciprocally weakens the Cu–S(thiolate) bond. This can also be seen from the effective nuclear charges on the coppers in the two complexes determined from the edge energies in Table 10 and DFT calculations, which convert **1** to **2** in several steps.¹⁵⁴

The S K- and Cu L-XAS preedge energies contain information about the relative effective nuclear charge (Z_{eff}) of the copper atom in complexes **1** and **2**. However, the preedge energies also have contributions from the LF splitting and the core level energies, which must be taken into account. On the basis of the similar edge energies in the S K-edge data for the two complexes, the S(thiolate) 1s core levels are at the same energy in **1** and **2**. On the basis of the MCD data (Figure 36), the LF of **2** is larger than in **1**, with the average energy of the d→d transitions in **2** being 6800 cm⁻¹ (~0.8 eV) higher than in **1**. Using this information, the three possibilities for the relative Z_{eff} of Cu in the two complexes, summarized in Figure 41, can be examined.

In case (i), if Z_{eff} in **1** is equal to Z_{eff} in **2**, their d manifolds would be at identical energies, and LF effects alone would dominate the shifts in preedge energies. This suggests that both the S K- and the Cu L-preedge energies for **2** should be at higher energy than **1** by a similar amount that would correspond to the LF difference of the two complexes. However, the magnitudes of the experimentally observed shifts in preedge energies (0.2 eV for the S K-edge and 0.5 eV for the Cu L-edge) are not equivalent, and thus, this case does not apply. In case (ii), if Z_{eff} in **2** were less positive than in **1**, the decreased Z_{eff} of **2** would shift both the core Cu 2p orbitals and the valence orbitals to less deep binding energy, but the magnitude of the effect on the core orbitals should be greater. This suggests that the Cu

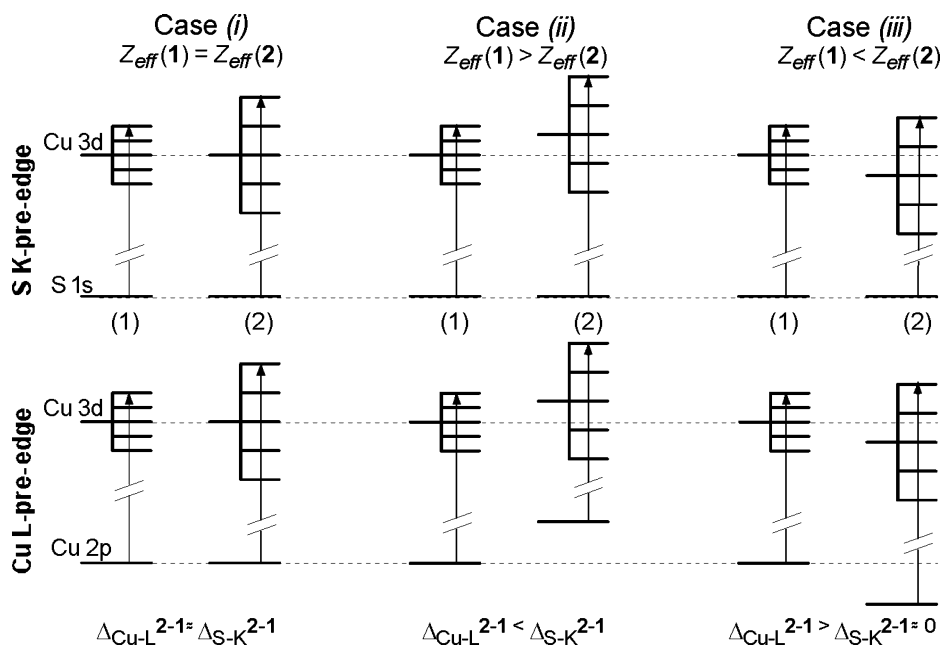


Figure 41. Schematic of the three possible scenarios for relative effective nuclear charge in complexes **1** and **2**. Adapted from ref 153.

L-edge transition of **1** would be at higher energy than for **2**. Furthermore, the decreased Z_{eff} of **2** relative to **1** would combine with the larger LF of **2** to give a large S K-preedge transition energy difference. In addition to the incorrect prediction of the relative Cu L-preedge energies of **2** and **1**, the predicted S K-preedge and Cu L-preedge differences for this case are reversed from what is observed experimentally. It is therefore clear that Z_{eff} of **1** is not greater than or equal to Z_{eff} of **2**. Finally, in case (iii), if Z_{eff} in **2** were more positive than in **1**, for the S K-preedge energy, the increased LF of **2** would be offset by its higher Z_{eff} relative to that of **1**. These two effects would largely cancel, leading to a small S K-preedge energy difference between **1** and **2**. At the Cu L-edge, the increased relative Z_{eff} of **2** would shift both the core and the valence orbitals to deeper binding energy, although again the magnitude of the shift in the core Cu 2p orbitals would be expected to be larger. Therefore, the Cu L-preedge transition energy of **2** would be expected to be at higher energy than the transition of **1**. Only case (iii) predicts an energy shift pattern for both the Cu L-edge and the S K-edge data that is consistent with experiment (Figure 35 and Table 10). This clearly demonstrates that the Z_{eff} on the Cu is higher in the three-coordinate **2** [2N + S] than in the four-coordinate **1** [3N + S].

To gain insight into the differences in the electronic structure of **1** and **2**, DFT calculations have been performed, which systematically alter the geometry of **1** into **2**.¹⁵⁴ The results of these calculations are summarized in Figure 42. First, the axial ligand is removed to give **3***, a hypothetical trigonal bis-(pyrazolyl)hydroborate-ligated Cu thiolate. This greatly increases the LF splitting from $\sim 8000\text{ cm}^{-1}$ in **1** to

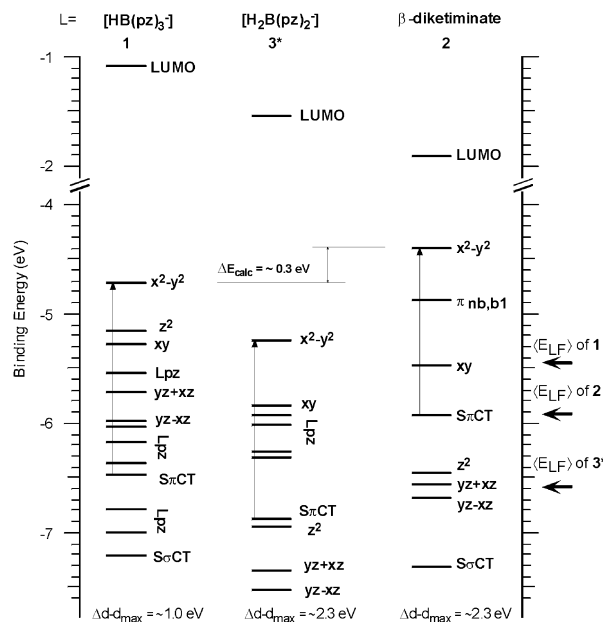


Figure 42. Calculated valence energy level diagrams showing electronic structural changes upon converting from [HB(pz)₃]CuSMe (**1**) → [H₂B(pz)₂]CuSMe (**3***) → [H₃C₃N₂]CuSMe (**2**). The bold, horizontal arrows on the right axis represent the average of the d orbital energies, $\langle E_{\text{LF}} \rangle$ for complexes **1**, **2**, and **3***. In order of decreasing binding energy (i.e., increasing Cu Z_{eff}), these values are -5.47 , -5.92 , and -6.59 eV. Adapted from ref 153.

$\sim 18\,400\text{ cm}^{-1}$ in **3***. In addition, the entire d manifold shifts to deeper binding energy, indicating a more positive Z_{eff} for **3*** due to loss of the fourth (axial) ligand. These results demonstrate a significant contribution from the axial ligand. Next, the N-donor is changed from pyrazole to β -diketimate (i.e., complex **2**). This results in an increase in the energy difference between the HOMO and the S $p\pi$ bonding orbitals (an approximation to the S $p\pi \rightarrow$ Cu CT transition energy) of $\sim 1000\text{ cm}^{-1}$ on going from **3*** to **2**. This is due to a larger splitting of the Sp bonding and antibonding orbitals [as reflected by increased S $p\pi$ character in the HOMO of **3*** (48% S_{calc})], and from destabilization of the S $p\pi$ bonding orbital in **2** due to its substantial Cu–N antibonding character. In addition, the HOMO of **3*** is calculated to lie 0.85 eV to deeper binding energy than the HOMO of **2**. This HOMO shift derives from a decreased effective nuclear charge in **2** relative to **3*** due to more efficient charge donation to the Cu from the β -diketimate ligand relative to the bidentate bis(pyrazolyl)hydroborate ligand. This indicates that the nature of the equatorial ligand is important because its donor strength can modulate the strength of the S $p\pi$ interaction, which in turn can influence the magnitude of the S $p\pi$ bonding–antibonding splitting, and therefore the energy of the S $p\pi \rightarrow$ Cu CT transition.

Thus, in the three-coordinate complex **2**, the d orbital manifold is stabilized relative to that of the four-coordinate complex **1**. This demonstrates that the axial ligand plays a role in modulating Z_{eff} through its additional donor interaction with the copper. The calculations emphasize this, where upon removing the axial ligand from four-coordinate [HB(pz)₃]CuSR₃ to give the hypothetical three-coordinate [H₂B(pz)₂]CuSR₃, the d manifold moves to substantially deeper energy reflecting a higher effective nuclear charge.

Finally, comparing the MCD data of **2** with **1** shows that the axial ligand greatly perturbs the LF at the copper center.¹⁵⁴ This can be seen from the dramatic increase in energies of the LF transitions in **2** relative to **1** in Figure 39. The LF transitions (intense in LT MCD, weak in absorption, band 1, and bands 4–6, which are now at higher energy than the thiolate π CT transition in **2**) shift to higher energy by up to 9000 cm^{-1} on going from **1** to **2**. This reflects the shift of the copper into the trigonal plane in the absence of an axial ligand, which greatly increases the LF splitting of the d orbitals. As described in section 5, an equivalent shift to higher energy of the LF transitions is observed in fungal laccase relative to plastocyanin, the former also having a stronger S(thiolate)–Cu bond. Both effects are due to the absence of the weak axial methionine sulfur ligand of plastocyanin in the blue copper site of fungal laccase. These model studies combined with the protein studies in section 5 show that variation in the axial ligand can effect the Cu^{II}–S(thiolate) bond and modify the ET properties of the blue copper site.

7. Electronic Structure Contributions to Function

As emphasized earlier (ref 77) and throughout this review, unique spectroscopic features of metallopro-

tein active sites reflect novel electronic structures, which can activate the metal centers for reactivity. The blue copper sites are characterized by unique spectroscopic features (intense low-energy CT transitions, small $A_{||}$ values, etc.), which reflect highly covalent Cu–S(Cys) bonds. Here, we consider the contribution of the electronic structure of the blue copper site to its function: long-range, rapid, directional ET. The two functionally significant properties of ET proteins are their redox potential (E_0) and rates of ET (k_{ET}).

7.1. Reduction Potential (E_0)

The reduction potential of the active site can be described by eq 5, where IE is the ionization energy of the site, -4.5 eV is an additional constant to convert from vacuum to the normal hydrogen electrode (240 mV more negative than the standard calomel electrode), and U is the solvation term, which accounts for the reorganization and relative stabilization of the active site environment with change in redox state.

$$E_0 \text{ (eV)} = \text{IE} - 4.5 + \text{U} \quad (5)$$

The protein environment can significantly affect the potential of a metal site through a general reduction of the dielectric relative to that of the aqueous solution and through specific interactions with charged and polar residues and hydrogen bonds, which can selectively stabilize either the reduced or the oxidized sites. The difference in solvation between the reduced and the oxidized sites can be approximated by the Born equation, $U' = (-e^2/2r_0) \times [(\epsilon-1)/\epsilon]$, where e is the unicharge, r_0 is the radius of the solvent sphere around the site, and ϵ is the effective dielectric constant of the environment. In going from aqueous solution ($\epsilon \sim 80$) to a protein-bound site ($\epsilon \sim 4$), the contribution of this term is reduced, raising E_0 . The S(Cys) ligands of the blue copper sites have hydrogen-bonding interactions with the amide N–H groups of the protein, one and two for plastocyanin and azurin, respectively. Hydrogen bonds to sulfur ligands have been shown to have a significant effect on their donor interactions with the metal in the iron sulfur proteins,^{18,156} but this effect has not yet been evaluated for the blue copper sites. The effects of local water dipoles, charge residues, and the carbonyl dipoles of the protein backbone have been considered and modeled for blue copper centers in refs 157 and 158. A useful way to experimentally evaluate the combined effects of the protein environment on the blue copper site is to compare E_0 values of equivalent sites in different proteins. Note that equivalent here means that the oxidized sites have essentially the same spectroscopic features, therefore, geometric and electronic structures; the reduced sites are typically less well-characterized. From the columns of Table 11, the E_0 values of equivalent sites can vary over a range of 450 mV due to general and specific structural features of the protein matrix.

The IE term in eq 5 is governed by the electronic structure of the active site. There are four potential electronic contributions to the ionization energy.²¹

Table 11. Dependence of E_0 on the Axial Ligand in Blue Cu Proteins

	axial ligand and E_0 (mV)			refs
	Phe/Leu/Thr	Met	Gln	
fungal laccase	+770	+680		138–140
azurin	+412	+310	+285	141, 142
cuc. stellacyanin	+500	+420	+260	143, 165
nitrite reductase	+354	+247		129
rusticyanin	+800	+667	+563	144
mavicyanin		+400	+213	145
amicyanin		+250	+165	146

The first of these is the energy of the redox active molecular orbital (RAMO) [the singly occupied HOMO for the oxidized blue Cu proteins], which is strongly affected by the geometry of the LF. Antibonding interactions with the ligands will raise the energy of this orbital and facilitate oxidation of this site (lowering E_0). The second contribution is the change in the effective nuclear charge (Z_{eff}) of the metal upon complexation and is determined by the total donor strength of the ligand set. Lowering Z_{eff} raises the energy of the d orbital manifold, making the site easier to oxidize (lowering E_0). The last two contributions are geometric and electronic relaxations. Geometric relaxation involves a change in geometry of the site upon oxidation, which will stabilize the oxidized site and lower E_0 . Electronic relaxation (which tends to limit the extent of geometric relaxation) refers to the change in electronic structure of the oxidized relative to the reduced site, which stabilizes the oxidized site and also lowers E_0 . For the blue copper site in plastocyanin, from the discussion in section 4, both the geometric and the electronic structures do not significantly change upon oxidation; therefore, the last two terms are small.

The reduction potentials of the classic blue copper site in proteins such as azurin and plastocyanin are in the range of +250 to +350 mV, which is considered to be high relative to aqueous copper ($E_0 = 150$ mV). From section 3, the redox active orbital is $3d_{x^2-y^2}$ and the distorted tetrahedral structure of the blue copper site lower the energy of this orbital relative to that of tetragonal cupric complexes (section 2), resulting in a significantly more positive potential than would be the case for the same ligand set in a tetragonal environment. Unconstrained Cu complexes with N_4 -ligand sets have $E_0 \sim -200$ mV while a constrained distorted tetrahedral complex with tetrakis(imidazole) coordination has $E_0 \sim +350$ mV.¹⁵⁹ These results (in acetonitrile solution) suggest that the tetrahedral structure contributes $\sim +500$ mV to the potential. To this redox active orbital energy contribution to E_0 , one should add the effect of the low dielectric of the blue copper environment ($\epsilon = 80$ in $H_2O \rightarrow \epsilon \sim 4-5$ in the protein), which will also raise the potential by at least ~ 500 mV (estimated from the Born equation = 600 mV using Cu sphere radii of 3.5 Å from polarized continuum model¹⁶⁰⁻¹⁶² calculations).

These contributions toward a high potential are opposed by the thiolate ligand, which as a strong donor will both raise the LF transition energies and significantly lower Z_{eff} , making a major contribution toward stabilizing the oxidized site and lowering the

potential. Both of these effects can be experimentally evaluated by Cu L-edge XAS spectroscopy.

Figure 43 shows a comparison of the Cu L₃-edge (Cu 2p_{3/2} → 3d) data of a tris(pyrazolyl)hydroborate

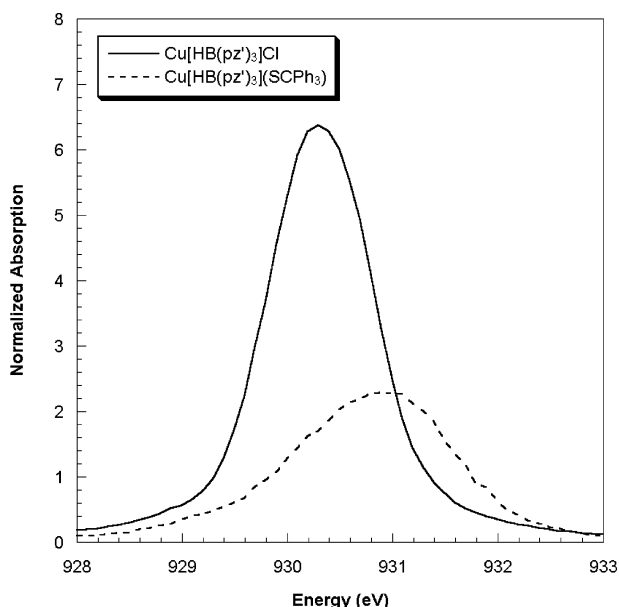


Figure 43. Comparison of normalized Cu L₃ XAS data for Cu[HB(pz')₃]Cl and Cu[HB(pz')₃](SCPh₃).

[HB(pz')₃](chloride)Cu model complex and its (triphenylmethylthiolate) analogue (complex **1**, section 6). The 2p and 3d orbitals are similarly effected by a change in Z_{eff} ; thus, the increase in L₃ energy in **1** primarily reflects the increase in LF on going from a chloride to a thiolate. However, the decrease in L-edge intensity on going from the chloride to thiolate complex directly reflects a decrease in metal d character in the singly occupied HOMO. These two factors result in an experimental decrease of 340 mV in E_0 [from -210 mV (vs Ag wire) for the chloride model complex to -550 mV for the thiolate complex in CH₂Cl₂],¹⁶³ in agreement with estimates from A. B. P. Lever's electrochemical parameter series.¹⁶⁴ It should be noted that the decrease in E_0 on going from an imidazole to a thiolate is estimated to be ~690 mV,¹⁶⁴ indicating that the introduction of a thiolate significantly lowers E_0 relative to the tetrakis(imidazole) complex (above).

The effect of the Cu–S(thioether) bond of the plastocyanin site on E_0 has been the subject of much discussion. We have proposed that the long bond reduces the donor interaction of the thioether with the copper raising E_0 .^{7,8,11} Alternatively, DFT calculations have argued for a very small effect of the axial ligand bond length on the total energy of the oxidized and reduced structures, therefore, little effect on E_0 . However, as presented in section 5.3, this is dependent on the functional and the model for the constrained protein site. This issue is difficult to address experimentally as it is complicated by the coupled distortion of the site. From section 5.1.1, changes of the Cu–S(thioether) bond length are coupled to changes in Cu–S(thiolate) bond and to a tetragonal distortion of the copper environment. Also, different sites along this coordinate are in different proteins

with different environmental effects. An alternative way to address the effect of the axial ligand donor strength on E_0 is to vary the chemical nature of the axial ligand (through mutagenesis) in the same protein environment.

The rows in Table 11 present the most complete compilation of data available at this time.^{129,138–146,165} In going from the limiting case of no axial ligand, to the long Cu–S(thioether) bond, to the short amide carbonyl oxygen–Cu bond at 2.2 (in stellacyanin), the potential decreases by 240 mV. This trend reflects the increased donor strength of the axial ligand and demonstrates that the chemical nature (i.e., donor strength) of the axial ligand can also adjust the potential of the blue copper site in a given protein environment.

7.2. ET Rate (k_{ET})

The reactants come together, the environment of the two sites reorganize to facilitate ET, and the electron is transferred from the reductant to the oxidant. The potential energy diagram for this process is given in Figure 44. From Marcus theory,^{166–168}

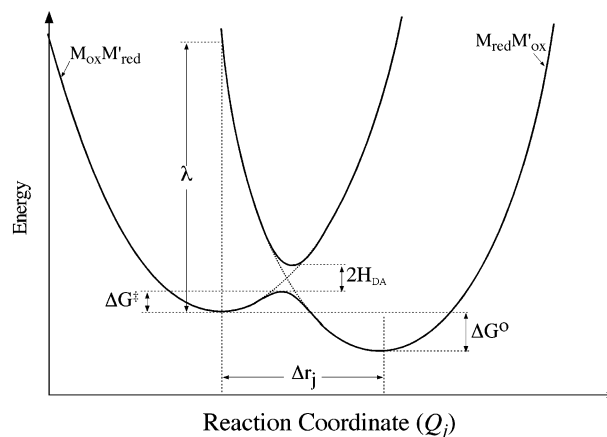


Figure 44. PES diagram for ET between two nearly equivalent complexes ($\Delta G^\circ \neq 0$ but is small). Adapted from ref 3.

the second-order rate constant for bimolecular ET in solution is given by eq 6.

$$k_{\text{ET}} = A\sigma^2 \kappa_{\text{el}} \exp(-\Delta G^\ddagger/RT) \quad (6)$$

$$\Delta G^\ddagger = w + \lambda/4 (1 + \Delta G^\circ/\lambda)^2 \quad (7)$$

$$\lambda = \lambda_o + \lambda_i \quad (8)$$

$$\lambda_o = (\Delta e)^2 [1/2a_1 + 1/2a_2 - 1/r] [1/D_{\text{op}} - 1/D_s] \quad (9)$$

$$\lambda_i = \sum_j k_j (\Delta r_j)^2/2 \quad (10)$$

where $A\sigma^2$ is the collisional frequency conducive to ET and ΔG^\ddagger is the activation energy (or Franck–Condon barrier) to ET. ΔG^\ddagger is defined in eq 7 where w is the work required to bring two charge reactants together, ΔG° is the total free energy for the ET reaction (the difference in reduction potentials, E_0 , which is zero for electron self-exchange), and λ is the total energy required to reorganize the ligand (λ_i) and solvent (λ_o) environments. The outer sphere

term (λ_o) involves repolarization of the solvent molecules as charge Δe is shifted from one center to the other, where in eq 9, a_1 and a_2 are the radii of the reactants, r is the radius of the solvent cavity for ET, and D_{op} and D_s are the optical (square of the refractive index) and static polarizabilities of the solvent, respectively. From eq 10, λ_i is the inner theory organization energy where k_j is the force constant for the ligand–metal vibration along normal mode Q_j being distorted by bond length change Δr_j in the redox reaction.

The quantity κ_{el} in eq 6 is the electron transmission coefficient, which is the normalized probability that the electron will transfer to form products at the isoenergetic geometry in Figure 44. κ_{el} contains H_{DA} , the electronic coupling matrix element, which derives from the overlap of the donor (D) and acceptor (A) orbitals through the protein and splits the PESs at the crossing point in Figure 44 by $2H_{DA}$. When H_{DA} is large, $\kappa_{el} \sim 1$ and the reaction is adiabatic (stays on the lowest energy PES). When H_{DA} is small, $\kappa_{el} \ll 1$ and the reaction is nonadiabatic. For the nonadiabatic case (appropriate for the blue copper proteins), with the reactant and product held at a fixed distance (as in covalently linked redox partners), the first-order rate constant for ET is given by eq 11

$$k_{ET} = (4\pi^3/h^2\lambda kT)^{1/2} [H_{DA}]^2 \exp[-(\Delta G^\circ + \lambda)^2/4\lambda kT] \quad (11)$$

(h and k are the Planck and Boltzmann constants) and is proportional to the electron coupling matrix element squared.

The self-exchange rates for the blue copper sites are very fast ($\sim 10^4$ – 10^6 M $^{-1}$ s $^{-1}$),¹⁶⁹ and from the above considerations (with $\Delta G^\circ = 0$), this requires a small reorganization energy, λ , therefore little change in geometry with redox and a large electronic coupling H_{DA} between metal centers in the protein often separated by large distances.

7.2.1. Reorganization Energy (λ)

For blue copper sites in proteins such as azurin and plastocyanin, the total reorganization energy (λ) has been measured to be 0.7–1.2 eV,^{170–172} and inner reorganization energy (λ_i) has been obtained from the difference in reduced and oxidized structures (0.6–0.8 eV),¹⁷³ resonance Raman distortion data (0.2–0.5 eV),¹⁷⁴ and DFT calculations (0.6–0.7 eV).¹⁷⁵ The outer sphere reorganization energy has been estimated in the range of 0.6–0.7 eV.^{6,170} It is interesting to contrast the small values of λ_i (on the order of 0.5 eV) with the large λ_i values associated with oxidizing normal copper complexes. Using copper tetramine complex as an example, λ_i is calculated to be 1.4 eV¹⁷⁶ (experimental estimates of the total reorganization energy, λ , for normal copper complexes give ~ 2.4 eV for $[\text{Cu}(\text{phen})_2]^{2+/1+}$ ¹⁷⁷). Through calculations, the large value of λ_i for normal Cu complexes can be divided into several components: oxidation and reduction in the reduced and oxidized geometry, respectively, relaxation of Cu^{II}–ligand and Cu^I–ligand bond lengths, and total geometry optimization, which allows the tetragonal distortion of

the oxidized complex. The bond length changes with redox is found to contribute ~ 0.4 eV to λ_i (similar to the bond length changes in the blue Cu site), while the tetragonal distortion contributes an additional ~ 1.0 eV to λ_i .

Thus, a major difference in the contributions to λ_i between the unconstrained complexes and the blue copper site is that only the former undergoes a Jahn–Teller tetragonal distortion from the reduced geometry, which contributes $\sim 70\%$ of λ_i . This derives from the near degeneracy of the Cu 3d_{xy} and 3d_{xz}, 3d_{yz} orbitals for the unconstrained, oxidized copper complex in the reduced geometry (Figure 22A). As indicated in Figure 22C,D for the blue copper site in plastocyanin, the Cu 3d_{x²–y²} and 3d_{xy} orbitals are split in energy by more than 10 000 cm $^{-1}$, which eliminates the Jahn–Teller distorting force, leading to little angular change in geometry with oxidation and thus a low inner sphere reorganization energy λ_i . An interesting issue is the role of the protein in lowering λ_i , which from the discussion in section 5 would be reflected in the different inner sphere reorganization energies along the coupled distortion coordinate of blue copper sites.

7.2.2. Electronic Coupling Matrix Element (H_{DA})

In transferring an electron from a donor to an acceptor site in a biological system, there are three possible contributions to the electron coupling matrix element reflecting orbital overlap between sites: (i) covalency of the ligand–metal bond, (ii) anisotropy in this covalency, and (iii) electron tunneling through the protein ligand. Most effort has been directed toward understanding contribution (iii).^{166,178–184} The rate of electron tunneling through the protein matrix is expected to decay exponentially with increasing distance r_{DA} between the donor and the acceptor (from the van der Waals contact distance r_0) according to eq 12, where β , a parameter reflecting the effectiveness of the protein in mediating ET, is generally found to be ~ 1.1 Å $^{-1}$ (relative to its value of 2.8 Å $^{-1}$ for ET through a vacuum).

$$H_{DA} = (H_{DA}^0) \exp[-\beta/2 (r_{DA} - r_0)] \quad (12)$$

$$H_{DA} = (H_{DA}^0) \pi_i \epsilon_i^{\text{bond}} \pi_j \epsilon_j^{\text{H-bond}} \pi_k \epsilon_k^{\text{space}} \quad (13)$$

Recent studies focus on specific superexchange pathways for the electron through the protein,^{180,185} where the total electron coupling is a product of contributions from individual steps, eq 13. Electron propagation through one covalent bond is attenuated by $\epsilon_i \sim 0.6$, a hydrogen bond reduces H_{DA} by $\sim (0.6)^2$ (about equivalent to two covalent bonds), and a through-space jump is worth $\sim (0.6) \exp[-1.7 - (r - r_{\text{bond}})]$, which is small. Certain pathways from the donor to the acceptor through the protein are found to be more efficient at ET (β sheet is better than ET along the z -axis of an α helix, but ET in the xy direction of an α helix is very efficient), and when several of these pathways exist, there can be constructive or destructive interference of the electron wave at the acceptor site.¹⁸⁴

It should be emphasized that in order for the metal center to couple into these ET pathways, there must be covalency in the ligand–metal bond: $H_{DA}^0 \propto (\alpha)^2$ for the RAMO given by $\psi^* = (1 - \alpha^2)^{1/2} \phi_M - \alpha \phi_L$.¹⁸⁶ The higher the covalency, the higher the value of H_{DA} , where k_{ET} is proportional to H_{DA}^2 .¹⁶⁸ Inequivalence of the ligands at the metal active site would lead to differences (i.e., anisotropy) in this covalency (that is, different α_i for each ligand i) and thus the relative effectiveness of the ligands at mediating ET. As already observed, covalency of a given ligand–metal bond correlates with the CT transitions associated with that ligand. Low-energy, intense CT transitions allow efficient coupling into superexchange pathways; ligand to metal CT creates a hole on the ligand and a superexchange pathway involving propagation of this hole through a valence orbital of the protein, while metal to ligand CT promotes an electron into the LUMO of the protein. Because ligand–metal bonds of relevance here all involve ligand–donor interactions and, therefore, ligand to metal CT transitions of the oxidized site, hole superexchange pathways are expected to dominate in the ET of blue copper proteins.

From the spectroscopy in section 3, the high covalency of the blue copper site of plastocyanin ($\sim 41\%$ Cu character in the LUMO⁹¹) is reflected in the small A_{\parallel} value in the EPR spectrum and quantitated by the L-edge absorption intensity in Figure 14B. That this coupling is highly anisotropic and involves the Cu–S(thiolate) bond is demonstrated by the low energy and high intensity of the CT transition associated with this ligand and quantitated by the sulfur K-edge absorption intensity data⁸⁵ in Figure 15B (38% S(Cys) character in the LUMO). This high anisotropic covalency of the LUMO activates the blue copper site for long-range directional ET through this ligand. Blue Cu proteins such as plastocyanin, nitrite reductase, multicopper oxidases (e.g. ascorbate oxidase), etc. use two sites for ET (Figure 45A, for plastocyanin). The remote site is ~ 13 Å from the blue Cu center, and the most likely pathway to it involves significantly more covalent bonds through the protein than that to the adjacent site, which is only ~ 5 Å from the Cu ion.⁷¹ The through-bond pathway to the remote site goes through the S(Cys) of the blue copper site to an adjacent residue in the primary amino acid sequence, which is at the remote ET site. This Cys–Tyr ET pathway to the remote site in plastocyanin contains 11 covalent bonds. In ascorbate oxidase, Figure 45B, and nitrite reductase, the analogous Cys–His pathway to the T3/T2 cluster or the T2 copper, respectively, contains nine covalent bonds.¹²⁶ On the other hand, the adjacent ET site involves one of the Cu-ligated N(His) side chains, which is on the surface of the protein, and involves two covalent bonds. For plastocyanin, the ET rates to both sites are found to be similar despite the large difference in the lengths of ET paths.⁷⁰ This is attributed to differences in the degree of covalent coupling into the two pathways (i.e., anisotropic covalency), which affects the electronic coupling, H_{DA} .¹⁸⁶ The ET rate to the distant site is facilitated by the large Cu–S(Cys) covalency, which greatly enhances H_{DA} along

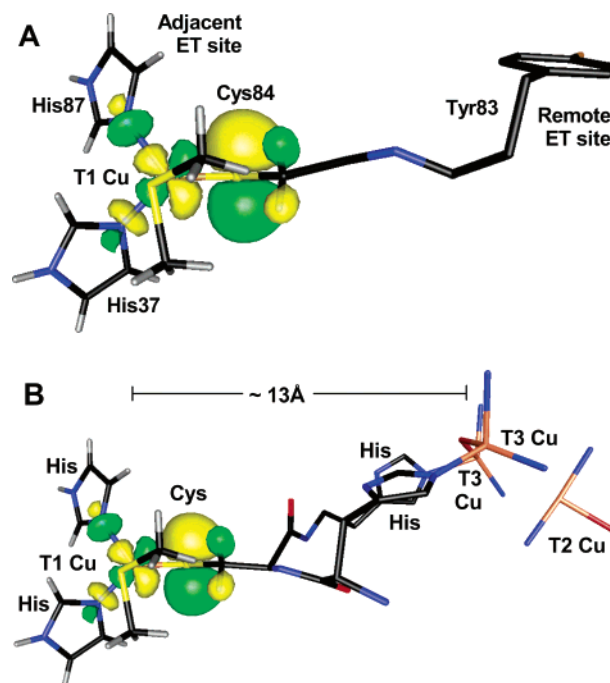


Figure 45. Proposed ET pathway from the T1 site to (A) the remote ET site in plastocyanin and (B) the T2/T3 trinuclear Cu cluster in the multicopper oxidases. Adapted from refs 133 and 187.

this ~ 8 Å longer S(Cys) pathway. Because H_{DA} affects the ET rate quadratically, the ~ 10 -fold greater covalency of S(Cys) over N(His) [the covalency of each N(His) is about 2–4%, from both ENDOR studies and calculations] makes the ET rate similar to a pathway with ~ 9 fewer covalent bonds (using a decay factor of 0.6 per bond). In multicopper proteins (e.g., the multicopper oxidase as in Figure 45B),^{133,187} it seems clear that an electron enters the blue Cu site through the His and leaves the blue site via a Cys–His pathway to the enzymatically active T2 or T3/T2 Cu cluster. Thus, the experimentally determined anisotropic covalency of the redox active orbital in the blue Cu site is important to the intra- and interprotein long-range ET function through its effect on H_{DA} in eq 12.

As developed in section 3, the LT MCD data have shown an additional important final feature of the blue copper LUMO, which is the dominant π bonding interaction of the thiolate with the copper and thus a π pathway for ET. For the multicopper oxidases and nitrite reductase sites, the ET acceptor site is well-defined (the T3 of the trinuclear cluster in the multicopper oxidases and the T2 in nitrite reductase). Nitrite reductase is the simplest case with only one Cys–His pathway to one (T2) copper. This copper is a more “normal” center and involved in a σ bonding interaction with the His of the ET pathway. This T1– π –S(Cys)–N(His)– σ –T2 pathway is now being evaluated.

8. Concluding Comments

This review has attempted to emphasize the information content of different spectroscopic methods and the importance of spectroscopy in bioinorganic chemistry focusing on the unique spectral features of the

blue copper sites and their relations to electronic and geometric structure and to biological function. Ground state spectroscopic methods give g values and metal and ligand A values, which define the nature of the singly occupied MOs and thus covalency. The energies and intensities of LF transitions give direct insight into the geometric and electronic structure of the metal center. CT transitions, defined by their energies, intensities, polarizations, and excited state distortions are sensitive probes of the nature of highly covalent ligand–metal bonds. XAS edges, particularly preedge intensities, experimentally quantitate the coefficients of the ground state wave function, $\psi_{gs} = \alpha \phi_{Md} + \beta \phi_{Mp} + \gamma \phi_{Lp}$. Thus, different spectroscopic methods provide complimentary insight, and the appropriate combination can provide a fundamental understanding of the electronic structure of an active site and its contribution to reactivity. This is strongly complimented by electronic structure calculations (DFT), and it must be emphasized that different functionals and hybrids give different results, and it is important to correlate calculations to spectroscopy and other experimental data to maximize their utility in obtaining further insight into reactivity (i.e., total energies, transition states, and reaction coordinates).

The blue copper sites emphasize the fact that unique spectral features reflect novel geometric and electronic structures that can activate a metal site for reactivity. The unique spectral features of the blue copper site are its intense low-energy S(Cys)→Cu^{II} CT transition and small $A_{||}$ value in EPR, which reflect a highly covalent Cu–S(thiolate) bond, which activates the superexchange pathways associated with this ligand for long-range ET to specific acceptor sites in or on the protein. The protein environment effects on the blue copper geometric and electronic structure (i.e., entatic or rack-induced state) dominantly destabilize the reduced site but also control whether the thiolate is involved in a π (plastocyanin) or σ (nitrite reductase) bonding interaction with the copper. With respect to E_0 , both the protein environment and the axial ligand donor strength can make a significant contribution to shifting the potential into the correct range for efficient ET relative to the physiological electron donor and acceptor.

Finally, it should be emphasized that model studies have contributed greatly to our understanding of the blue copper site. These can involve high symmetry; simple model systems such as copper chloride, which can be studied in detail to understand spectroscopic features; their relation to electronic structure; and the associated energetics in “normal” complexes. They also must involve biomimetic ligand systems designed to evaluate specific geometric and electronic features of an active site. These can be complicated by the facts that the designed ligand itself can have constraints and the chemical nature of the ligand set can differ from that of the protein site. However, for the blue copper site, biomimetic studies have allowed perturbations of the nature of the thiolate and of the axial ligand and thus direct evaluation of these contributions to the spectroscopic features and electronic structure of the blue copper proteins.

9. Acknowledgment

E.I.S. thanks his students and collaborators as cited in the references for their key contributions to this research. This work was supported by NSF CHE-9980549 (E.I.S.). SSRL operations are funded by the Department of Energy, Office of Basic Energy Sciences. The Structural Molecular Biology program is supported by the National Institutes of Health, National Center for Research Resources, Biomedical Technology Program and by the Department of Energy, Office of Biological and Environmental Research. We thank the Clark Center at Stanford and the Bio-X program for computational time on a Silicon Graphics Origin 3800 shared memory super-computer.

10. References

- (1) Abola, E. E.; Bernstein, F. C.; Bryant, S. H.; Koetzle, T. F.; Weng, J.; Allen, F. H.; Bergerhoff, G.; Sievers, R., Eds. Protein Data Bank. Crystallographic Databases—Information Content, Software Systems and Scientific Applications. Data Commission of the International Union of Crystallography: Bonn, Germany, 1987.
- (2) Bernstein, T.; Koetzle, T. F.; Williams, G. J. B.; Meyer, F. E.; Brice, M. D.; Rodgers, J. R.; Kennard, O.; Shimanouchi, T.; Tasumi, M. *J. Mol. Biol.* **1977**, *112*, 535.
- (3) Holm, R. H.; Kennepohl, P.; Solomon, E. I. *Chem. Rev.* **1996**, *96*, 2239.
- (4) Williams, R. J. P. *Eur. J. Biochem.* **1995**, *234*, 363.
- (5) Malmström, B. G. *Eur. J. Biochem.* **1994**, *223*, 711.
- (6) Gray, H. B.; Malmström, B. G.; Williams, R. J. P. *J. Biol. Inorg. Chem.* **2000**, *5*, 551.
- (7) Guckert, J. A.; Lowery, M. D.; Solomon, E. I. *J. Am. Chem. Soc.* **1995**, *117*, 2817.
- (8) Randall, D. W.; Gamelin, D. R.; LaCroix, L. B.; Solomon, E. I. *J. Biol. Inorg. Chem.* **2000**, *5*, 16.
- (9) Ryde, U.; Olsson, M. H. M.; Pierloot, K.; Roos, B. O. *J. Mol. Biol.* **1996**, *261*, 586.
- (10) Ryde, U.; Olsson, M. H. M.; Pierloot, K. *Theor. Comput. Chem.* **2001**, *9*, 1.
- (11) Solomon, E. I.; Penfield, K. W.; Gewirth, A. A.; Lowery, M. D.; Shadle, S. E.; Guckert, J. A.; Lacroix, L. B. *Inorg. Chim. Acta* **1996**, *243*, 67.
- (12) Solomon, E. I. In *Comments on Inorganic Chemistry*; Sutin, N., Ed.; Gordon and Breach: New York, 1984; Vol. III.
- (13) Solomon, E. I.; Hanson, M. A. In *Inorganic Electronic Structure and Spectroscopy*; Solomon, E. I., Lever, A. B. P., Eds.; Wiley: New York, 1999; Vol. 2.
- (14) Lehnert, N.; DeBeer George, S.; Solomon, E. I. *Curr. Opin. Chem. Biol.* **2001**, *5*, 176.
- (15) Neese, F.; Solomon, E. I. *Inorg. Chem.* **1999**, *38*, 1847.
- (16) Hedman, B.; Hodgson, K. O.; Solomon, E. I. *J. Am. Chem. Soc.* **1990**, *112*, 1643.
- (17) George, S. J.; Lowery, M. D.; Solomon, E. I.; Cramer, S. P. *J. Am. Chem. Soc.* **1993**, *115*, 2968.
- (18) Glaser, T.; Hedman, B.; Hodgson, K. O.; Solomon, E. I. *Acc. Chem. Res.* **2000**, *33*, 859.
- (19) Hecht, M. H.; Lindau, I. *J. Electron Spectrosc. Relat. Phenom.* **1985**, *35*, 211.
- (20) Kennepohl, P.; Solomon, E. I. *Inorg. Chem.* **2003**, *42*, 679.
- (21) Kennepohl, P.; Solomon, E. I. *Inorg. Chem.* **2003**, *42*, 689.
- (22) Kennepohl, P.; Solomon, E. I. *Inorg. Chem.* **2003**, *42*, 696.
- (23) Hoffmann, R. *J. Chem. Phys.* **1963**, *39*, 1397.
- (24) Hückel, E. *Z. Phys.* **1931**, *70*, 204.
- (25) Thiel, W.; Voityuk, A. *Theor. Chim. Acta* **1992**, *81*, 391.
- (26) Anderson, W. P.; Edwards, W. D.; Zerner, M. C. *Inorg. Chem.* **1986**, *25*, 2728.
- (27) Martin, C. H.; Zerner, M. C. In *Inorganic Electronic Structure and Spectroscopy*; Solomon, E. I., Lever, A. B. P., Eds.; John Wiley and Sons: New York, 1999; Vol. I: Methodology.
- (28) Hehre, W. J.; Random, L.; Schleyer, P. v. R.; Pople, J. A. *Ab Initio Molecular Orbital Theory*; Wiley: New York, 1986.
- (29) Koch, W.; Holthausen, M. C. *A Chemist's Guide to Density Functional Theory*; Wiley-VCH: Weinheim, 2000.
- (30) Slater, J. C. *The Calculation of Molecular Orbitals*; John Wiley & Sons: New York, 1979.
- (31) Connolly, J. W. D. *Mod. Theor. Chem.* **1977**, *7*, 105.
- (32) Roesch, N. In *Electrons in Finite and Infinite Structures*; Phariseau, P., Scheire, J. C., Eds.; Wiley: New York, 1977; Vol. V24.

- (33) Johnson, K. H.; Norman, J. G., Jr.; Connolly, J. W. D. In *Computational Methods for Large Molecules and Localized States in Solids: Proc. Symp.*; Herman, F., McLean, A. D., Nesbet, R. K., Eds.; Plenum: New York, 1973.
- (34) Kohn, W.; Sham, L. J. *Phys. Rev. A* **1965**, *140*, 1133.
- (35) Hohenberg, P.; Kohn, W. *Phys. Rev. B* **1964**, *136*, 864.
- (36) Slater, J. C. *The Self-Consistent Field for Molecules and Solids. Quantum Theory*; McGraw-Hill: New York, 1974.
- (37) Perdew, J. P.; Chevary, J. A.; Vosko, S. H.; Jackson, K. A.; Pederson, M. R.; Singh, D. J.; Fiolhais, C. *Phys. Rev. B: Condens. Matter* **1992**, *46*, 6671.
- (38) Perdew, J. P.; Burke, K.; Ernzerhof, M. *Phys. Rev. Lett.* **1996**, *77*, 3865.
- (39) Gritsenko, O. V.; Schipper, P. R. T.; Baerends, E. J. *J. Chem. Phys.* **1997**, *107*, 5007.
- (40) Becke, A. D. *Phys. Rev. A: Gen. Phys.* **1988**, *38*, 3098.
- (41) Lee, C.; Yang, W.; Parr, R. G. *Phys. Rev. B: Condens. Matter* **1988**, *37*, 785.
- (42) Becke, A. D. *J. Chem. Phys.* **1993**, *98*, 5648.
- (43) Szilagy, R. K.; Metz, M.; Solomon, E. I. *J. Phys. Chem. A* **2002**, *106*, 2994.
- (44) Szilagy, R. K.; Solomon, E. I. *Curr. Opin. Chem. Biol.* **2002**, *6*, 250.
- (45) Desjardins, S. R.; Penfield, K. W.; Cohen, S. L.; Musselman, R. L.; Solomon, E. I. *J. Am. Chem. Soc.* **1983**, *105*, 4590.
- (46) Gewirth, A. A.; Cohen, S. L.; Schugar, H. J.; Solomon, E. I. *Inorg. Chem.* **1987**, *26*, 1133.
- (47) Didziulis, S. V.; Cohen, S. L.; Gewirth, A. A.; Solomon, E. I. *J. Am. Chem. Soc.* **1988**, *110*, 250.
- (48) Perdew, J. P. *Phys. Rev. B: Condens. Matter* **1986**, *33*, 8822.
- (49) Becke, A. D. *J. Chem. Phys.* **1993**, *98*, 5648.
- (50) Mulliken, R. S. *J. Chem. Phys.* **1955**, *23*, 1833.
- (51) Siegbahn, P. E. M.; Blomberg, M. R. A. *Chem. Rev.* **2000**, *100*, 421.
- (52) Schaefer, A.; Horn, H.; Ahlrichs, R. *J. Chem. Phys.* **1992**, *97*, 2571.
- (53) Hariharan, P. C.; Pople, J. A. *Theor. Chim. Acta* **1973**, *28*, 213.
- (54) Francl, M. M.; Pietro, W. J.; Hehre, W. J.; Binkley, J. S.; Gordon, M. S.; DeFrees, D. J.; Pople, J. A. *J. Chem. Phys.* **1982**, *77*, 3654.
- (55) Rassolov, V. A.; Pople, J. A.; Ratner, M. A.; Windus, T. L. *J. Chem. Phys.* **1998**, *109*, 1223.
- (56) Baerends, E. J.; Ellis, D. E.; Ros, P. *Chem. Phys.* **1973**, *2*, 41.
- (57) Versluis, L.; Ziegler, T. *J. Chem. Phys.* **1988**, *88*, 322.
- (58) Te Velde, G.; Baerends, E. J. *J. Comput. Phys.* **1992**, *99*, 84.
- (59) Guerra, C. F.; Snijders, J. G.; Te Velde, G.; Baerends, E. J. *Theor. Chem. Acc.* **1998**, *99*, 391.
- (60) Velde, G. T.; Bickelhaupt, F. M.; Baerends, E. J.; Guerra, C. F.; Van Gisbergen, S. J. A.; Snijders, J. G.; Ziegler, T. *J. Comput. Chem.* **2001**, *22*, 931.
- (61) Head-Gordon, M.; Pople, J. A.; Frisch, M. J. *Chem. Phys. Lett.* **1988**, *153*, 503.
- (62) Saebo, S.; Almlöf, J. *Chem. Phys. Lett.* **1989**, *154*, 83.
- (63) Frisch, M. J.; Head-Gordon, M.; Pople, J. A. *Chem. Phys. Lett.* **1990**, *166*, 275.
- (64) Frisch, M. J.; Head-Gordon, M.; Pople, J. A. *Chem. Phys. Lett.* **1990**, *166*, 281.
- (65) Head-Gordon, M.; Head-Gordon, T. *Chem. Phys. Lett.* **1994**, *220*, 122.
- (66) Krishnan, R.; Pople, J. A. *Int. J. Quantum Chem.* **1978**, *14*, 91.
- (67) Pople, J. A.; Head-Gordon, M.; Raghavachari, K. *J. Chem. Phys.* **1987**, *87*, 5968.
- (68) Harlow, R. L.; Wells, W. J., III; Watt, G. W.; Simonsen, S. H. *Inorg. Chem.* **1974**, *13*, 2106.
- (69) Solomon, E. I.; Hare, J. W.; Gray, H. B. *Proc. Natl. Acad. Sci. U.S.A.* **1976**, *73*, 1389.
- (70) Guss, J. M.; Freeman, H. C. *J. Mol. Biol.* **1983**, *169*, 521.
- (71) Guss, J. M.; Bartunik, H. D.; Freeman, H. C. *Acta Crystallogr. B* **1992**, *B48*, 790.
- (72) Adman, E. T. In *Advances in Protein Chemistry*; Anfinsen, C. B., Richards, F. M., Edsall, J. T., Eisenberg, D. S., Eds.; Academic Press: San Diego, 1991; Vol. 42.
- (73) Sykes, A. G. *Adv. Inorg. Chem.* **1991**, *107*, 377.
- (74) Messerschmidt, A. *Struct. Bonding* **1998**, *90*, 37.
- (75) Baker, E. N. *Encyclopedia of Inorganic Chemistry*; Wiley: Chichester, 1994.
- (76) Solomon, E. I.; Baldwin, M. J.; Lowery, M. D. *Chem. Rev.* **1992**, *92*, 521.
- (77) Solomon, E. I.; Lowery, M. D. *Science* **1993**, *259*, 1575.
- (78) Penfield, K. W.; Gay, R. R.; Himmelwright, R. S.; Eickman, N. C.; Freeman, H. C.; Solomon, E. I. *J. Am. Chem. Soc.* **1981**, *103*, 4382.
- (79) Coremans, J. W. A. P. O. G.; Groenen, E. I. J.; Canters, G. W.; Nar, H.; Messerschmidt, A. *J. Am. Chem. Soc.* **1994**, *116*, 3097.
- (80) Duliba, E. P. H.; Gregory, C.; Belford, R. L. *Inorg. Chem.* **1982**, *22*, 577.
- (81) Schweiger, A.; Gunthard, H. H. *Chem. Phys.* **1978**, *32*, 35.
- (82) Brown, T. G.; Hoffman, B. M. *Mol. Phys.* **1980**, *39*, 1073.
- (83) Sharnoff, M. *J. Chem. Phys.* **1965**, *42*, 3383.
- (84) Roberts, J. E.; Brown, T. G.; Hoffman, B. M.; Peisach, J. *J. Am. Chem. Soc.* **1980**, *102*, 825.
- (85) Shadle, S. E.; Penner-Hahn, J. E.; Schugar, H. J.; Hedman, B.; Hodgson, K. O.; Solomon, E. I. *J. Am. Chem. Soc.* **1993**, *115*, 767.
- (86) Scott, R. A.; Hahn, J. E.; Doniach, S.; Freeman, H. C.; Hodgson, K. O. *J. Am. Chem. Soc.* **1982**, *104*, 5364.
- (87) Penfield, K. W.; Gewirth, A. A.; Solomon, E. I. *J. Am. Chem. Soc.* **1985**, *107*, 4519.
- (88) Gewirth, A. A.; Solomon, E. I. *J. Am. Chem. Soc.* **1988**, *110*, 3811.
- (89) LaCroix, L. B.; Shadle, S. E.; Wang, Y. N.; Averill, B. A.; Hedman, B.; Hodgson, K. O.; Solomon, E. I. *J. Am. Chem. Soc.* **1996**, *118*, 7755.
- (90) Schwarz, K. *Phys. Rev. B* **1972**, *5*, 2466.
- (91) George, S. J.; Lowery, M. D.; Solomon, E. I.; Cramer, S. P. *J. Am. Chem. Soc.* **1993**, *115*, 2968.
- (92) Hughley, J. L.; Fawcett, T. G.; Rudich, S. M.; Lalancette, R. A.; Potenza, J. A.; Schugar, H. J. *J. Am. Chem. Soc.* **1979**, *101*, 2617.
- (93) DeBeer George, S.; Basumallick, L.; Szilagy, R. K.; Randall, D. W.; Hill, M. G.; Nersissian, A. M.; Valentine, J. S.; Hedmann, B.; Hodgson, K. O.; Solomon, E. I. *J. Am. Chem. Soc.* **2003**, *125* (37), 11314–11328.
- (94) Palmer, A. E.; Randall, D. W.; Xu, F.; Solomon, E. I. *J. Am. Chem. Soc.* **1999**, *121*, 7138.
- (95) Foster, J. P.; Weinhold, F. *J. Am. Chem. Soc.* **1980**, *102*, 7211.
- (96) Reed, A. E.; Curtiss, L. A.; Weinhold, F. *Chem. Rev.* **1988**, *88*, 899.
- (97) Carpenter, J. E.; Weinhold, F. *J. Mol. Struct. (THEOCHEM)* **1988**, *169*, 41.
- (98) Bader, R. F. W. *Atoms in Molecules: A Quantum Theory*; Oxford University Press: Oxford, 1990.
- (99) Pierloot, K.; De Kerpel, J. O. A.; Ryde, U.; Olsson, M. H. M.; Roos, B. O. *J. Am. Chem. Soc.* **1998**, *120*, 13156.
- (100) Casida, M. E. In *Recent Advances in Density Functional Theory*; Chong, D. P., Ed.; World Scientific: Singapore, 1995; Vol. 1.
- (101) Gross, E. U. K. In *Density Functional Theory*; Nalewajski, R. F., Ed.; Springer: Heidelberg, 1996.
- (102) Stratmann, R. E.; Scuseria, G. E.; Frish, M. J. *J. Chem. Phys.* **1998**, *109*, 8218.
- (103) Frisch, M. J.; Trucks, G. W.; Schlegel, H. B.; Scuseria, G. E.; Robb, M. A.; Cheeseman, J. R.; Zakrzewski, V. G.; Montgomery, J. A., Jr.; Stratmann, R. E.; Burant, J. C.; Dapprich, S.; Millam, J. M.; Daniels, A. D.; Kudin, K. N.; Strain, M. C.; Farkas, O.; Tomasi, J.; Barone, V.; Cossi, M.; Cammi, R.; Mennucci, B.; Pomelli, C.; Adamo, C.; Clifford, S.; Ochterski, J.; Petersson, G. A.; Ayala, P. Y.; Cui, Q.; Morokuma, K.; Malick, D. K.; Rabuck, A. D.; Raghavachari, K.; Foresman, J. B.; Cioslowski, J.; Ortiz, J. V.; Stefanov, B. B.; Liu, G.; Liashenko, A.; Piskorz, P.; Komaromi, I.; Gomperts, R.; Martin, R. L.; Fox, D. J.; Keith, T.; Al-Laham, M. A.; Peng, C. Y.; Nanayakkara, A.; Gonzalez, C.; Challacombe, M.; Gill, P. M. W.; Johnson, B. G.; Chen, W.; Wong, M. W.; Andres, J. L.; Head-Gordon, M.; Replogle, E. S.; Pople, J. A. *Gaussian 98*, revision A.11; Gaussian, Inc.: Pittsburgh, PA, 1998.
- (104) Yeh, J. J. *At. Data Nucl. Data Tables* **1985**, *32*, 1.
- (105) Kau, L. S.; Spira-Solomon, D. J.; Pennerhahn, J. E.; Hodgson, K. O.; Solomon, E. I. *J. Am. Chem. Soc.* **1987**, *109*, 6433.
- (106) Penner-Hahn, J. X-ray Absorption Studies of Metalloprotein Structure: Cytochrome P450, Horeradish Peroxidase, Plastocyanin and Laccase. Thesis, Stanford University, 1984.
- (107) Guss, J. M.; Harrowell, P. R.; Murata, M.; Norris, V. A.; Freeman, H. C. *J. Mol. Biol.* **1986**, *192*, 361.
- (108) Inoue, T.; Gotowda, M.; Sugawara, H.; Kohzuma, T.; Yoshizaki, F.; Sugimura, Y.; Kai, Y. *Biochemistry* **1999**, *38*, 13853.
- (109) Inoue, T.; Sugawara, H.; Hamanaka, S.; Tsukui, H.; Suzuki, E.; Kohzuma, T.; Kai, Y. *Biochemistry* **1999**, *38*, 6063.
- (110) Baker, E. N. *J. Mol. Biol.* **1988**, *203*, 1071.
- (111) Shepard, W. E. B.; Anderson, B. F.; Lewandoski, D. A.; Norris, G. E.; Baker, E. N. *J. Am. Chem. Soc.* **1990**, *112*, 7817.
- (112) Dodd, F. E.; Abraham, Z. H. L.; Eady, R. R.; Hasnain, S. S. *Acta Crystallogr. D* **2000**, *56*, 690.
- (113) Freeman, H. C. In *Spectroscopic Methods in Bioinorganic Chemistry*; Solomon, E. I., Hodgson, K. O., Eds.; ACS Symposium Series; Washington, DC, 1998; Vol. 692.
- (114) Ellis, P. J. Studies of Metalloproteins using EXAFS and XRD. Thesis, University of Sydney, 1995.
- (115) Tullius, T. D. Structures of Metal Complexes in Biological Systems: EXAFS Studies of Blue Copper Proteins, Xanthine Oxidase and Vanadocytes. Thesis, Stanford University, 1979.
- (116) Co, M. S.; Hodgson, K. O. In *Copper Proteins and Copper Enzymes*; Lontie, R., Ed.; CRC Press: Boca Raton, 1984.
- (117) Murphy, L. M.; Hasnain, S. S.; Strange, R. W.; Harvey, I.; Ingledew, W. J. In *X-ray Absorption Fine Structure*; Hasnain, S. S., Ed.; Ellis Horwood: London, 1991.
- (118) DeBeer, S.; Wittung-Stafshede, P.; Leckner, J.; Karlsson, G.; Winkler, J. R.; Gray, H. B.; Malmström, B. G.; Solomon, E. I.; Hedman, B.; Hodgson, K. O. *Inorg. Chim. Acta* **2000**, *297*, 278.

- (119) DeBeer, S.; Randall, D. W.; Nersissian, A. M.; Valentine, J. S.; Hedman, B.; Hodgson, K. O.; Solomon, E. I. *J. Phys. Chem. B* **2000**, *104*, 10814.
- (120) LaCroix, L. B.; Randall, D. W.; Nersissian, A. M.; Hoitink, C. W. G.; Canters, G. W.; Valentine, J. S.; Solomon, E. I. *J. Am. Chem. Soc.* **1998**, *120*, 9621.
- (121) Fraga, E.; Loppnow, G. R. *J. Phys. Chem.* **1998**, *102*, 7659.
- (122) Sakurai, T.; Okamoto, H.; Kawahara, K.; Nakahara, A. *FEBS Lett.* **1982**, *147*, 220.
- (123) Han, J.; Loehr, T. M.; Lu, Y.; Valentine, J. S.; Averill, B. A.; Loehr, J. S. *J. Am. Chem. Soc.* **1993**, *115*, 4256.
- (124) Andrew, C. R.; Yeom, H.; Valentine, J. S.; Karlsson, B. G.; Bonander, N.; Pouderoyn, G. v.; Canters, G. W.; Loehr, T. M.; Sanders-Loehr, J. *J. Am. Chem. Soc.* **1994**, *116*, 11489.
- (125) Andrew, C. R.; Sanders-Loehr, J. *Acc. Chem. Res.* **1996**, *29*, 365.
- (126) Adman, E. T.; Godden, J. W.; Turley, S. *J. Biol. Chem.* **1995**, *270*, 27458.
- (127) Guss, J. M.; Merritt, E. A.; Phizackerley, R. P.; Freeman, H. C. *J. Mol. Biol.* **1996**, *259*, 686.
- (128) Basumallick, L.; Szilagyi, R. K.; Zhao, Y.; Shapleigh, J. P.; Scholes, C. P.; Solomon, E. I. *J. Am. Chem. Soc.* **2003**, *125*(48), 14784.
- (129) Olesen, K.; Veselov, A.; Zhao, Y. W.; Wang, Y. S.; Danner, B.; Scholes, C. P.; Shapleigh, J. P. *Biochemistry* **1998**, *37*, 6086.
- (130) Veselov, A.; Olesen, K.; Seinkiewicz, A.; Shapleigh, J. P.; Scholes, C. P. *Biochemistry* **1998**, *37*, 6095.
- (131) Germann, U. A.; Müller, G.; Hunziker, P. E.; Lerch, K. *J. Biol. Chem.* **1988**, *263*, 885.
- (132) Messerschmidt, A.; Huber, R. *Eur. J. Biochem.* **1990**, *187*, 341.
- (133) Solomon, E. I.; Sundaram, U. M.; Machonkin, T. E. *Chem. Rev.* **1996**, *96*, 2563.
- (134) Machonkin, T. E.; Quintanar, L.; Palmer, A. E.; Hassett, R.; Severance, A.; Kosman, D. J.; Solomon, E. I. *J. Am. Chem. Soc.* **2001**, *123*, 5507.
- (135) Dooley, D. M.; Rawlings, J.; Dawson, J. H.; Stephens, P. J.; Andréasson, L.-E.; Malmström, B. G.; Gray, H. B. *J. Am. Chem. Soc.* **1979**, *101*, 5038.
- (136) Messerschmidt, A. In *Multicopper Oxidases*; Messerschmidt, A., Ed.; World Scientific: Singapore, 1997.
- (137) McGarvey, B. R. In *Transition Metal Chemistry*; Carlin, B. L., Ed.; M. Dekker: New York, 1966.
- (138) Xu, F.; Berka, R. M.; Wahleithner, J. A.; Nelson, B. A.; Shuster, J. R.; Brown, S. H.; Palmer, A. E.; Solomon, E. I. *Biochem. J.* **1998**, *334*, 63.
- (139) Yaver, D. S.; Xu, F.; Golightly, E. J.; Brown, S. H.; Rey, M. W.; Schneider, P.; Halkier, T.; Mondrof, K.; Dalboge, H. *Appl. Environ. Microbiol.* **1996**, *62*, 834.
- (140) Xu, F.; Palmer, A. E.; Yaver, D. S.; Berka, R. M.; Gambetta, G. A.; Brown, S. H.; Solomon, E. I. *J. Biol. Chem.* **1999**, *274*, 12372.
- (141) Pascher, T.; Karlsson, G.; Nordling, M.; Malmström, B. G.; Vännegård, T. *FEBS Lett.* **1993**, *272*, 289.
- (142) Romero, A.; Hoitink, C. W. G.; Nar, H.; Huber, R.; Messerschmidt, A.; Canters, G. W. *J. Mol. Biol.* **1993**, *229*, 1007.
- (143) Nersissian, A. M.; Immoos, C.; Hill, M. G.; Hart, P. J.; Williams, G.; Herrmann, R. G.; Valentine, J. S. *Protein Sci.* **1998**, *7*, 1915.
- (144) Hall, J. F.; Lalji, D. K.; Strange, R. W.; Hasnain, S. S. *Biochemistry* **1999**, *38*, 12675.
- (145) Kataoka, K.; Nakai, M.; Yamaguchi, K.; Suzuki, S. *Biochem. Biophys. Res. Commun.* **1998**, *250*, 409.
- (146) Diederix, R. E. M.; Canters, G. W.; Dennison, C. *Biochemistry* **2000**, *39*, 9551.
- (147) Hart, P. J.; Nersissian, A. M.; Herrmann, R. G.; Nalbandyan, R. M.; Valentine, J. S.; Eisenberg, D. *Protein Sci.* **1996**, *5*, 2175.
- (148) Ryde, U.; Olsson, M. H. M.; Roos, B. O.; De Kerpel, J. O. A.; Pierloot, K. *J. Biol. Inorg. Chem.* **2000**, *5*, 565.
- (149) Ducros, V.; Brzozowski, A. M.; Wilson, K. S.; Brown, S. H.; Ostergaard, P.; Schneider, P.; Yaver, D. S.; Pedersen, A. H.; Davies, G. J. *Nat. Struct. Biol.* **1998**, *5*, 310.
- (150) Kitajima, N.; Fujisawa, K.; Morooka, Y. *J. Am. Chem. Soc.* **1990**, *112*, 3210.
- (151) Kitajima, N.; Fujisawa, K.; Tanaka, M.; Morooka, Y. *J. Am. Chem. Soc.* **1992**, *114*, 9232.
- (152) Holland, P. L.; Tolman, W. B. *J. Am. Chem. Soc.* **1999**, *121*, 7270.
- (153) Randall, D. W.; DeBeer George, S.; Holland, P. L.; Hedman, B.; Hodgson, K. O.; Tolman, W. B.; Solomon, E. I. *J. Am. Chem. Soc.* **2000**, *122*, 11632.
- (154) Randall, D. W.; DeBeer George, S.; Hedman, B.; Hodgson, K. O.; Fujisawa, K.; Solomon, E. I. *J. Am. Chem. Soc.* **2000**, *122*, 11620.
- (155) Solomon, E. I.; Randall, D. W.; Glaser, T. *Coord. Chem. Rev.* **2000**, *200–202*, 595.
- (156) Glaser, T.; Bertini, I.; Moura, J. J. G.; Hedman, B.; Hodgson, K. O.; Solomon, E. I. *J. Am. Chem. Soc.* **2001**, *123*, 4859.
- (157) Warshel, A.; Papazyan, A.; Muegge, I. *J. Biol. Inorg. Chem.* **1997**, *2*, 143.
- (158) Olsson, M. H. M.; Hong, G.; Warshel, A. *J. Am. Chem. Soc.* **2003**, *125*, 5025.
- (159) Knapp, S. K., T. P.; Zhang, X.; Fikar, R.; Potenza, J. A.; Schugar, H. J. *J. Am. Chem. Soc.* **1990**, *112*, 3452.
- (160) Miertus, S.; Scrocco, E.; Tomasi, J. *Chem. Phys.* **1981**, *55*, 117.
- (161) Tomasi, J.; Persico, M. *Chem. Rev.* **1994**, *94*, 2027.
- (162) Cossi, M.; Barone, V.; Cammi, R.; Tomasi, J. *Chem. Phys. Lett.* **1996**, *255*, 327.
- (163) Kitajima, N. *Adv. Inorg. Chem.* **1992**, *39*, 1.
- (164) Lever, A. B. P.; Dodsworth, E. S. In *Inorganic Electronic Structure and Spectroscopy*; Solomon, E. I., Lever, A. B. P., Eds.; John Wiley and Sons: New York, 1999; Vol. II.
- (165) Nersissian, A. M.; Hill, M. G.; Valentine, J. S. Personal communication, 2003.
- (166) Beratan, D. N.; Betts, J. N.; Onuchic, J. N. *Science* **1991**, *252*, 1285.
- (167) Marcus, R. A.; Sutin, N. *Biochim. Biophys. Acta* **1985**, *811*, 265.
- (168) Newton, M. D. *Chem. Rev.* **1991**, *91*, 767.
- (169) Sykes, A. G. *Struct. Bonding (Berlin)* **1991**, *75*, 175.
- (170) Di Bilio, A. J.; Hill, M. G.; Bonander, N.; Karlsson, B. G.; Villahermosa, R. M.; Malmström, B. G.; Winkler, J. R.; Gray, H. B. *J. Am. Chem. Soc.* **1997**, *119*, 9921.
- (171) Skov, L. K.; Pascher, T.; Winkler, J. R.; Gray, H. B. *J. Am. Chem. Soc.* **1998**, *120*, 1102.
- (172) Sigfridsson, K.; Ejdeback, M.; Sundahl, M.; Hansson, O. *Arch. Biochem. Biophys.* **1998**, *351*, 197.
- (173) Larsson, S. *J. Chem. Soc., Faraday II* **1983**, *79*, 1375.
- (174) Fraga, E.; Webb, M. A.; Loppnow, G. R. *J. Phys. Chem.* **1996**, *100*, 3278.
- (175) Ryde, U.; Olsson, M. H. M. *Int. J. Quantum Chem.* **2001**, *81*, 335.
- (176) Olsson, M. H. M.; Ryde, U.; Roos, B. O. *Protein Sci.* **1998**, *7*, 2659.
- (177) Winkler, J. R.; Wittung-Stafshede, P.; Leckner, J.; Malmström, B. G.; Gray, H. B. *Proc. Natl. Acad. Sci. U.S.A.* **1997**, *94*, 4246.
- (178) Beratan, D. N.; Hopfield, J. J. *J. Am. Chem. Soc.* **1984**, *106*, 1584.
- (179) Beratan, D. N.; Onuchic, J. N.; Hopfield, J. J. *J. Chem. Phys.* **1987**, *86*, 4488.
- (180) Beratan, D. N.; Onuchic, J. N.; Betts, J. N.; Bowler, B. E.; Gray, H. B. *J. Am. Chem. Soc.* **1990**, *112*, 7915.
- (181) Beratan, D. N.; Betts, J. N.; Onuchic, J. N. *J. Phys. Chem.* **1992**, *96*, 2852.
- (182) Betts, J. N.; Beratan, D. N.; Onuchic, J. N. *J. Am. Chem. Soc.* **1992**, *114*, 4043.
- (183) Onuchic, J. N.; Beratan, D. N. *J. Chem. Phys.* **1990**, *92*, 722.
- (184) Regan, J. J.; Onuchic, J. N. *Adv. Chem. Phys.* **1999**, *107*, 497.
- (185) Beratan, D. N.; Onuchic, J. N. *Photosynth. Res.* **1989**, *22*, 173.
- (186) Lowery, M. D.; Guckert, J. A.; Gebhard, M. S.; Solomon, E. I. *J. Am. Chem. Soc.* **1993**, *115*, 3012.
- (187) Machonkin, T. E.; Solomon, E. I. *J. Am. Chem. Soc.* **2000**, *122*, 12547.
- (188) The His π_1 levels are at higher energy as compared to those in Figure 17, Column 2, due to symmetrized C_5 structure, which was achieved by slightly altering the Cu–N(His) distances and positions in ref 7.

CR0206317